DOKUZ EYLÜL UNIVERSITY

GRADUATE SCHOOL OF NATURAL AND APPLIED

SCIENCES

PRODUCTION AND CHARACTERIZATION OF HIGH TEMPERATURE CORROSION RESISTANT MATERIALS

by

Esra DOKUMACI

June, 2012

İZMİR

PRODUCTION AND CHARACTERIZATION OF HIGH TEMPERATURE CORROSION RESISTANT MATERIALS

A Thesis Submitted to the
Graduate School of Natural and Applied Sciences of Dokuz Eylül University
In Partial Fulfillment of the Requirements for the Degree of Doctor of
Philosophy in Metallurgical and Materials Engineering, Metallurgical and
Materials Engineering Program
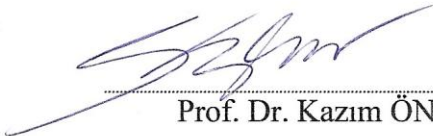
by
Esra DOKUMACI

June, 2012
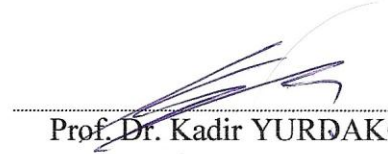**İZMİR**

Ph.D. THESIS EXAMINATION RESULT FORM

We have read the thesis entitled **"PRODUCTION AND CHARACTERIZATION OF HIGH TEMPERATURE CORROSION RESISTANT MATERIALS"** completed by **ESRA DOKUMACI** under supervision of **ASSOC. PROF. DR. A. BÜLENT ÖNAY** and we certify that in our opinion it is fully adequate, in scope and in quality, as a thesis for the degree of Doctor of Philosophy.

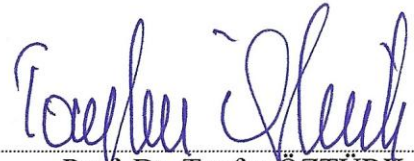Assoc. Prof. Dr. A. Bülent ÖNAY
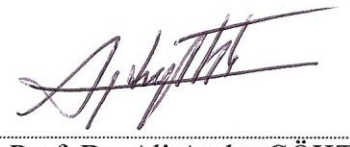
Supervisor

Prof. Dr. Kazım ÖNEL

Thesis Committee Member
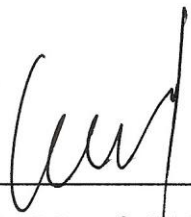
Prof. Dr. Kadir YURDAKOÇ

Thesis Committee Member

Prof. Dr. Tayfur ÖZTÜRK

Examining Committee Member

Prof. Dr. Ali Aydın GÖKTAŞ

Examining Committee Member

Prof. Dr. Mustafa SABUNCU
Director
Graduate School of Natural and Applied Sciences

ACKNOWLEDGMENTS

Esra DOKUMACI

PRODUCTION AND CHARACTERIZATION OF HIGH TEMPERATURE CORROSION RESISTANT MATERIALS

ABSTRACT

Operating temperatures of the current Nickel and Cobalt-base superalloys used in industrial applications, energy production and transportation are getting closer to their limits (~1200 degree Celcius). Thus, there is a search for new metallic structural materials that can be utilized in high temperature as well as corrosive environments. Because of their melting temperatures above 2000 degree Celcius, refractory metals can be considered as candidate materials for the next generation high temperature alloys. However, in environments such as air, refractory metals and their alloys cannot develop protective oxide layers. The objective of this study has been the production and characterization of refractory metal-based materials that are resistant to air oxidation at temperatures above 1000 degree Celcius.

In this study, production of binary and ternary Niobium alloys by the Vacuum Arc Melting (VAM) method was made by using both bulk and powder raw materials. Alloys produced from powders had better homogeneity even in "as-cast" condition. Effects of alloying elements like Cr, Mo and Ti on alloy microstructure and oxidation behavior were investigated through extensive characterization studies conducted by scanning electron microscopy (SEM) and X-ray diffraction (XRD). Oxidation resistances of the produced alloys were moderate and depended on the multi-phase structures of the alloys. For long-term use at high temperatures alloys will require some form of coatings. Boronizing, as a method of surface modification was applied to pure refractory metals Nb and Mo and found to increase their oxidation resistance. As future work on this Thesis work, investigation of the effect of heat-treatment on alloy microstructure and development of oxidation-resistant coatings are considered.

Keywords: Refractory metals, vacuum arc melting, oxidation, high temperature

KOROZYONA DAYANIKLI YÜKSEK SICAKLIK MALZEMELERİNİN ÜRETİMİ VE KARAKTERİZASYONU

ÖZ

Endüstriyel uygulamalar, enerji üretimi ve taşımacılık alanlarında kullanılan günümüz Nikel ve Kobalt-esaslı süperalaşımları kullanım sıcaklık sınırlarına (~1200 Santigrat derece) yaklaşmıştır. Bu sebeple, hem korozif ortamlarda hem de yüksek sıcaklıkta kullanılabilecek yeni metalik yapısal malzemeler aranmaktadır. 2000 Santigrat derecenin üzerinde ergime sıcaklıklarına sahip olmaları nedeniyle refrakter metaller gelecek nesil yüksek sıcaklık alaşımları için istenilen malzemeler olarak düşünülmektedir. Fakat hava gibi ortamlarda, refrakter metaller ve alaşımları koruyucu oksit tabakaları oluşturamazlar. Bu çalışmanın amacı, 1000 Santigrat derece üzerindeki sıcaklıklarda havada oksitlenmeye dayanıklı refrakter metal esaslı malzemelerin üretimi ve karakterizasyonudur.

Bu çalışmada, katı ve toz hammaddeler kullanılarak, Vakum Ark Ergitme (VAM) metodu ile ikili ve üçlü Niyobyum alaşımları üretilmiştir. Tozlar ile üretilen alaşımlar "döküldüğü" durumlarında bile daha iyi homojenliğe sahiptir. Krom (Cr), Mo ve Ti gibi alaşım elementlerinin mikroyapıya ve oksitlenme davranışına etkileri taramalı elektron mikroskobu (SEM) ve X-ışınları difraksiyonu (XRD) ile gerçekleştirilen geniş çaplı karakterizasyon çalışmaları yoluyla incelenmiştir. Üretilen alaşımların oksitlenme dirençleri alaşımların çok-fazlı yapılarına bağlıdır. Yüksek sıcaklıklarda uzun süre kullanılabilmeleri için alaşımların çeşitli şekillerde kaplamalara ihtiyaçları vardır. Yüzey modifikasyon yöntemi olarak borlama saf Nb ve Mo refrakter metallerine uygulanmıştır ve oksitlenme dirençlerini arttırdığı görülmüştür. Isıl işlemin alaşım kompozisyonu üzerindeki etkisi ve oksitlenmeye dirençli kaplamaların geliştirilmesi gelecekte yapılması düşünülen çalışmalardır.

Anahtar sözcükler: Refrakter metaller, VAM, oksitlenme, yüksek sıcaklık

CONTENTS

CHAPTER ONE
INTRODUCTION

Thermodynamic efficiencies of the engineering systems which convert heat to work in industrial applications, energy production and transportation, increase with the melting temperature of the metallic materials used in these systems. Today, operating temperatures of the stainless steels, Nickel (Ni) and Cobalt (Co)-based alloys used in furnaces, boilers, steam and gas turbines used in power stations as well as the internal combustion, jet and other type of engines used in transportation vehicles, space vehicles and military rockets are close to their application limits (Bewlay, Lewandowksi, & Jackson, 1997; Mandal et al., 2004; Meetham, & Van de Voorde, 2000). However refractory metals and their alloys with higher melting temperatures have the potential to become candidate materials for use at temperatures that are much higher than the operating temperatures of superalloys (Bewlay, Lewandowksi, & Jackson, 1997; Heilmaier et al., 2009; Kim, Tanaka, Kim, & Hanada, 2003). However, one major drawback for the application of refractory alloys based on Niobium (Nb) and Molybdenum (Mo), for example, is their poor resistance to oxidation (scaling) in oxygen-containing environments like air even at moderately elevated temperatures (800°C). Oxidation of such alloys produces volatile metal oxides and the volatilization of the oxide prevents the development a protective scale that would retard further oxidation (Subramanian, Mendiratta, & Dimiduk, 1996). Thus, methods to improve oxidation resistance of these alloys are needed. This can be done either by the development of new oxidation-resistant alloys and/or surface modification techniques (Habazaki et al., 1999; Stringer, Jaffee, & Kearns, 1975).

In this study, Nb- and Mo-base binary and ternary experimental alloys were produced by using a laboratory-type vacuum arc melting (VAM) equipment. Alloying elements such as Cr and Ti were used to improve the oxidation resistance of the refractory metals. Short-term isothermal oxidation tests were conducted on the alloys and effects of composition and microstructures of alloy on the properties of the surface oxide layers were investigated using a X-ray diffractometer (XRD) and a

scanning electron microscope (SEM) which is equipped with an energy dispersive spectrometer (EDS).

In order to further improve the oxidation resistances of alloys the surface modification method of pack boronizing was applied to some of the alloys. The boride layers formed over some of the alloys were found to provide some protection at high temperatures in air.

CHAPTER TWO
BACKGROUND

2.1 Refractory Metals

Metals and their alloys are important engineering materials for industrial operations which take place at room temperature as well as at high temperatures. Operation at high temperatures is of fundamental importance for many industries, including material production and processing, chemical engineering, power generation, transportation, and aerospace (Meetham, & Van de Voorde, 2000). Thermodynamic efficiencies increase with the melting temperature of the metallic materials used in these industrial sectors (Mandal et al., 2004; Vilasi et al., 1998). For these reasons, advanced structural materials are required for application at temperatures above the maximum operating temperature of conventional high temperature engineering materials such as Co- and Ni-base superalloys (Subramanian, Mendiratta, & Dimiduk, 1996). Refractory-base alloys have been expected to be as candidate materials to use at temperatures higher than the operating temperatures of current superalloys (Kim et al., 2003).

Refractory metals can be defined in different ways. "International Journal of Refractory Metals and Hard Materials" defines refractory metals as those metals whose melting points (Tm) are above $1850^{o}C$. According to this definition, Nb, Mo, V, Ru, Rh, Hf, Ta, W, Re, Os, Ir, Zr and Cr can be all called refractory metals. Sometimes they are defined as metals which have a body-centered cubic (BCC) structure and whose melting points are higher than those of their oxides. Of these metals niobium (Nb), tantalum (Ta) of group VB, molybdenum (Mo) and tungsten (W) of group VIB are considered as the four major refractory metals which currently have structural, electronic, chemical and nuclear applications. (Buckman, 1988; Lipetzky, 2002). Properties of these four major refractory metals are given in Table 2.1. In these work mainly Nb and its alloys are studied.

Table 2.1 Property comparison of pure refractory metals (Lambert, & Rausch, 1990).

Property	Niobium	Tantalum	Molybdenum	Tungsten
Structure and atomic properties				
Atomic number	41	73	42	74
Atomic weight	92.90	180.95	95.94	183.85
Density at 20°C g/cm^3	8.5	16.5	10.2	19.2
Crystal structure	bcc	bcc	bcc	bcc
Thermal properties				
Melting temperature, ^{o}C	2468	2996	2610	3410
Boiling temperature, ^{o}C	4927	5427	5560	5700
Vapor pressure at 2500K, mPa	5.3	0.11	80	0.0093
Coefficient of expansion, near RT (25°C), μm/m K	7.3	6.5	4.9	4.6
Specific heat at 20°C, kJ/kg.K	0.268	0.139	0.276	0.138
Thermal conductivity, W/m.K				
At 20°C	52.7	54.4	142	155
At 500°C	63.2	66.6	123	130
Electrical properties				
Electrical conductivity at 18°C	13.2	13.9	33.0	30.0
Electrical resistivity at 20°C nΩ.m	160	135	52	53
Additional properties				
Poisson's ratio at 25°C	0.38	0.35	0.32	0.28
Elastic modulus, GPa	103	185	324	400

Refractory metals are characterized by their high melting temperatures and the low vapor pressures (Northcott, 1961). The differences between the group VB and group VIB metals are as follows:

- Niobium and Ta exhibit high solubility of interstitial elements (C, O, H, and N).
- Molybdenum and W are significantly stronger in creep-rupture than Nb and Ta.
- Niobium and Ta exhibit lower ductile-to-brittle transition temperatures (DBTT) than Mo and W.

- Molybdenum and W are strengthened primarily by second-phase particles in combination with cold working. Solid solution strengthening and use of second-phase particles (dispersion hardening) are the mechanisms used for increasing the elevated temperature strengths of Nb and Ta (Buckman, 1988; Northcott, 1961).

The difference between the physical and mechanical properties of VB and VIB group refractory metals results from the atomic and electronic structures of these metals. Transition metals with five or less d-electrons exhibit relatively strong interatomic bonding. This results in higher resistance to deformation, and in higher melting points than those of metals (of the same group) with d-shells that are nearly or completely filled. The outer orbital electron concentration (e/a ratio) is important to the alloying of refractory metals, to chemical reactions such as corrosion and most importantly, to the solubility of interstitials (Wilkinson, 1969).

Among all refractory metals, niobium and molybdenum have been considered to have the greatest potential for high temperature applications (Miller, & Cox, 1960). The advantages of niobium and molybdenum compared with other refractory metals can be summarized as follows:

- Niobium is preferred in aerospace applications because of its lower density and better oxidation resistance of its alloys, although still not adequate to be used uncoated (Buckman, 1988).
- Niobium exhibits superconductivity in addition to its high temperature capability (Sheftel, & Bannykh, 1994).
- Niobium has the highest ductility of all refractory metals at room temperature.
- Molybdenum has a high specific elastic modulus, which makes it attractive for application that requires stiffness.
- The high thermal conductivity, low coefficient of thermal expansion and low specific heat of molybdenum provide resistance to thermal shock and fatigue.
- Molybdenum is stable in a wide variety of chemical environments (Gritsch et al., 2000).

Based on their melting temperatures, these metals have advantages for high temperature applications; however certain drawbacks have limited their use. Some of the limitations of refractory metals as high temperature materials can be summarized as follows:

- Nickel has a density of 8.9 g/cm^3. Refractory elements such as V, Nb and Cr have comparatively lower densities; but W, Ta, and Re metals with higher melting points have higher densities (Northcott, 1961),
- Most of the refractory metals have bcc crystal structure and therefore alloys based on these metals show significant loss of strength at high temperatures (Northcott, 1961),
- Casting of refractory metal base alloys is difficult due to their high melting temperature,

Table 2.2 Compositions of selected commercial molybdenum alloys (Lambert, & Rausch, 1990).

Alloy	Alloying addition (in w/o)
Unalloyed Mo	0.04 C, 0.003 O, 0.001 N
Reactive-metal-carbide alloys	
TZM (MT–104)	0.5 Ti, 0.08 Zr, 0.03 C
TZC	1.2 Ti, 0.3 Zr, 0.1 C
MHC (HCM)	1.2 Hf, 0.05 C
ZHM	0.5 Zr, 1.5 Hf, 0.2C
Solid-solution alloys	
25 W	25 W
30 W	30 W
5 Re	5 Re
41 Re	41 Re
50 Re	50 Re
Combination alloy	
HWM–25 (Mo-25WH)	1 Hf, 0.07 C, 25 W
Dispersion-strengthened alloys	
Z–6	0.5 ZrO$_2$
MH (HD)	150 K, 300 Si (ppm)
KW	200 K, 300 Si, 100 Al (ppm)

- All refractory metals have poor resistance to oxidation in oxygen-containing environments like air at even moderately elevated temperature. Oxidation produces nonprotective oxides on these metals and volatilization (or spallation) of their oxide prevents refractory metals from generating a protective film that would retard further oxidation (Habazaki et al., 1999). Some selected commercial Mo- and Nb- based refractory alloys and their compositions are given in Table 2.2 and Table 2.3.

Main applications for niobium are as alloying agents in steel and nickel alloys, electronic applications such as superconductors and magnetic applications such as medical diagnosis devices, in the aircraft engines, automotive industry, and nuclear industry and as a high-temperature structural material (Lipetzky, 2002; Titran, 1992).

Table 2.3 Compositions of selected commercial niobium alloys (Lambert, & Rausch, 1990; Wilkinson, 1969).

Alloy	Alloying addition (in w/o)
Unalloyed Nb	0.03 O, 0.01 C, 0.03 N
Nb-1Zr (D-11, FS-80, SCb-999, Cb-751)	1 Zr
B-33	5 V
B-66	5 Mo, 5 V, 1 Zr
C-103	10 Hf, 1 Ti, 0.7 Zr
C-129	10 W, 10 Hf
Cb-7	28 W, 7 Ti
Cb-16	20 W, 10 Ti
Cb-752	10 W, 2.5 Zr
D-14	5 Zr
D-31	10 Ti, 10 Mo, 0.1 C
Nb-10Ti-5Zr (D-36, SCb-885)	10 Ti, 5 Zr
D-41	1 Zr, 0.1 C
D-43	10 W, 1 Zr, 0.1 C
F-85	11 W, 28 Ta, 1 Zr
SCb-291	10 W, 10 Ta
WC-103	10 Hf, 1 Ti

Table 2.4 Application areas for some commercial Mo- and Nb- based alloys (Lambert, & Rausch, 1990).

Application Areas	Mo-based alloys	Nb-based alloys
Aerospace and Nuclear Industry	• Solid propellant rockets, • Honeycomb structures,	• Lifting and guidance structures for glide reentry vehicles • Leading edges • Trust chambers • Radiation nozzle extensions • Jet engine components • Rocket nozzles • Fasteners • Hot gas bellows • Honeycomb structures • Linear accelerators, microwave cavities • Superconductors
Electronic Industry	• Transducers, • Electron tube parts (supports, anodes), • X-ray targets, • Electrodes, • Thin-film substrates, • Heat sinks, • Backing wafers, • semiconductor,	• Superconducting wire
Process Industry	• Valves for hot sulfuric acids,	• Heating and cooling coils • Valves for hot sulfuric acids • Cathodic protection electrodes
Special Equipment Parts	• Furnaces parts (heating elements, shields, boats, trays, fixtures), • Extrusion dies, • Hot punches, • Vacuum metallizing coils, boats	• Rapid-fire gun barrels • Sodium vapor lamp electrodes

In vacuum furnaces, the heating elements, heat shields, racks for handling and positioning the furnace charge and container are required to operate at high temperatures and thus high purity and low vapor pressure constructional materials are necessary. Molybdenum, tungsten and tantalum meet these requirements. The choice of material depends also on the operating temperature of the furnace and the applications planned. Economic considerations make molybdenum the first choice for temperatures up to $2000^{o}C$. Tungsten can be used at temperatures around $3000^{o}C$.

Tantalum has a temperature capability intermediate between molybdenum and tungsten, but getters oxygen, hydrogen and nitrogen (Buckman, 1988). In Table 2.4, application areas of the alloys of Mo and Nb are given.

2.2 High Temperature Corrosion

High temperature corrosion refers to chemical degradation of materials at temperatures higher than the ambient temperatures. "High temperature", is a relative term which varies from metal to metal because of the difference in the melting temperatures of metallic materials (Khanna, 2002).

Oxidation is the most important high temperature corrosion reaction. Oxidation takes place when a metal or alloy heated to elevated temperatures in air or highly oxidizing environments, such as a combustion environment containing air or pure oxygen. Oxidation can also occur in mixed gas environments (CO/CO_2, H_2/H_2O) even though they have relatively low oxygen potentials (Khanna, 2002; Lai, 1990). The oxidation mechanism, upon which a scale (oxidation product) develops over a metal (or alloy) surface, can go through the following steps;

- Adsorption of oxygen molecules from the atmosphere on the metal surface.
- Nucleation of oxide at multiple sites that are thermodynamically favorable and its growth to form a continuous film.
- If the oxide layer (scale) is protective, the scale can prevent the metal from further oxygen attack.
- Growth stresses may develop during scale growth and cause cracks and porosity in the oxide that could modify the oxidation mechanism and cause failure of the protective scale (Lai, 1990; Wright, 1987).

Thermodynamically, an oxide will form on a metal surface when the oxygen potential in the environment is greater than the oxygen partial pressure in equilibrium with metal and its oxide. This equilibrium oxygen partial pressure ($P_{O_2}^{eqm}$) can be

calculated from the standard Gibbs free energy (GFE) of formation of the oxide (ΔG_f^o) (Equation 2.4) (Lai, 1990).

The oxidation reaction between a solid metal (M) and the oxygen gas to form a solid oxide can be written as in Equation 2.1.

$M(s) + O_2(g) = MO_2(s)$, where (s) denotes the solid phase and (g), the gas, respectively. (2.1)
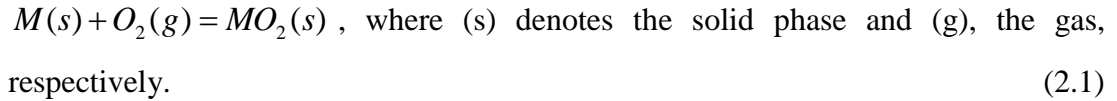
The standard GFE of this reaction is related to the $P_{O_2}^{eqm}$ of the reaction as shown in Equations 2.2 and 2.3.

$\Delta G^o = -RT \ln(a_{MO_2} / a_M \cdot P_{O_2})$ where (2.2)

a = activity, T = Temperature, R = gas constant

$\Delta G^o = RT \ln P_{O_2}$ since $a_{MO_2} = a_M = 1$, for pure materials (standard state) (2.3)

Thus, $P_{O_2}^{eqm} = e^{\Delta G^o / RT}$ (2.4)

The affinities of metals for oxygen (as well as other oxidants like N, C, S, Cl, etc.) are usually presented in the form of Ellingham diagrams (Figure 2.1), in which the standard GFE of oxide formation is plotted against temperature for one mole of oxygen. The driving force for metal-oxygen reactions is the Gibbs free energy change, ΔG^o.

Since the ΔG^o is described as

$\Delta G^o = \Delta H^o - T\Delta S^o$ (2.5)
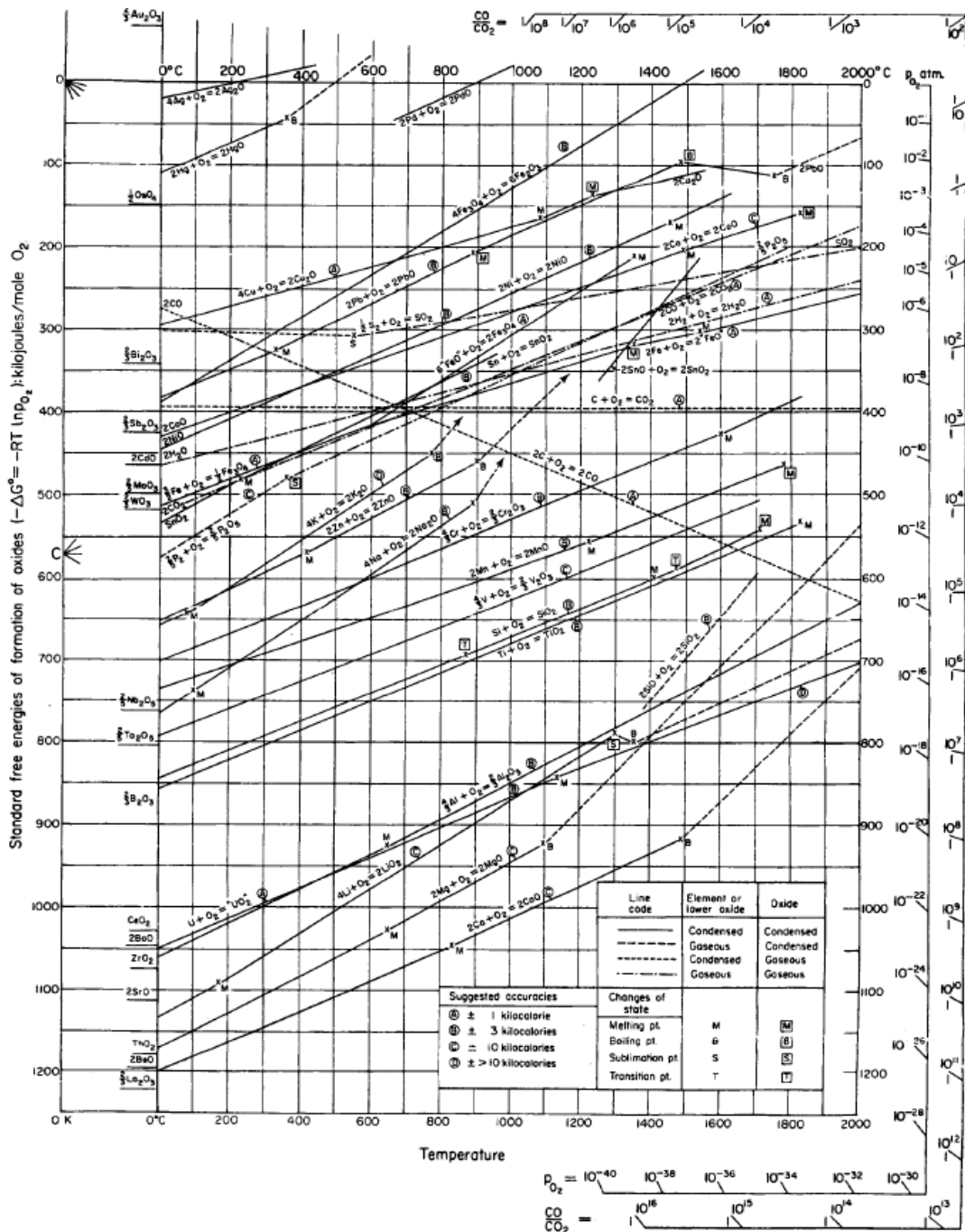
Figure 2.1 Ellingham Diagram, showing the change of Gibbs free energy with temperature for various oxides (Gaskell, 2003).

where ΔH^o is the Standard Enthalpy change, ΔS^o the Standard Entropy change and T the reaction temperature in Kelvin scale, the oxidation reaction will occur

spontaneously if $\Delta G^o < 0$. If $\Delta G^o = 0$, the reaction is at equilibrium and if $\Delta G^o > 0$ the reaction is thermodynamically unfavorable as written.

It is clear from Ellingham diagrams that oxides of iron, nickel and cobalt which are the base metals for the majority of engineering alloys are significantly less stable than the oxides of some of the alloying elements (Cr, Al, and Si) in these alloys. When one of these alloying elements is added to iron, nickel or cobalt in adequate concentration, the base alloy is protected from oxidation due to formation of the stable oxide of the alloying element at the surface. This type of "protective oxide formation" is the basis of the protection of most of the high temperature engineering alloys. Most of the current high temperature alloys are protected from oxidation by either alumina (Al_2O_3) or chromia (Cr_2O_3) containing scales. Coatings containing of these alloying elements can also be applied to prevent oxidation of the substrate (Khanna, 2002).

The oxidation of alloys involves the same general phenomena described for pure metals. However, alloys in general contain two or more oxidizable constituents making their oxidation more complex since additional factors and parameters must be taken into account during the process.

Several factors determine the effect of alloying additions on the oxidation process (Moricca, 2009):

- Alloying elements will have different diffusivities in the metallic substrate.
- Elements in the alloy will have different affinities for oxygen (as shown by Ellingham Diagram).
- Ternary or complex oxides may be formed during scaling.
- A degree of solubility may exist between the oxides in the scale.
- Metals ions will have different mobilities in the oxide phases.
- Dissolution of oxygen into the alloy may result in internal oxidation, if the concentration of the alloying elements is low.

2.3 Oxidation of Molybdenum

Molybdenum is used as an alloying element in many stainless steels and Ni-based alloys, because it possesses good resistance to corrosion by mineral acids in the absence of oxidizing agents. It is also resistant to iodine, bromine and chlorine vapors and to several liquid metals, including bismuth, lithium, magnesium, potassium and sodium. Molybdenum is relatively inert in hydrogen, ammonia, nitrogen atmospheres up to nearly 1100°C, although above this temperature ammonia and nitrogen form a nitride layer (Johnson, 1990). It is not subject to hydrogen embrittlement and, it does not form hydrides. Molybdenum is commonly used in the glass-processing industry, since it is unaffected by refractory oxides such as alumina, zirconia, beryllia, magnesia, and thoria at up to 1760°C in inert atmospheres. In spite of these excellent corrosion behaviors of molybdenum, one major drawback for the application of this metal is its poor resistance to oxidation even at moderately high temperatures (500°C) in oxygen containing environments such as air (Habazaki et al., 1999).

The solubility of oxygen in molybdenum is not significant (0.018 a/o at 1649°C) (Stringer, Jaffee, & Kearns, 1975). Hence, surface oxides readily form on Mo metal even at low oxygen pressures. At higher temperatures, oxidation rates become complicated by the high vaporization rate of MoO_3. Although weight increases arise with the stable scale formation, weight losses can concurrently occur when evaporation of low melting point oxides takes place (DiStefano, Pint, & DeVan, 2000).

Some studies on molybdenum at lower temperatures ($<700^{o}$C) in high levels of oxygen report the following results (Smolik, Petti, & Schuetz, 2000):

- Parabolic behavior between 250-450°C,
- Linear behavior above 400°C,
- Formation of MoO_2 and other oxides (MoO_z), where 2>z>3 between 450°C and 650°C),

- High vaporization of MoO_3, mass loss and oxidation rates above 650°C.

The surfaces of Mo metal remain bright up to 200°C and then temper (steel-blue) colors appear at 300°C. Speiser and St. Pierre (1964) reported that they observed a thin MoO_2 next to the metal or an external MoO_3 with a thin sub-layer of MoO_2 or other non-stoichiometric oxides intermediate between MoO_2 and MoO_3 during the oxidation of molybdenum in air between 450°C and 770°C (Stringer, 1973). Some properties of the oxides of molybdenum are listed in Table 2.5.

Table 2.5 Some physical and physico-chemical datas of the oxides of molybdenum (Kubaschewski, & Hopkins, 1962).

Compound	Remarks	Structure	Molar vol. (cm³)	Volume ratio	Density (10⁻³ kg/cm³)	M.p. (°C)	B.p. (°C)
Mo		b.c.c	9.4			2600	5550
MoO_2		monoclinic	19.7	2.10	4.11	1927	1977
Mo_4O_{11}		orthorhombic	134.0	3.57		disp.*	disp.
Mo_9O_{26}	Stable<650°C			3.50			
Mo_8O_{23}	Stable>650°C					disp.	disp.
MoO_3		orthorhombic	31.3	3.3	4.69	795	1155

*disprop: disproportionate
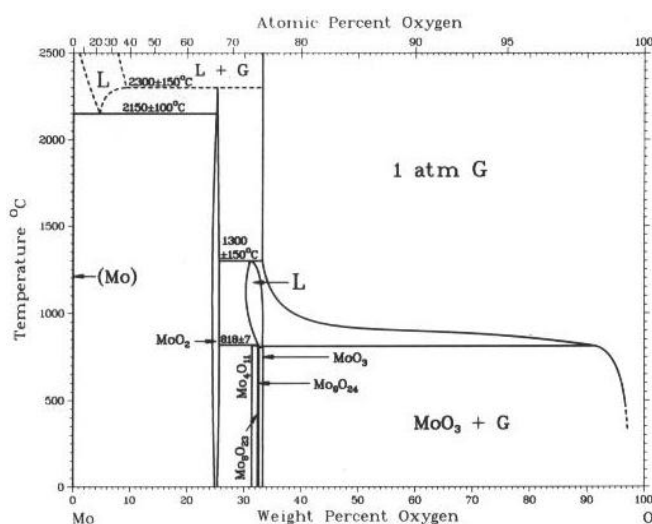
Figure 2.2 Mo-O binary phase diagram (Baker et al., 1992).

Above 550°C, MoO$_3$ begins to evaporate noticeably. MoO$_3$ melts at 795°C and forms the MoO$_2$-MoO$_3$ eutectic which melts at 778°C (Figure 2.2) (Davis, 1997; Johnson, 1990), MoO$_3$ sublimes, and the vapor pressure becomes significant above 700°C. At lower temperatures (up to 700°C) where the rate of volatilization is very low, the formation of the MoO$_3$ has been found to vary parabolically with time. Volatilization reaches a maximum rate at 600°C. At higher temperatures (725-770°C) the time dependence appears to be linear with breaks in the curves probably caused by cracking of the oxide. At 770°C the oxide attains a limiting thickness and the rate of formation is balanced by the rate of volatilization (Kubaschewski, & Hopkins, 1962).

Above the melting point of MoO$_3$, oxidation occurs in the presence of liquid, but at still higher temperatures the rate of evaporation of MoO$_3$ is so fast that no liquid is present. The rate of oxidation in this range is substantially constant, but is slightly faster when liquid is present. The accelerating effect of liquid MoO$_3$ is also apparent at temperatures around 800°C by the faster oxidation at the bottom of a specimen where liquid collects (Kubaschewski, & Hopkins, 1962). Figure 2.3 shows the volatile species diagram for molybdenum at 827°C. The diagram shows how the vapor pressure of vapor species (MoO$_3$) varies with oxygen pressure as well as the oxygen pressure required to oxidize Mo to MoO$_2$ using the following reactions:

$$Mo(s) + O_2(g) \rightarrow MoO_2(s) \qquad\qquad (2.6)$$
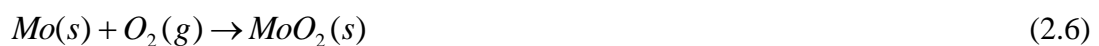
and the oxygen pressure required to further oxidize MoO_2 to MoO_3 using the following reaction:

$$MoO_2(s) + \tfrac{1}{2}O_2(g) \rightarrow MoO_3(l) \qquad\qquad (2.7)$$

The reaction used to calculate the pressure of $MoO_3(g)$ over the $Mo(s)$ condensed phase is:

$$Mo(s) + \tfrac{3}{2}O_2(g) \rightarrow MoO_3(g) \qquad\qquad (2.8)$$

and over the $MoO_2(s)$ condensed phase is:

$$MoO_2(s) + \tfrac{1}{2}O_2(g) \rightarrow MoO_3(g) \qquad\qquad (2.9)$$

and over the $MoO_3(l)$ condensed phase is:

$$MoO_3(l) \rightarrow MoO_3(g) \qquad\qquad (2.10)$$
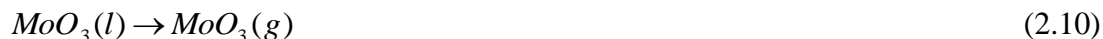
If the partial pressure of the MoO_3 (g) reaches its saturation pressure, condensed MoO_3 can form on the surface. This means that the partial pressure of MoO_3 (g) can control the transport mechanism for oxidation. On the other hand, if the partial pressure of MoO_3 (g) remains below the saturation pressure, the transport mechanism will be gas phase diffusion near the surface of the metal. By controlling the partial pressure of MoO_3 (g) near the surface of the metal, the rate of volatilization of MoO_3 from the surface will be controlled (Helmick, 2003).
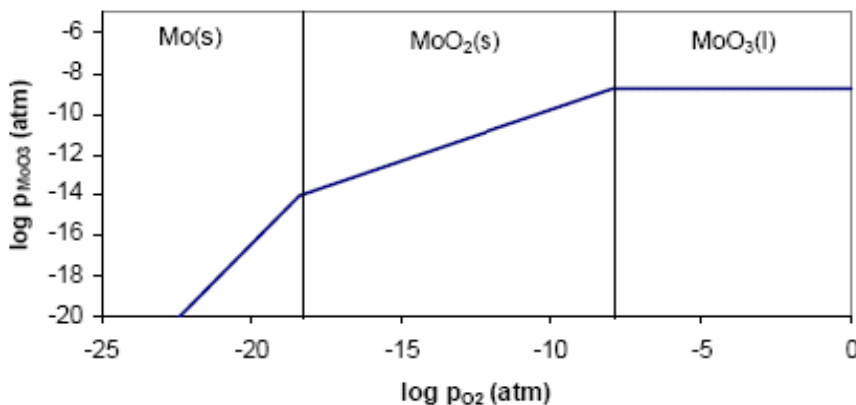
Figure 2.3 Volatile species diagram for molybdenum at 827°C (Helmick, 2003).

Researchers have concluded that rapid gas flow rates increased the volatilization of MoO_3, which in turn increased the oxidation rate. Also, they have suggested that there is a maximum oxidation rate for molybdenum at a given temperature at which the partial pressure of MoO_3 (g) is maintained at a low value near the surface of the specimen. These results suggest that the description of oxidation of molybdenum includes boundary layer flow kinetics controlling the transport mechanisms. The

standard Enthalpy and Entropy changes for oxidation reactions of Mo are given in Table 2.6.

Table 2.6 Standard free energy reactions ($\Delta G^o = \Delta H^o - T\Delta S^o$) (Türkdoğan, 1980).

Reaction	ΔH^o (J)	ΔS^o (J)	Error (±kJ)	Range (^{o}C)
$<MoO_2> = <Mo> + (O_2)$	132.7	2.8	12.5	25-1412
$(MoO_2) = <Mo> + (O_2)$	578.6	166.6	12.5	25-2000
$<MoO_3> = \{MoO_3\}$	47.7	45.2	-	795m
$<MoO_3> = <Mo> + 3/2(O_2)$	740.6	246.8	12.5	25-795m
$(MoO_3) = <Mo> + 3/2(O_2)$	360.0	59.4	20.9	25-2000

$< >$: solid ( ): gases { }: liquid   m: melting

It may be concluded that although MoO_3 offers some protection at the lower temperatures and for limited times during which the oxidation is parabolic, at higher temperatures it is non-protective, and the rate of oxidation of sub-oxides to the trioxide at the sub-oxides/trioxide interface is equal to the rate of diffusion of oxygen ions through the sub-oxide to the metal.

2.4 Oxidation of Niobium

When a pure niobium surface exposed to oxygen or oxygen-containing environments like air, on the contrary to molybdenum, significant amount of oxygen (1 a/o at 700°C and 9 a/o at 1915°C) initially dissolves in the metal before the nucleation of three stable oxides (Figure 2.4), such as mono-oxide (NbO), dioxide (NbO_2) and pentoxide (Nb_2O_5) and some metastable oxides (NbO_x, NbO_y, NbyO etc.) whose compositions are uncertain. The lower oxides (NbO and NbO_2) exist only as relatively thin layers and they play a negligible part in the oxidation process at elevated temperatures. Pentoxide (Nb_2O_5) exists in different polymeric forms; a preferentially-oriented layer of α-Nb_2O_5 phase, or β-Nb_2O_5 phase formed by the transformation of α-Nb_2O_5 (Khanna, 2002; Smith, 1960; Stringer, Jaffee, & Kearns, 1975). Some properties of the niobium oxides are given in Table 2.7.
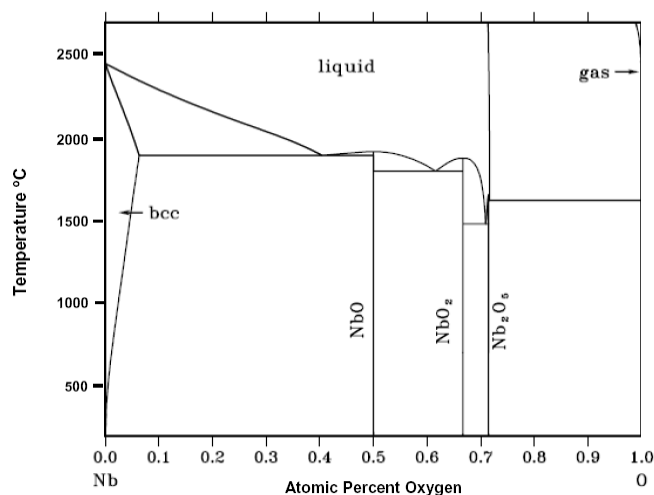
Figure 2.4 Nb-O binary phase diagram (Moricca, 2009).

The kinetics of the oxidation reactions of Nb are quite complex. There are several views about the oxidation mechanism of niobium. In Table 2.8, characteristic feature of the oxidation of niobium is given.

Table 2.7 Some physical and physico-chemical datas of the oxides of niobium (Kubaschewski, & Hopkins, 1962).

Compound	Remarks	Structure	Molar vol. (cm^3)	Volume ratio	Density (g/cm^3)	M.p. (^{o}C)	B.p. (^{o}C)
Nb		b.c.c	10.9			2468	4400
Nb$_4$O		tetragonal					
NbO	25% lattice sites vacant	cubic:NaCl	15.0	1.37	7.26	1945	
NbO$_2$		tetragonal	20.5	1.87	5.98	1915	
Nb$_2$O$_5$ α	metastable	orthorhombic			5.17		
Nb$_2$O$_5$ β		monoclinic	58.3	2.68	4.95	1490	dec.*

* dec: decomposes

The oxidation of niobium below 300°C is explained by the Cabrera-Mott-Hauffe-Ilschner mechanism. According to this mechanism, a very thin oxide film on a metal adsorbs oxygen at its surface, and electrons pass through the film from the metal to the adsorbed surface layer. By this way a strong electric field is set up which pulls the ions (cations or anions) across the film, depending on

whether the passage of electrons or ions is rate-determining, one obtains a logarithmic or inverse logarithmic (parabolic) relationship between the increase in thickness and the time. Above $300^{o}C$ apparently pore free, adherent oxide films formed in bright temper colors (Kubaschewski, & Hopkins, 1962).

Table 2.8 Characteristic feature of the oxidation of niobium (Argent, & Phelps, 1960).

	Growth law	Oxide type	Oxide character	Deviations from stoichiometry
250-400°C	parabolic	Amorphous+ αNb_2O_5	Adherent film showing temper colors	Not known
400-450°C	parabolic changing to linear	Amorphous+ αNb_2O_5	Adherent dark film.	Changes from anion deficient at $400^{o}C$ to apparent cation deficiency at $450^{o}C$
450-600°C	parabolic changing to linear	αNb_2O_5	Cream oxide. Some spalling at temperature	Maximum specific surface $450^{o}C$ apparently cation deficient. Approaches stoichiometry at $550^{o}C$.
600-675°C	linear	αNb_2O_5	Cream oxide. Slight spalling	Increasing anion deficiency
675-850°C	linear	αNb_2O_5	Light grey oxide changing to dark grey with increasing temperature. No spalling at temperature or on cooling.	Anion deficient returning to stoichiometry at $800^{o}C$
850-1050°C	linear	βNb_2O_5	Cream oxide. No spalling at temperature but spalls on cooling.	Not known

The metastable sub-oxides begin to decompose at about $400^{o}C$. Noeman et al. reported that after 20h at $500^{o}C$ under low oxygen pressures the phases present on pure niobium metal were Nb-containing dissolved oxygen and a number of sub-oxides, which formed as platelets penetrating into the metal/oxide interface. In the meantime, nucleation of Nb_2O_5 (pentoxide) is also observed. At high oxygen pressures, Nb_2O_5 can spread over the metal surface rapidly (Stringer, Jaffee, & Kearns, 1975).

Between 400°C and 600°C, the external niobium pentoxide, Nb_2O_5, which is effectively a non-protective porous scale, continues to grow and thickness of the oxide layer increases with increasing temperature. The oxide layer reaches a limiting thickness at which it can no longer stand the compressive growth stresses due to the high volume ratio of the oxide and eventually fails allowing the penetration of oxygen into the metal surface. This process repeats with the development of a thick outer scale (Stringer, Jaffee, & Kearns, 1975).

At all temperatures, oxygen dissolves in the metal, and this has an adverse effect on the mechanical properties of scale. At about 500°C, in the parabolic-linear transition range, small blister-like cracks start forming because of the presence of the metastable platelets which appear to act as a crack initiator in the adherent pentoxide. The outer scale breaks down to a powdery oxide owing to the large change in density caused by the transformation of amorphous Nb_2O_5 to α-Nb_2O_5 (a density change of 4.36 to 5.17 g/cm^3 at room temperature) completely (Kubaschewski, & Hopkins, 1960; Stringer, Jaffee, & Kearns, 1975). The rate-controlling process is the diffusion of anions through a coherent oxide layer at the surface of the metal, but this layer is of virtually constant thickness. An adsorbed layer of oxygen completely covers the oxide surface promoting a linear and a pressure independent oxidation rate. The surface of the oxide is no longer saturated with adsorbed oxygen and the temperature dependence of the rate of oxidation decreases. Diffusion is still the rate controlling process and thus the rate of oxidation depends on the square root of the oxygen pressure (Argent, & Phelps, 1960).

Above 600°C the metastable lower oxides platelets disappear and in their place, beneath the outer pentoxide layer small amounts of the stable lower oxides NbO and NbO_2 are detected. They appear to be present as discrete islands rather than as continuous layers. The reaction mechanism changes drastically at high temperatures, above 650°C. The initially grown oxides NbO or NbO_2 are now directly formed from metastable oxides at lower temperatures. This causes formation of a uniform oxide layer that is unlike the uneven and localized scaling at lower temperatures. The reaction after extended period changes to a linear rate. The scale formed on niobium

appears to have better adherence and less porosity at 700°C compared to 600°C at where the linear oxidation rate reaches its maximum value. These textural changes in the scale on the niobium appear to be due to the formation of different Nb_2O_5 modifications in different temperature regions and to the ability of some modifications to deform plastically (Khanna, 2002; Stringer, 1973).

The crystal structure of Nb_2O_5 undergoes a number of modifications and some of the structures appear to be relatively minor rearrangements making the process unclear whether they are all stable or not. However, modification of Nb_2O_5 from the γ to α phase occurs at 800-850°C significantly. This change in modification of Nb_2O_5 gives rise to irregularities in the temperature dependence of the linear oxidation rate. A pronounced whisker growth is observed due to formation of α Nb_2O_5 which consists of single crystal of Nb_2O_5. The oxide formed above 850°C is β-Nb_2O_5 and the temperature dependence of the oxidation rate decreases (Stringer, 1973). The subsequent acceleration noted by some workers at 1150°C could be due to the onset of conditions analogous to combustion involving a considerable rise in the temperature of the specimen. Klopp, Sims and Jaffee reported that at 1400°C the heat of reaction was sufficient to melt the niobium metal (Argent, & Phelps, 1960).

Another common notation about pentoxide is that of Brauer who identified a low temperature form. T-Nb_2O_5, is stable up to approximately 900°C; an intermediate form, M-Nb_2O_5, stable between 900 and 1100°C; and a high temperature form, H-Nb_2O_5, stable above 1100°C (Stringer, Jaffee, & Kearns, 1975). Later authors have questioned the separate existence of M-Nb_2O_5; the powder diffraction pattern is similar to the H form, and M was probably an incompletely crystallized form of H. It seems probable that Nb_2O_5 has a limited range of stoichiometry: oxygen-deficient material can be produced, which is black in color; but at large deviations, succession of closely-related berthollide structures with the general formula $Nb_{3n+1}O_{8n-2}$ appear, due to oxygen vacancy (Sheasby, & Smeltzer, 1981).
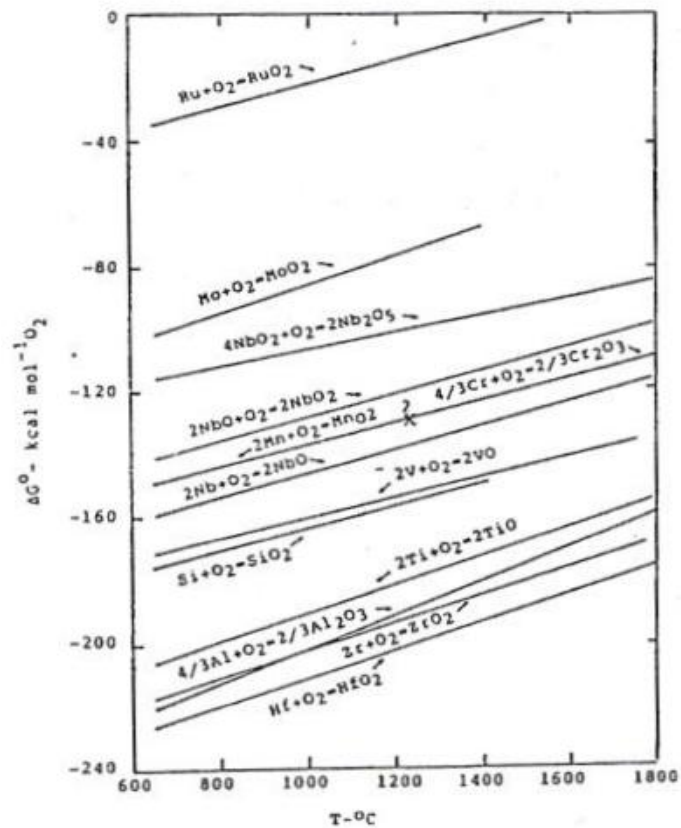
Figure 2.5 Standard free energy of formation of Nb oxides
(Grobstein, & Doychak, 1988).

Table 2.9 Standard free energy reactions ($\Delta G^o = \Delta H^o - T\Delta S^o$) (Türkdoğan, 1980).

Reaction	ΔH^o (J)	ΔS^o (J)	Error (±kJ)	Range (^{o}C)
\<NbO\> = {NbO}	83.7	38.5	20.9	1937m
\<NbO\> = \<Nb\> + 1/2(O$_2$)	414.4	86.6	20.9	25-1937m
\< Nb$_2$O$_5$\> = {Nb$_2$O$_5$}	104.3	58.4	2.0	1512m
\< Nb$_2$O$_5$\> = 2\<Nb\> + 5/2(O$_2$)	1889.5	419.9	12.5	25-1512m
\< NbO$_2$\> = {NbO$_2$}	92.1	42.2	20.9	2150m
\< NbO$_2$\> = \<Nb\> + (O$_2$)	784.1	167.0	10.4	25-2150m

< >: solid ( ): gases { }: liquid m: melting

According to the Ellingham diagram given in Figure 2.5 the first lower oxide of Nb; NbO, has the largest negative value of ΔG^o and is represented by the lowest line in the diagram. Between the two lower oxides of Nb (NbO and NbO$_2$) the lines of oxides of chromium and manganese are present. This means that oxides of Cr

(Cr$_2$O$_3$) are less stable than the NbO. The least stable oxide of Nb is Nb$_2$O$_5$. However, it is clear that Nb$_2$O$_5$ is more stable than the oxide of Mo (MoO$_2$). Standard Enthalpy and Entropy changes for oxidation reactions of Nb are given in Table 2.9.

2.5 Effects of Alloying Elements on Oxidation of Refractory Metals

In common with all the refractory metals, niobium has poor oxidation resistance, even at moderately elevated temperatures. Although the oxides of niobium are porous and essentially non-protective, Nb$_2$O$_5$ remains solid to about 1500°C. Thus the oxidation problem associated with niobium is considerably less formidable than that encountered with molybdenum or tungsten, which form relatively low melting and volatile oxides and provide no protection against oxidation (Table 2.10). So, there seems little hope that competitive oxidation resistant alloys can be developed based on tungsten and molybdenum. The resistance against oxidation can be achieved with a protective oxide scale which has the following features (Stott, 1989; Wright, 1987):

- High thermodynamic stability (high negative Gibbs free energy of formation) so that it forms preferentially to other possible oxides.
- Low vapor pressure so that the oxide does not evaporate and forms as a solid and does not react further with the environment to form volatile products.
- Pilling-Bedworth ratio (the ratio of the molar volume of oxide to the molar volume of the metal) is equal or close to 1 so that the oxide completely covers the metal surface, does not spall, and remains adherent to the substrate metal. If the ratio is more than 2, the stress accumulated is compressive; whereas, if the PBR is less than 1, the scale has tensile stress.
- Low coefficient of diffusion of reactant species (metal cations and oxidant anions) so that the scale has a slow growth rate,
- High melting temperature,

Table 2.10 Comparison of melting points of metallic elements and their oxides (Buckman, 1988).

Element	Crystal Structure (stable at 25°C)	Melting point, K		Ro/m*
		Metal	Oxide	
Ti	hcp	1943	2098	1.1
Zr	hcp	2125	2688	1.3
Hf	hcp	2500	3173	1.3
V	bcc	2175	963	0.4
Nb	bcc	2740	1763	0.6
Ta	bcc	3287	2045	0.6
Cr	bcc	2130	2540	1.2
Mo	bcc	2890	1068	0.4
W	bcc	3680	1773	0.5
Re	hcp	3453	570	0.2
Ni	fcc	1728	2233	1.3

*Ro/m=Tm (oxide)/Tm (metal)

- Good adherence to the metal substrate, which usually involves a coefficient of thermal expansion close to that of the metal, and sufficient high-temperature plasticity to resist fracture caused by differential thermal expansion stresses.

- Free of pores, cracks, or other crystalline defects thereby preventing short circuit transport of reactants across it.

According to these requirements, as opposed to molybdenum, the oxide scale formed on niobium seems partially protective and the addition of alloying elements to niobium (or molybdenum) can vary the oxidation behavior and improve both the mechanical properties and the oxidation resistance of this pure metal. Alloying modifies the non-protective scales by the ways explained below.

2.5.1 Formation of Phases Other than Nb_2O_5 in the Scale

One way to improve the oxidation resistance of niobium is to reduce the oxidation rate with the addition of elements which encourage the formation of oxides other than Nb_2O_5. This may be either the oxide of the alloy addition, or a compound oxide

with the base metal (Argent, & Phelps, 1960). If this is to be achieved, the alloy element must have a greater affinity for oxygen than niobium does, and this restricts the choice to elements like titanium, zirconium, hafnium, aluminum, beryllium, silicon, calcium, magnesium and the rare earths. At low alloy contents, such an alloy will oxidize internally, and it is necessary to exceed a critical concentration to form its own protective external scale. However, large additions of some of these elements have a detrimental effect on the ductility or refractoriness of niobium (Smith, 1960). This critical content depends on the formation of a critical volume of internal oxide, and decreases rapidly with decreasing oxygen pressure. As a consequence the presence of a secondary getter by reducing the effective oxygen concentration at the metal/oxide interface can facilitate the development of an external scale. The formation of an internal oxide of a reactive metal will probably not reduce the rate of external oxidation significantly, but it may reduce the oxygen contamination in the metal, which may be very important in the case of niobium (Perkins, Chiang, Meier, & Miller, 1989).

2.5.2 Alteration of the Diffusion Rates Through the Scale

Niobium pentoxide (Nb_2O_5) possess an oxygen-deficient lattice and according to the Wagner model, alloy cations having a higher valency than niobium should reduce the number of lattice defects and thus the diffusion rate of oxygen through the adherent compact scale. Titanium, zirconium and tantalum, after an initial worsening, all have a beneficial effect on the oxidation resistance of niobium at higher concentrations. These three metals mentioned have a higher affinity for oxygen than niobium, and would therefore be oxidized preferentially. When these metals are present in sufficient concentration in the alloy, coherent films of TiO_2, ZrO_2 or Ta_2O_5 may be formed. In addition, the volume ratio of TiO_2/Ti and ZrO_2/Zr are considerably smaller than that of $Nb_2O_5/2Nb$ and the oxide layers thus much less prone to cracking (Argent, & Phelps, 1960; Kubaschewski, & Hopkins, 1960).

2.5.3 Alteration of the Scale Plasticity

Kling (1958) suggested that alloy additions might be made in accordance with the above mentioned Wagner model:

- To reduce the rate at which the initial oxide film grow prior to fracturing,
- To alter the mechanical properties of the scale, either by increasing the fracture strength or decreasing the creep strength, so that the growth stresses could be relaxed by creep.
- To stabilize the lower oxides, this might have better transport properties and lower growth stresses (Stringer, Jaffee, & Kearns, 1975).

Kling noted that Ti, V, and Mo elements have positive effects on the plasticity of the oxide scale if they are added at moderate concentrations. He suggested that an alloy addition of a lower valency would increase the defect concentration in the scale, and thus make it more plastic (Stringer, Jaffee, & Kearns, 1975).

Wlodek (1960) also pointed out the same view with Kling that if the lower oxides NbO and NbO_2 could be stabilized they would have lower Pilling-Bedworth ratios, and furthermore if present as continuous intermediate layers would allow a more gradual change in specific volume, thus reducing the effective growth stress at any interface. In addition, stabilizing the lower oxides would probably prevent the formation of NbO_2 platelets, and thus remove the crack initiators.

2.5.4 Effect of Alloy Cation Size on the Nb_2O_5 Crystal Structure

Since the metal cations occupy a minor part of the oxide volume, any variation in their dimensions has been considered to have a reduced effect on the oxide dimensions. An alloying element in the ionized state may exert a different dimensional effect to the oxide. Because of this consideration, the oxide/metal volume ratio is thought to be hardly affected by the atomic radii of the constituent elements unless they are markedly different and one of them is appreciably

concentrated in the oxide (Smith, 1960). Nevertheless, some investigators suggested that the presence of smaller cations in solution in the pentoxide might in fact reduce the specific volume of the oxide, and thus reduce the Pilling-Bedworth Ratio (Stringer, Jaffee, & Kearns, 1975).

2.5.5 Effect of Cation Valency on Oxide Stoichiometry and Nb$_2$O$_5$ Crystal Structure

The addition of elements with lower effective valences than that of niobium had been proposed to reduce the volume ratio and the tendency to cracking of the Nb$_2$O$_5$. (Argent, & Phelps, 1960; Smith, 1960)

Regarding the effect of valency on the behavior of Nb oxides, the following observations have been reported at a temperature where only such oxides are formed in the scale (Smith, 1960):

- of the quadrivalent elements titanium, zirconium and silicon, titanium improves the oxidation resistance of pentavalent niobium, while zirconium and silicon reduce it,
- vanadium, which can exhibit valances of both 4 and 5, markedly improves the oxidation resistance,
- molybdenum, with alternative valances both higher (6) and lower (4) than niobium, also improves the oxidation resistance,
- tungsten, with the same possible valances as molybdenum, was initially reported to have a beneficial effect at 1100°C,
- chromium, with alternative valencies of 6 and 3, has beneficial effects.

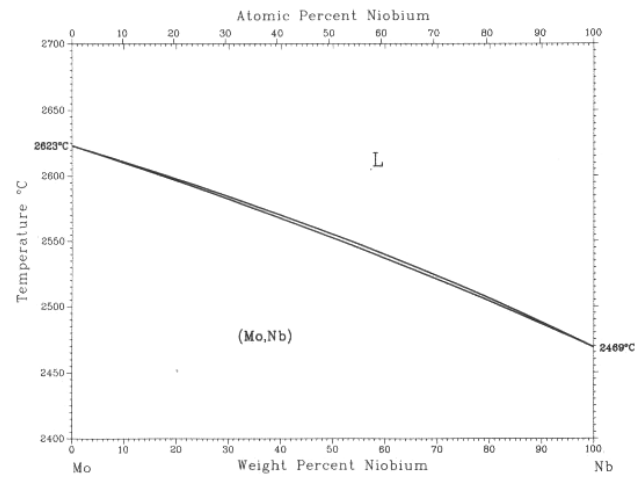Barrett and Clauss (1958) reported that alloy elements capable of forming 3+ ions with a size similar to that of the Nb^{5+} ion appeared to give good results. Klopp (1960) on the other hand suggested that the size effect was more important than the valance effect; with smaller ions than Nb^{5+} apparently contracting the scale and thus reducing the growth stresses in the scale (Stringer, Jaffee, & Kearns, 1975).

Wagner mechanism, for metals having n-type conducting oxides it is possible to make metallic additions that have a higher valency, a higher affinity for oxygen, and a smaller radius in the ionic form, so that the added element dissolves in the form of ions in the oxide of the base metal, and reduces the number of cations per anion and thus the number of anion deficiencies such as vacancies in the anion lattice (Kubaschewski, & Hopkins, 1960). Therefore, these results indicate that there seems to be no simple and consistent relationship among the influence of an added element, its valency and its ionic size.

2.6 Historical Development of Niobium-Based Alloys

Structural materials for high-temperature applications, such as jet engines, gas turbines and turbine blades applied in advanced aerospace or turbine engine systems require a balanced combination of ductility and toughness at low temperatures, strength and creep resistance at elevated temperatures, and oxidation resistance properties. Therefore, researches have focused on the Nb-based alloys as potential candidates to replace superalloys because of their high melting points, low density and high-temperature strength but their oxidation resistance at elevated temperatures is catastrophic (Bewlay, Lewandowksi, & Jackson, 1997; Heilmaier et al., 2009; Perepezko, 2009). For this reason, since the 1950's extensive efforts have been made to improve the oxidation resistance of Nb by modifying the metal composition and properties of oxidation products (Bewlay, Jackson, Zhao, & Subramanian, 2003; Stringer, Jaffee, & Kearns, 1975).

In the late 1950's, some researchers studied the effects of alloying elements which are near neighbors of Nb in the periodic table, on the mechanical properties of niobium (Begley, & Bechtold, 1961). Two-phase diagrams belonging to Mo, Ti and Cr binary systems with niobium are shown in Figure 2.6. Niobium forms a continuous series of solid solutions with molybdenum and β-titanium. The other refractory alloy element Cr has relatively low solubility in niobium at elevated temperatures. These alloying elements have relatively high melting points. Except titanium, the melting temperatures of the other elements are above 1800°C.
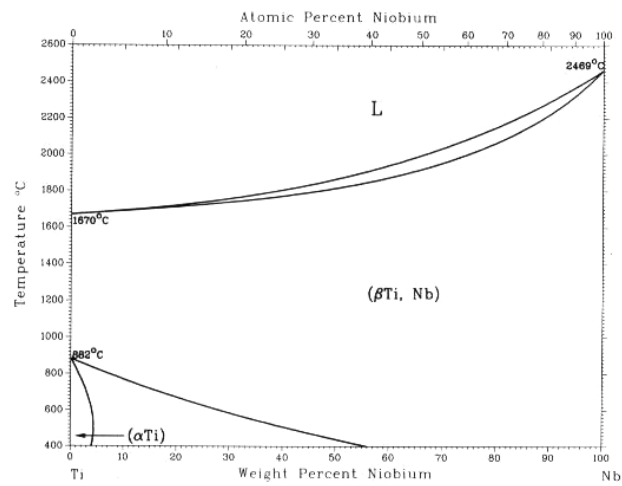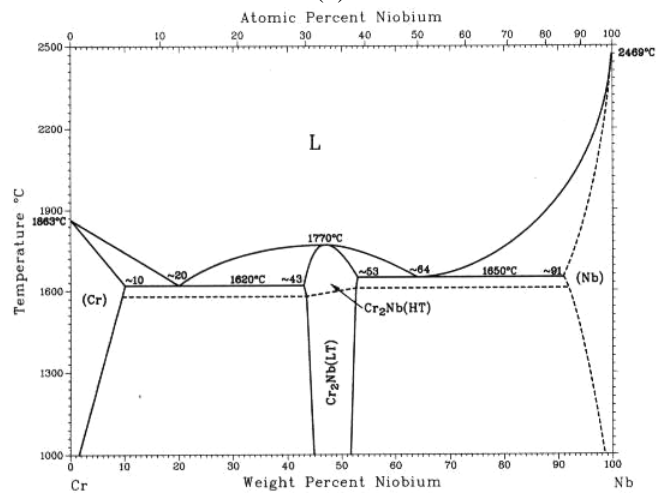
Figure 2.6 Phase diagrams of niobium with some of its near neighbors in the Periodic Table. (a) Mo, (b) Ti and (c) Cr (Baker et al., 1992).

These studies resulted in several alloys with good mechanical properties but poor oxidation resistances (Argent, & Phelps, 1960; Goldschmidt, & Brand, 1960; Mayo, Shepherd, & Thomas, 1960).

Consequently, in 1960's research concentrated on the development of coating systems for Nb alloys (Weber, Bouvier, & Slama, 1973). Although silicide-based coatings with good oxidation resistances were developed, local coating failure and following degradation of the coating due to inter diffusion with the substrate was the major drawback in their applications (Cox, & Brown, 1964). The other Nb-based alloys produced commercially in 1970's, still were not adequate to be used in oxidizing environments without a coating (Alam, Rao, & Das, 2010; Zmii, Ruden'kii, Bredikhin, & Kunchenko, 2008).

In the mid-1980's studies in this field focused mostly on the production of Nb-Al binary alloys and the use of Al as an alloying element to improve the oxidation resistance of Nb through the formation of a protective Al_2O_3 layer (Perkins et al., 1989). As seen in Figure 2.7, the Nb-Al binary system has three intermetallics; Nb_3Al, Nb_2Al, and $NbAl_3$. There are several studies on the oxidation characteristics of the $NbAl_3$ phase since it is the only intermetallic that forms Al_2O_3 when oxidized at high temperatures (T>1000°C), however this phase cannot sustain the growth of a protective oxide layer (Hebsur, Stephens, Smialek, Barrett, & Fox, 1989).

Thus, selective oxidation of the aluminum results in the surface stabilization of the non-protective niobium oxides. It is possible to increase the oxidation resistance of Nb-Al alloys by adding Ti, V or Cr elements that decrease the diffusivity of oxygen and increase that of aluminum in the metal matrix (Perkins, & Meier, 1990). However, high concentration of Al and addition of other alloying elements decrease the melting point of alloy and have negative effects on the alloys' mechanical properties. Hebsur et al. (1989) suggested that alloying of Nb-Al alloys with Cr and Y elements has also positive effects on the oxidation behavior of $NbAl_3$ intermetallic phase.
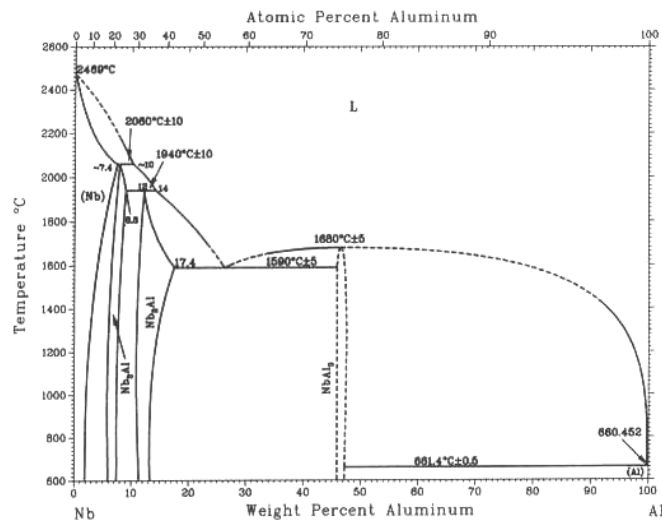
Figure 2.7 Phase diagram of Nb-Al binary alloy

(Baker et al., 1992).

During the latter part of 1980's, attention was directed almost entirely to the development of new alloys strengthened with intermetallic compounds; often referred to as "refractory-metal-intermetallic-composites" (RMICs) or "*in situ*" composites (Bewlay, Jackson, & Subramanian, 1999; Kumar, & Liu, 1993; Subramanian, Mendiratta, & Dimiduk, 1996). Intermetallic compounds, such as Nb or Mo silicides have been combined with metallic phases to produce composites with a balance of attractive high temperature properties and acceptable low-temperature properties (Bewlay, Jackson, & Gigliotti, 2002; Bewlay et al., 2003). As shown in Figure 2.8, three silicides exist in the Nb-Si binary system, among which Nb_3Si is stable only between $1700^{o}C$ and $1980^{o}C$ and decomposes into Nb and Nb_5Si_3 below this temperature range. Nb_5Si_3 exhibits the highest melting point of $2520^{o}C$, existing in two modifications (α-and β-Nb_5Si_3) with a transition temperature of $1940^{o}C$; and $NbSi_2$ is a line compound melting at $1927^{o}C$. Nb-silicide based *in situ* composites with Nb_3Si and/or Nb_5Si_3 silicides have been extensively studied as high-temperature structural materials in comparison with Ni-based superalloys due to their low density (6.6-7.2 g/cm^3), high melting points (~$1750^{o}C$) and high-temperature strength and creep performance (Bewlay, Lewandowksi, & Jackson, 1997). However, the oxidation resistance of some of the niobium silicides is lower than that of $MoSi_2$ because protective SiO_2 scale is not formed at high temperatures. However, $MoSi_2$

has excellent oxidation resistance at high temperatures and is known to show plastic deformation at low temperatures; although, its high-temperature strength is poor. In some studies (Chattopadhyay, Balachandran, Mitra, & Ray, 2006; Chattopadhyay, Mitra, & Ray, 2008), Mo was chosen as the ternary alloying element in the Nb-Si system because it improves the strength, fracture toughness and hardness of the metallic phase while preventing the formation of metastable phase, Nb_3Si through the eutectic reaction.
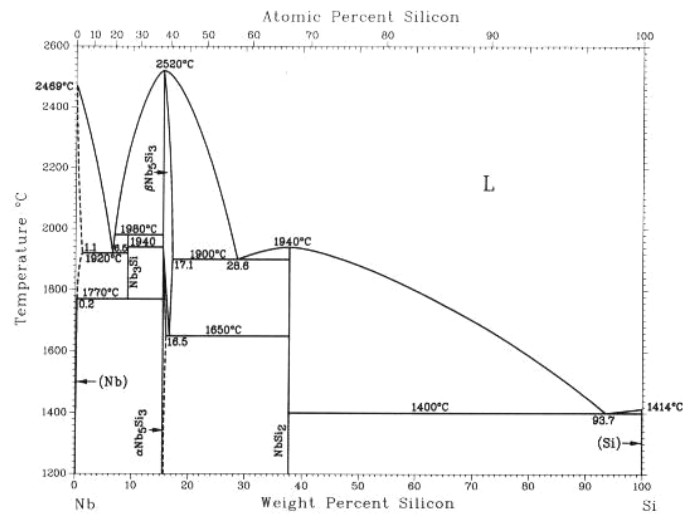
Figure 2.8 Phase diagram of Nb-Si binary alloy
(Baker et al., 1992).

Pesting which causes brittleness in some silicides at low temperatures has been observed for $NbSi_2$ and $MoSi_2$ intermetallics (Chou, & Nieh, 1993; F. Zhang, L. Zhang, Shan, & Wu, 2005). Bewlay et al. (2003) suggested that the Al and Hf additions can reduce the pesting damage. Also alloying with Sn was found to be effective in managing pesting of the silicide-based composites at intermediate ($750^{\circ}C$-$950^{\circ}C$) temperatures (Geng, Tsakiropoulos, & Shao, 2007; Vellios, & Tsakiropoulos, 2007). The low temperature pesting behavior of some of these composites is an important issue for their development as high temperature materials.

To enable Nb-silicide based alloys to have balanced properties, the concept of "multiphase" alloys has been considered (Chan, 2005). This approach involves the

incorporation of ductile Nbss (bcc solid solution), with stiffening intermetallics, such as Nb_5Si_3 and Laves phase Cr_2Nb, to form a multiphase $Nbss/Nb_5Si_3/Cr_2Nb$ eutectic microstructures, in which the "ductile" Nbss phase offers ductility and fracture resistance at ambient temperature and the Nb_5Si_3 and Cr_2Nb phases supply high-temperature strength and oxidation resistance, respectively, at elevated temperatures (Brady, Zhu, Liu, Tortorelli, & Walker, 2000; Takasugi, Hanada, & Yoshida, 1995; Takeyama, & Liu, 1991; Varma, Parga, Amato, & Hernandez, 2010).

Again Bewlay et al. (2003) have reported that Si is the most beneficial element in reducing the oxidation losses in niobium silicide-based in situ composites, followed by Cr and Ti additions. Chromium and Al improve the oxidation resistances of both the silicide and the Nbss phases but are detrimental for the fracture toughness of the Nbss (Sha, Liu, & Zhou, 2010). Addition of Ti provides solid solution strengthening, improves the fracture toughness of the Nbss, enhances the oxidation resistance of both the silicide and the Nbss, and decreases the alloy density. However, the Ti concentration should not exceed 25 a/o in order to maintain the high melting point of the alloy above 1750°C and avoid the formation of the Ti_5Si_3 phase which has reported to be detrimental to the creep of Nb-silicides.

In some studies, Nb-Si composites are alloyed with Ti, Cr, Hf, Al, Mo and Sn to get a better balance between room and high temperature properties (Geng, Tsakiropoulos, & Shao, 2006; Yao, Cai, Zhou, Sha, & Jiang, 2009). Transition metals such as Ti, Cr, Hf additions reduce oxygen solubility and diffusivity of interstitials in the alloy and slow down its embrittlement at elevated temperatures. A multi-component Nb-Si-Ti-Hf-Cr-Al system has been developed by General Electric Co. to optimize the alloy properties (Jackson, 1991).

Recently, researches have focused also on the effect of B addition on the oxidation and mechanical properties of Nb-silicide and Mo-silicide based alloys (Benedict, & Varma, 2010; Dimiduk, & Perepezko, 2003; Ventura, & Varma, 2009). In a few studies, alloying Nb silicide based alloys with B has been reported to

improve their high temperature oxidation behavior (Behrani, Thom, Kramer, & Akinc, 2006; Jun, Xiping, & Jinming, 2009).

2.7 Pack Boronizing of Refractory Metals

Some metals are weak in their pure state to fulfill requirements of some applications such as hardness, wear and oxidation resistance. Although alloying and complex heat treatment procedures can improve mechanical and physical properties, surface treatment is needed to improve wear and corrosion resistance of pure metals (Mu, Yang, Shen & Jiang, 2009; Usta et al., 2006). One of the surface improvement methods that are applicable to metallic materials is boronizing (Sahin, & Meric, 2002).

Boronizing (or boriding) is a thermochemical surface treatment where boron atoms are diffused into the metal substrate to form extremely hard and wear-resistant metallic borides on the substrate surface (Hausner, 1966). Boronizing can be carried out in different ways, including plasma-based boronizing, gaseous boronizing, molten salt boronizing, paste (consists of B_4C, cryolithe and water) boronizing and pack boronizing (Campos et al., 2006, Uslu et al., 2007; Kuznetsov et al., 2004). Pack boronizing is the most common method and has the advantages of simplicity, the flexibility of the composition of the powder, minimal equipment and cost-effectiveness. It has also some disadvantages; the distribution of boron is not uniform and the sample surfaces need to be cleaned (Hausner, 1966).

The pack (boriding media) contains a source of boron, usually boron carbide (B_4C) or amorphous boron, an alkali-halide activator (NH_4Cl or KBF_4) to deposit atomic boron in the substrate and an inert diluting agent (SiC) to prevent caking and sintering of the powder to the substrate. During the process, the sample is placed in a sealed container containing powder mixture. The container is heated up to the required (850-1050°C) temperature and kept at that temperature for the prescribed time (2–10 h), and finally cooled (Hausner, 1966; Mu et al., 2009).

Since boron is a relatively small element, it is possible to apply the boronizing process to a wide range of materials including ferrous (structural steels, cast steels, gray and ductile iron, and sintered iron and all kind of steels) and non-ferrous (nickel-, cobalt- and titanium-based) alloys, mainly, to improve their wear resistance (Mu, & Shen, 2010). The formation of the metal boride enhances the other surface properties such as hardness, corrosion resistance and high temperature oxidation resistance up to 850°C (Lei et al., 2000; Mu et al, 2009).

The presence of alloying elements reduces the diffusivity of boron and consequently decreases the thickness of the borided layer. Boronizing behavior of multicomponent alloys have been shown to be complex because the morphology, phase composition, micro hardness and other properties of the boride layers are affected by the alloying elements. For example, in steel, while carbon, molybdenum and tungsten dramatically reduce the borided layer thickness, silicon, chromium and aluminum have moderate influence, and nickel, manganese and cobalt have only marginal influence. Chromium either enters iron borides or accumulates at the interface between the boride coating and steel and also forms a distinct CrB boride layer. Nickel concentrates underneath the boride coating and enters the Fe_2B phase. Titanium increases the effectiveness of the boron on the hardenability of steel. It is also well known that a titanium–boron compound like titanium boride has very high hardness, high melting temperature and chemical inertness (Hausner, 1966).

Boronizing has been applied to transition metals like titanium, tantalum, niobium, molybdenum, tungsten and chromium to obtain a boride coating on their surfaces (Usta et al., 2006). The strong covalent bonding in most transition metal diborides is responsible for their high melting points, high mechanical strength, elastic modulus and hardness values. They have high free energy of formation, which gives them excellent chemical and thermal stability under many conditions (Hausner, 1966). Table 2.11 shows some of the properties of borides of the transition metals. In the literature, several studies have reported the siliconizing and aluminizing of refractory metals (Alam, Rao, & Das, 2010; Weber, Bouvier, & Slama, 1973). However,

research on the boronizing and influence of a boron coating on oxidation resistance of refractory metals is still limited.

Table 2.11 Some physical properties of the borides of transition metals (Hausner, 1966).

Metal Borides	Melting Point, ^{o}C	Micro hardness, kg/mm^2	Coefficient of linear expansion (0-1200°C), $\alpha.10^6/^{o}$C	Thermal conductivity, cal/cm.^{o}C.sec	Resistivity, $\mu\Omega$. cm
TiB$_2$	2980	3370	8.1	0.063	14.4
ZrB$_2$	3040	2250	6.88	0.058	16.6
HfB$_2$	3250	2900	5.73	-	8.8
VB$_2$	2400	2800	7.5	-	19
NbB$_2$	3000	2600	7.9-8.3	0.047	34
NbB	2280	2195	-	-	64.5
TaB	2430	3130	-	-	100
TaB$_2$	3100	2500	11.4	0.033	37.4
CrB$_2$	2200	1785	11.1	0.053	84
MoB	2500	1570	-	-	50
MoB$_2$	2100	1380	-	-	45
Mo$_2$B	2140	2500	-	-	40
Mo$_2$B$_5$	2100	2350	-	0.064	18
W$_2$B$_5$	2300	2660	-	0.76	43

Under any conditions, the depth of the borided layer is maximum on molybdenum and much less on tungsten, niobium, zirconium, tantalum and rhenium. On molybdenum, and tungsten, layers of a thickness of up to 100μ were reported to retain relatively strongly, and practically did not crumble during the preparation of polished sections. Boride layers on tantalum and niobium have been found to be dense, nonporous and adhere strongly to the metal. Even at temperatures of 1400°C and 1500°C, no cracks extending to the surface of these metals were observed. However with increasing thickness, the boride layers became brittle, contained porosity and number and size of the cracks increased, while their bonding to the metal deteriorated (Hausner, 1966).

Depending on the boronizing process parameters, it has been shown that it is possible to form different boride phases for both Nb and Mo metals. Binary phase diagrams of these two metals are given in Figure 2.9 (a) and (b).
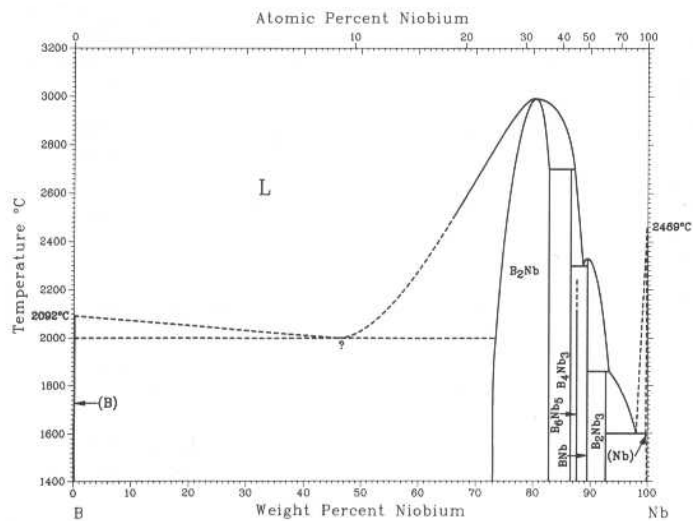
(a)
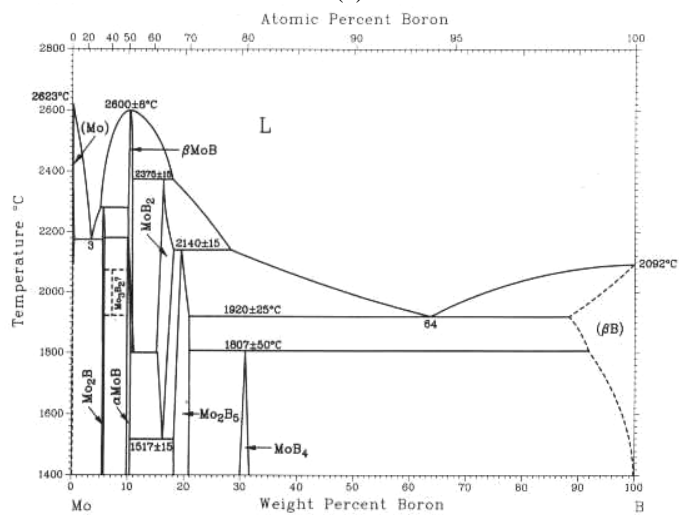
(b)

Figure 2.9 Binary phase diagrams of (a) Nb-B and (b) Mo-B
(Baker et al., 1992).

CHAPTER THREE
EXPERIMENTAL PROCEDURE

3.1 Materials Used and Alloy Production with Vacuum Arc Melting

High purity raw materials such as Mo (99.95%), Nb (99.95%), Cr (99.9%) and Ti (99.9%) used in alloy production were bought from the Alfa Aesar Company. In the first part of this study, bulk (slug, pieces or plate) raw materials (charge) were used. They were cleaned ultrasonically in acetone then dried quickly in flowing warm air and weighed using a balance with 0.1 mg sensitivity before the melting process.

In the second part, high purity (>99.95) powders (-325 mesh) of these metals were used to enhance the homogeneity of alloys. Powder mixtures were prepared inside a glove box filled with nitrogen (N_2) gas. Mixing of powders was done for 1h at room temperature inside a container rotating at a speed of 250 rpm. A stainless steel mold is obtained to prepare the powder pellets (Figure 3.1 (a)). The ring-shaped mold is placed on the die part and powder is put inside the mold and compacted using the press shown in the Figure 3.1 (a), (b). During compacting, pressure is applied to the mold in two stages. In the first stage, a low pressure (10 MPa) is applied to remove the remaining air in the powder for better shaping. In the second stage, a pressure of 25 MPa is applied to form the disk-shaped powder compacts of approximately 20 mm in diameter. After compacting, the mold is turned upside down to remove the pellet (Figure 3.1 (c)). Thicknesses of the pellets were between 1-3 mm depending on the amount of powder used.

Melting of both the bulk and pellet samples was done inside the water-cooled copper hearth of a laboratory type vacuum arc melting (VAM) furnace (Edmund Bühler Model) (Figure 3.2) which uses a non-consumable tungsten electrode.
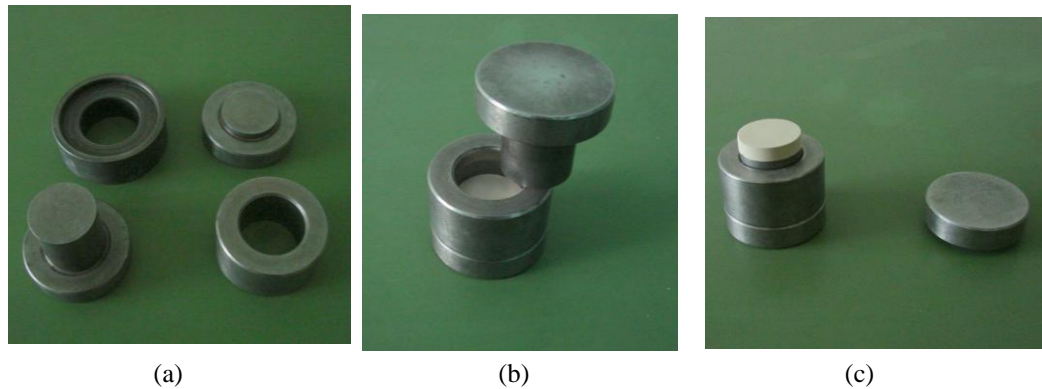
Figure 3.1 Mold pieces which are used during sample preparation from powder raw materials.

In this system, materials with very high melting points and/or materials which are susceptible to oxidation can be melted under a protective inert gas (Argon) atmosphere. The unit has two vacuum pumps. The pre-evacuation of the chamber is done by a rotary pump up to approximately 10^{-3} mbar. Then a diffusion pump is employed for further pressure reduction down to 1.5×10^{-5} mbar. The chamber was purged at least three times with high purity Ar gas prior to melting. A Ti button was used as an oxygen getter and it was melted before the sample. The melting process was generally repeated several times to prevent segregation and enhance the chemical homogeneity of the final product. A sample manipulator attached to the chamber was used to overturn the samples *in situ* without having to open the chamber and thus preventing the introduction of air into the chamber.
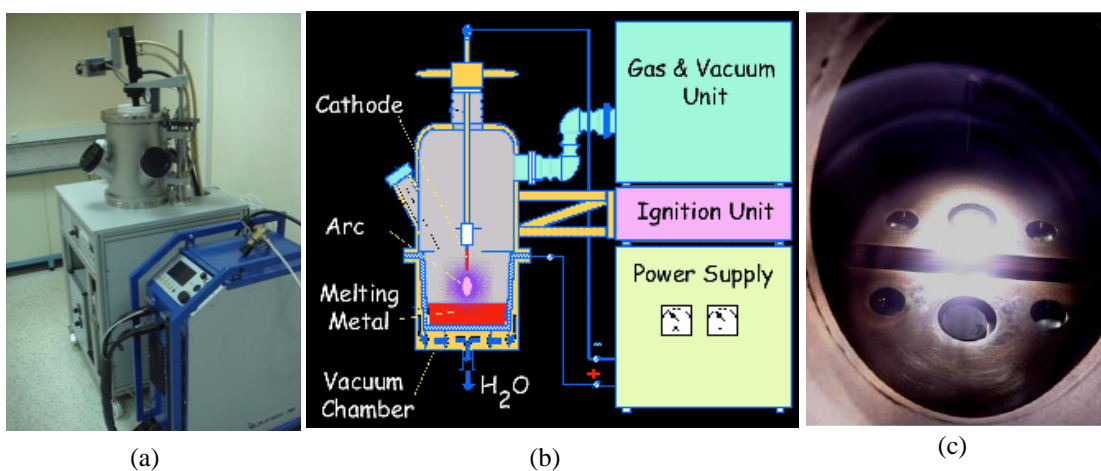
Figure 3.2 (a) Photograph (b) schematic representation and (c) copper crucible molds of vacuum arc melting (VAM) furnace.

During the melting of the bulk materials, evaporation of some of the alloying elements such as Al, Si and Cr was observed because of their relatively low melting and vaporization temperatures. In order to determine sample weight changes during melting, bulk or pellets and ingots were always weighed carefully before and after melting.

Alloys production was also conducted using the Electron Beam Melting (EBM) equipment available in the Process Metallurgy and Metal Recycling Laboratories (IME) at RWTH, Aachen, Germany. Objective of these studies was to produce alloys with better microstructures and in quantities enough to make samples for high temperature corrosion studies. The EBM equipment was a LEYBOLD AG ES1/3/60 Model Electron Beam Furnace shown in Figure 3.3 (a). Button-shaped alloy samples were prepared inside the water-cooled copper crucibles (Figure 3.2 (b)) in the furnace. The equipment uses a single focused electron gun (60 kW- 2 A) as a heat source instead of the non-consumable tungsten electrode as the case for VAM. The EBM chamber can be evacuated to nearly 1×10^{-6} mbar total pressure by a turbo molecular pump which provided a better processing environment compared to the VAM system. In Figure 3.3, some of the alloy samples made in this system are shown.

For alloy production in the EBM system, refractory metals (Nb, Mo, and Cr) and alloying elements such as Ti were used. Raw materials were cleaned ultrasonically, in n-hexane-cyclohexane solution, dried quickly in flowing warm air and weighed using an electronic balance (Mettler) with 0.01 mg sensitivity. Each button-shaped ingot was made after melting at least twice (before and after inverting the ingot). Excluding the time spent for beam focusing and charge heating, the total melting time for two melting cycles was approximately 6-8 min. for each sample. Here, the "melting cycle" refers to the time during which the full beam power was applied to the liquid charge pool. At the end of each melting cycle, weight changes of the samples were measured carefully.
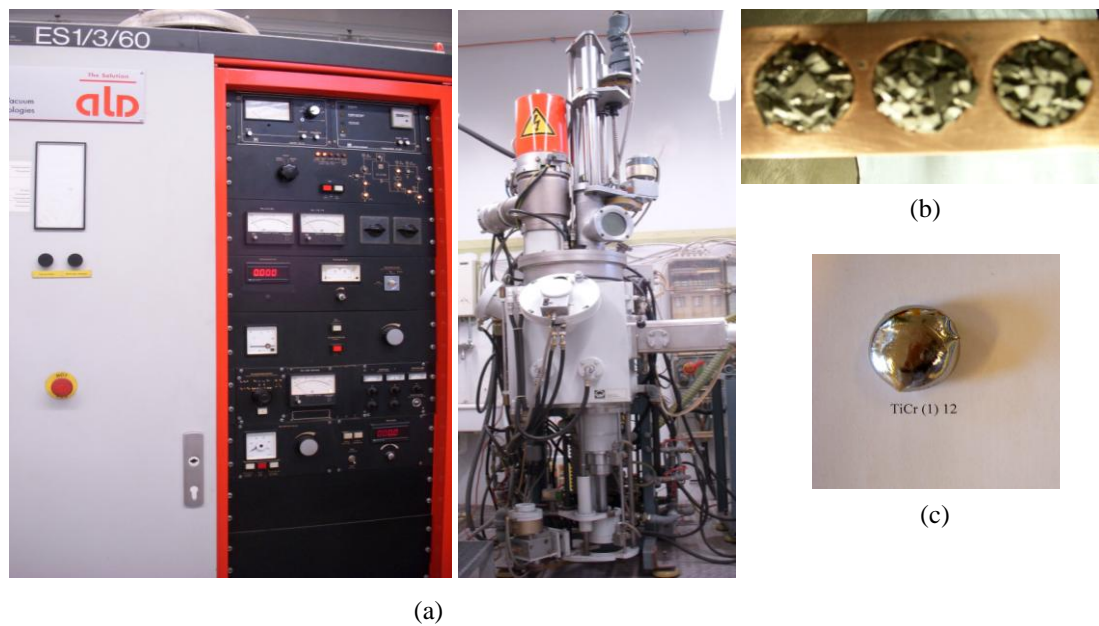
Figure 3.3 (a) The EBM equipment, (b) water-cooled Cu crucibles with pure Mo and Nb starting materials, (c) a button-shaped TiCr alloy ingot produced during the study.

It was observed that material loss from the alloys was large during the electron beam (EB) melting method. This is believed to be related, mainly, to the high vacuum conditions required for the transport of electrons in the EB equipment. Another reason for this was the different melting points of the elements present in the binary alloys. When elements with very high melting points were melted together with elements with lower melting points, it was easier for the lower melting point element to vaporize during melting by EB. Movement and spallation of materials from the melting crucibles in the EB equipment also caused some material losses. Nevertheless, because of the better control of the electron beam, it was possible to prepare large size homogeneous alloy samples with the EBM equipment. However, for most of the work conducted in this Thesis, focused on the alloys produced by VAM method.

For the characterization studies such as metallographic observation of alloy microstructures, chemical composition analyses, phase identification and oxidation tests, of the produced alloys, all ingots were sectioned into pieces by an EDM (electro-discharge machine) to obtain proper samples.

3.2 Atmosphere Controlled Furnace System

The construction of a test furnace with controlled atmosphere was realized for two purposes. The first one is the annealing (heat treatment) of the ingots to improve their microstructure and properties. The second purpose was the conducting of pack-boronizing of the selected metal and alloy samples to enhance their oxidation resistances.

3.2.1 Annealing (Heat Treatment)

The atmosphere controlled furnace system designed for this purpose (Figure 3.4) consists of two parts. The first part supplied annealing environment gases such as Argon from the gas tanks. Flow of gases is controlled using pressure regulators. Argon gas flow rate through the pipes is controlled by valves and flow meters. In the second part, there is an annealing furnace equipped with a quartz reaction tube and gas-tight caps. At the both ends of the reaction tube, these caps allowed gas inlet, outlet and attachment of a thermocouple. To obtain a mixed gas environment, two or three different gas tanks can be connected to this system. Separate flow meters and a mixing tube can be used to mix different gases to prepare gas mixtures. This heat-treatment system is shown schematically in Figure 3.5.

Figure 3.4 The photograph of the atmosphere controlled system.
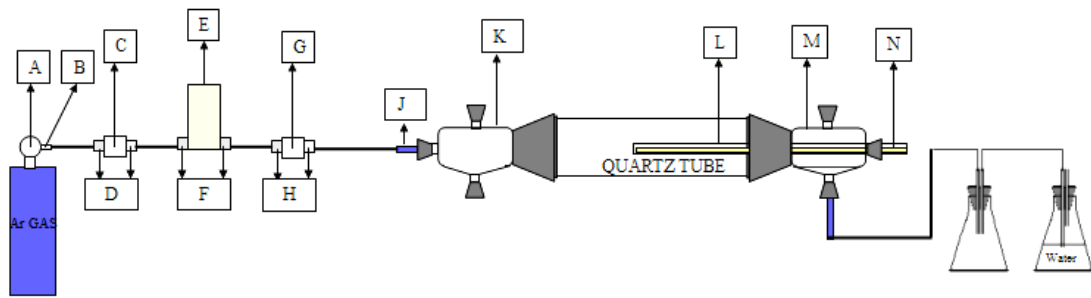
A: Regulator

B: Fixing parts of the gas flow form the
regulator to the gas flow tube

C: Security valve

D: Fixing parts between the valve and gas tube

E: Flow meter

F: Fixing parts of the flow meter

G: Security valve

H: Fixing parts between the valve and gas tube

J: Glass fixing parts between plastic pipe and
borosilicate gas-tight

K: Borosilicate gas tight

L: Quartz pipe for thermocouple

M: Borosilicate gas tight

N: Thermocouple

Figure 3.5 Schematic representation atmosphere controlled system for heat treatment (HT) process.

Before the tests, the calibration of the flow meter was made for Ar gas which is mostly used as the protective gas. The flow rate of the gas was read from the calibration chart prepared for the flow meter (Figure 3.6).
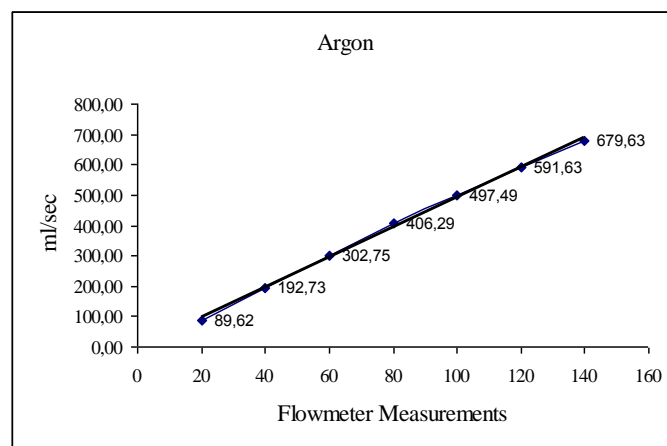

Figure 3.6 Calibration curve for the Ar flow meter.

In the annealing tests, samples were placed inside a ceramic boat and another ceramic boat was turned upside down and placed over the boat containing the

samples. Next to the boat containing the samples, a different ceramic boat containing Ti metal pieces were placed so that the oxidizing impurities in the gas environment could be collected by the Ti (getter) pieces in the boat. Before heating the furnace, the reaction tube was flushed with Ar gas for approximately 30 min. Samples were kept at high temperature (T$\geq$1000°C) under the Ar gas environment for a predetermined time before cooling to room temperature inside the furnace. Argon gas passed through the furnace tube during the entire testing. Flow rate of the Ar gas during the test was generally set to 50 (220 ml/min).

Annealing of the alloys was also conducted in a sealed evacuated quartz capsules. For this method, a quartz tube with a diameter of 12 mm and a thickness of 1 mm was used. Besides the samples, Nb, Mo, Ta and/or Ti plate were put inside the tube as getter elements. Before closing of the tube, surfaces of the samples were wet polished using SiC paper and diamond paste followed by cleaning in acetone. After placing the samples inside, the quartz capsule was flushed with Ar gas and evacuated 2-3 min. using a rotary pump. This cleaning process was repeated 5 times before sealing the tube under vacuum. A schematic of the condition of the quartz tube is shown in Figure 3.7. This sealed tube was later placed inside the high temperature furnace. After cooling, samples were removed from the quartz tube and both surfaces of the samples were wet polished using SiC paper and diamond paste for microstructural analyses.
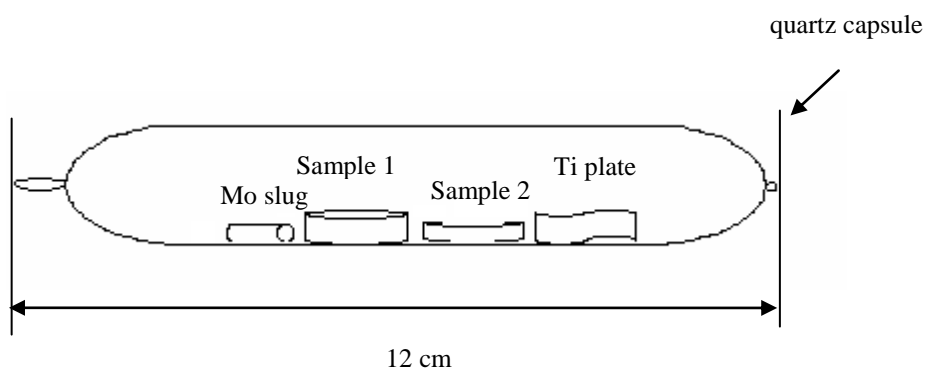

Figure 3.7 Schematic representations of the samples in a sealed quartz capsule.

It was observed then the quartz capsule was much more effective method compared to the annealing in atmosphere controlled system regarding the prevention of samples from oxidation.

3.2.2 Pack-Boronizing

Boronizing tests were performed in a solid medium by using commercial Ekabor-II powder that had a nominal chemical composition of 90% SiC, 5% B_4C and 5% KBF_4. Samples were placed in contact with the powder mix and then transferred to an electrical resistance furnace in a stainless-steel container. Boronizing of pure metals was performed in the atmosphere controlled furnace at 950°C for 4h, 5 h and 6h respectively, followed by air cooling. Boronizing tests were also performed on some selected alloy samples in the atmosphere controlled furnace at 950°C for 8h. Flow rate of the Ar gas during all tests was set to 50 (220 ml/min).

3.3 Oxidation Tests

Oxidation tests were performed on the produced alloy samples as well as the pure Mo and Nb metal samples. Both box and tube furnaces were used for this purpose. Before each oxidation test, surfaces of the samples were wet polished using SiC and alumina abrasives. For oxidation tests, the sample was placed inside a ceramic boat. Another boat was turned upside down and placed over the boat containing the sample to decrease the access of the oxidizing impurities in the furnace atmosphere to the samples. Oxidation tests for these samples were conducted at 300, 500, 600, 700, 800°C. In each test, the sample was heated to the test temperature and kept at this temperature for 30 min. Samples were removed from the furnace and cooled outside the furnace. Additional tests were performed on pure Mo and Nb metals and some as-cast and boronized (B) alloy samples at 800, 900, 1000°C for 30 min.

After each oxidation test, the weight of the sample was recorded after carefully removing it from the boat or the crucible. Corrosion products (oxide scales) which

spalled off from sample surfaces were collected as much as possible and weighed separately.

3.4 Sample Characterization Equipments

3.4.1 Scanning Electron Microscope (SEM) and Energy Dispersive Spectrometer (EDS)

The surface morphologies and microstructures of the samples were investigated by a Scanning Electron Microscope (SEM) (JEOL-JSM 6060). SEM was used in two different modes: the secondary electron (SE) and the back scattered electron (BE) imaging. Secondary electron (SE) signal is used to generate high-resolution images of surfaces.

In the BE mode, high atomic number atoms in the material scatters many electrons. Thus, location and distribution of the heavy and light elements can be observed. Spectrum and depth of escape of backscattered electrons are directly related to the atomic number of the elements in the samples.

Composition of samples and product phases were determined by using the IXRF System Model energy dispersive X-Ray spectrometry (EDS) attached to the SEM. EDS is an analytical technique used for elemental analysis of samples. It is a technique based on collection and evaluation of the characteristic X-ray energies emitted from the atoms in the sample. These X-rays are converted into electronic signals by a Si (Li) crystal in the EDS detector is attached to the SEM.

3.4.2 X-Ray Diffractometer (XRD)

X-ray diffractometer is used to determine the crystalline phases in the alloy samples as well as the oxidation and boronizing products. Each crystalline material, when exposed to radiation by X-ray source, produces a unique and different X-ray diffraction signal. Phases and compounds in the sample are determined using the

database provided with the Rigaku D/Max-2200/PC Model X-ray diffractometer with CuKα radiation. The 2θ angular scans of the samples were generally performed within the range of 3-90°.

CHAPTER FOUR
RESULTS AND DISCUSSION

4.1 Results and Discussion for Pure Refractory Metals

In the first part of this study, oxidation behavior of (1) as-received and (2) boronized Mo and Nb metals were investigated. For this purpose, as-received Mo and Nb metal slugs (small cylinders) were used. Conditions of both the isothermal oxidation tests and the boronizing tests are explained in Chapter 3. Before the oxidation tests, all surfaces of the as-received slugs were polished and cleaned with acetone, ultrasonically. The boronized metal samples were also cleaned in acetone before oxidation.

4.1.1 Results and Discussion for As-Received Pure Refractory Metals

4.1.1.1 Results and Discussion for As-Received Molybdenum

Prior to high temperature tests, oxidation tests were conducted on an as-received Mo slug at temperatures lower than $800^{o}C$ to observe its low temperature oxidation behavior. After the 30 min. test at $300^{o}C$ most of the surface of the sample had a bright metallic gray color. However, a small area at the surface had black color. Other scientists who oxidized Mo metal at lower temperatures reported that MoO_2 and other sub-oxides such as MoO_z, where $2<z<3$ formed between $450^{o}C$ and $650^{o}C$ (Smolik, Petti, & Schuetz, 2000). These observations suggested that the layer observed on the Mo sample surface after the $500^{o}C$/30 min. test could be an oxide layer containing both the MoO_2 phase and the MoO_3 phase. This suggestion is supported by the observation that while negligible mass gains were recorded during oxidation below $600^{o}C$, significant vaporization from the sample was also seen above $700^{o}C$ indicating the presence of the MoO_3 phase. Also, yellow stains were visible at the inner surfaces of the top ceramic boat covering the boat containing the Mo samples. Surprisingly, no scale spallation was observed during the tests up to

800°C. Above this temperature, the oxidized Mo sample was found to have strongly adhered to the ceramic boat.

The second group of tests which were started at 800°C showed evidence of a molten oxide formation underneath of the sample that was exposed, inside a quartz boat, to stagnant air for 30 min. During the test, dimensions of the cylindrical sample changed. Molten oxide flowed down the sample as shown in Figure 4.1 (a) and (b). This observation agrees with the Mo-O phase diagram in Figure 2.2 which shows that the MoO$_3$ phase melts at 795°C while liquid MoO$_3$ and solid MoO$_2$ phases form.

5mm	5mm	5mm
(a)	(b)	(c)
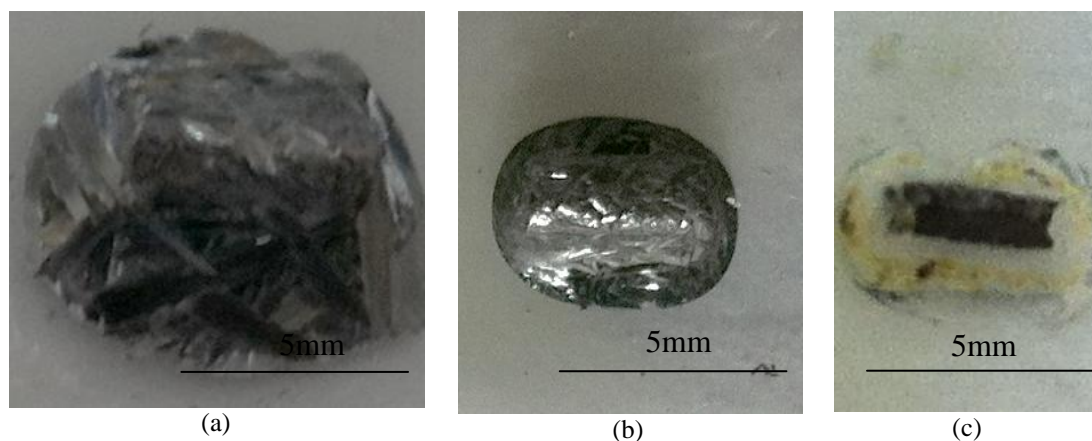
Figure 4.1 Pure Mo samples after oxidation tests at (a) 800°C, (b) 900°C, (c) 1000°C for 30 min.

In Figure 4.1 (b) and 4.1 (c), the appearance of the sample after 900°C and 1000°C/30 min. tests is shown. After 1000°C, the sample became smaller, but not completely consumed. After the test at 1000°C, transparent and fiber-like structures were observed over the internal surfaces of the alumina furnace tube containing the samples.

According to the literature, at high temperature (T>800°C), MoO$_2$ is solid and MoO$_3$ is liquid. Upon cooling of the alloy from such a temperature two distinctive molybdenum oxide morphologies could be observed. One of them has a facetted and crystalline appearing morphology while the other one has spherical and the molten appearing morphology (Helmick, 2003). In this study, the appearance of the pure Mo surface after oxidation test at 800°C is shown in Figure 4.2 (a). As seen in the micrograph, the surface was covered with band-shaped oxide products. Figure 4.2 (b)

shows a high magnification SE image of this oxide structure. According to the EDS analysis, there were 63.3% Mo and 36.7% O in this scale. XRD result supported that the molten oxide seen in Figure 4.1 (a) is crystalline MoO_3, and no MoO_2 phase was detected.

(a)   (b)
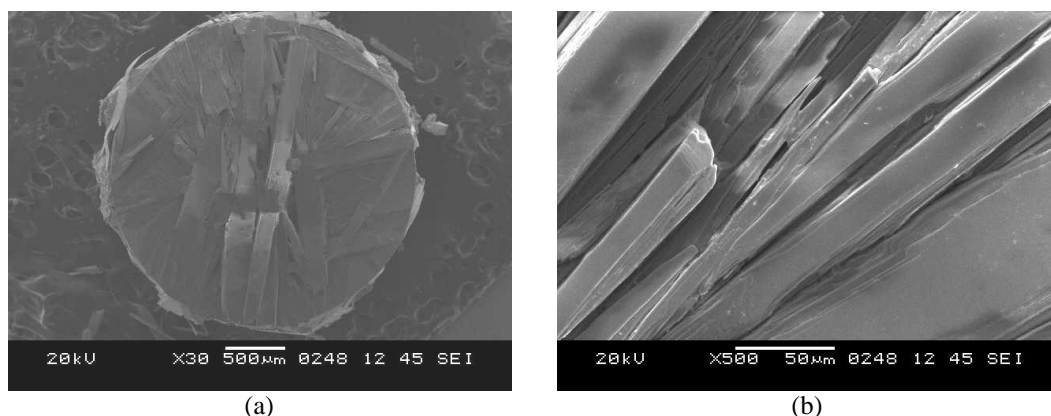
Figure 4.2 (a) a general and (b) high magnification SEM micrograph of pure Mo after oxidation test at 800°C for 30 min.

4.1.1.2 Results and Discussion for As-Received Niobium

For the oxidation of as-received Nb, slug samples were used. The first sample was exposed to air for oxidation between 300°C and 800°C inside a ceramic boat while the second sample was oxidized inside a quartz boat in air between 800°C and 1000°C. Figure 4.3 shows SEM micrograph of the pure Nb sample after the oxidation test at 800°C inside ceramic boat. As seen in the figure, a thick and poorly adhered oxide layer surrounded the sample. The top flat surface of the cylindrical slug sample in the same picture also had a similar oxide. However, this thick layer spalled off the surface during sample handling. The scale had a metallic gray color. Morphology of the oxide that grew over the side surfaces of the sample was observed to have rod-shaped structures which appeared to have grown layer by layer over the surface.

(a)   (b)
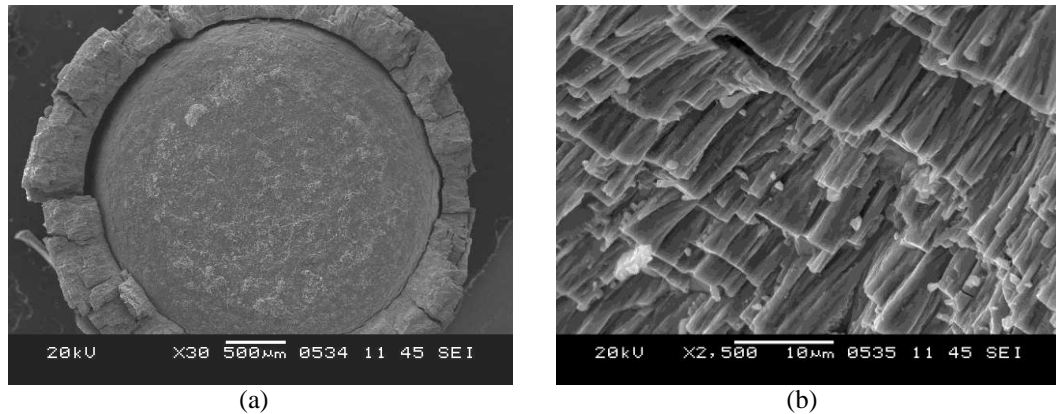
Figure 4.3 (a) Low and (b) high magnification SEM micrographs of pure Nb after oxidation test at 800°C for 30 min.

According to the literature, as in our study, a cream-colored oxide starts forming over pure Nb at above 450°C (Argent, & Phelps, 1960). In this study, after the 600°C/30 min. test, the surface of the sample was completely covered with a white oxide layer. Small amount of oxide spallation was observed after the test at 600°C. The oxide layer thickness increased with temperature. It is known that spallation of the scale is expected when the thickness of the scale reaches a critical thickness (Stringer, 1973). As seen in Figure 4.4 (a)-(c) spallation became significant with increasing temperature, possibly due to the fact that the critical thickness was reached earlier at higher temperatures.

(a)   (b)   (c)

Figure 4.4 Photograph of pure Nb after oxidation tests at (a) 800°C, (b) 900°C, (c) 1000°C for 30 min.

Compared to Mo-oxides, melting temperatures of Nb-oxides (NbO, NbO$_2$ and Nb$_2$O$_5$) are higher. Therefore, during the oxidation of pure Nb slug, melting of and vaporization of oxide phases were not observed. Although the oxide layer formed on

Nb was not protective enough because of its porous structure and spallation, the scale provided some protection unlike the low melting oxides of Mo.
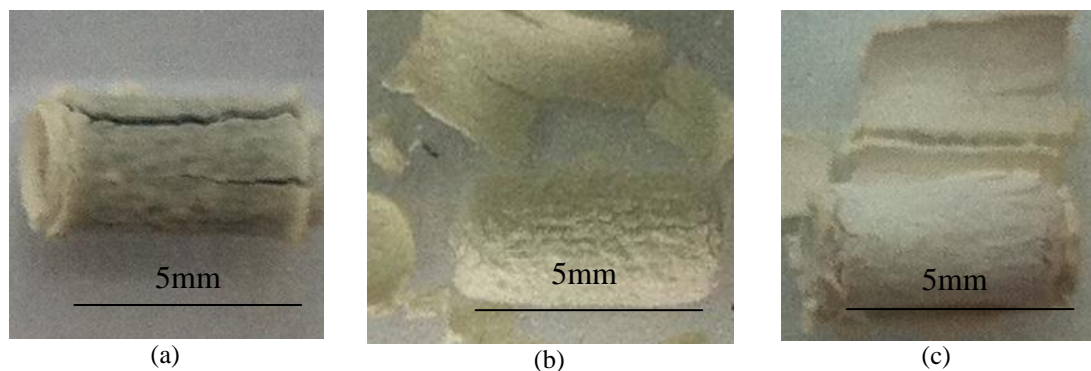
4.1.2 Results and Discussion for Boronized Refractory Metals

For these tests both as-received cylindrical slug samples and plate samples were used. The plate samples were sliced from the ingots produced by VAM under laboratory conditions.

4.1.2.1 Results and Discussion for Boronized Molybdenum

Cross-sectional SEM micrographs obtained in the backscattered electron (BE) mode for the boronized Mo slugs at 950°C for 4 and 6h are given in Figure 4.5. In the BE image, contrast arises from the difference in atomic numbers of the elements, with brighter areas indicative of the presence of heavier elements. Whereas the darker areas indicate enrichment by the lighter element; boron. The interface between this enriched layer and the pure Mo substrate was observed to have a smooth structure in Figure 4.5 with negligible amount of cracking. Formation of cracks is thought to be the result of differences between the thermal expansion coefficients of the boride layer and pure metal. The thickness of the boride layer was uniform over the sample. The average thickness measured for the boride layer was 15 μm. It is known that the thickness of such a layer depends on the time and temperature of the diffusion process (Mu et al., 2009). In this study, the chemical composition of the material boronized, process temperature and the nature of the process (pack boronizing) were fixed, making the boronizing time as the only parameter that was changed. Thus, it was observed that by increasing the process time from 5h to 6h at 950°C, the average thickness of the coating layer increased from 17 μm to 25μm.

In Figure 2.9 (a), the Mo-B binary phase diagram is shown. Depending on the boronizing parameters, it is possible to form different Mo-B intermetallic phases like MoB, MoB_2, Mo_2B, MoB_4 and Mo_2B_5 on the pure Mo substrate. However, the XRD

analysis results shown in Figure 4.6 for the Mo plate sample boronized for 5h at 950°C shows that only the MoB phase was present over the sample. Since boron atoms can diffuse easily into the metallic substrate because of their relatively small atomic size and mobile nature (Mu, & Shen, 2010), it is possible that the Mo$_2$B phase initially formed at the earlier stages of the boronizing process. However, as the supply of boron continued, the Mo$_2$B phase must have been oxidized to form the MoB phase. In another study, it was suggested that Mo$_2$B acts as a diffusion barrier for boron thus; boron atoms accumulating behind the layer of Mo$_2$B react with this phase and form MoB at the outer regions of the sample (Kuznetsov et al., 2004).
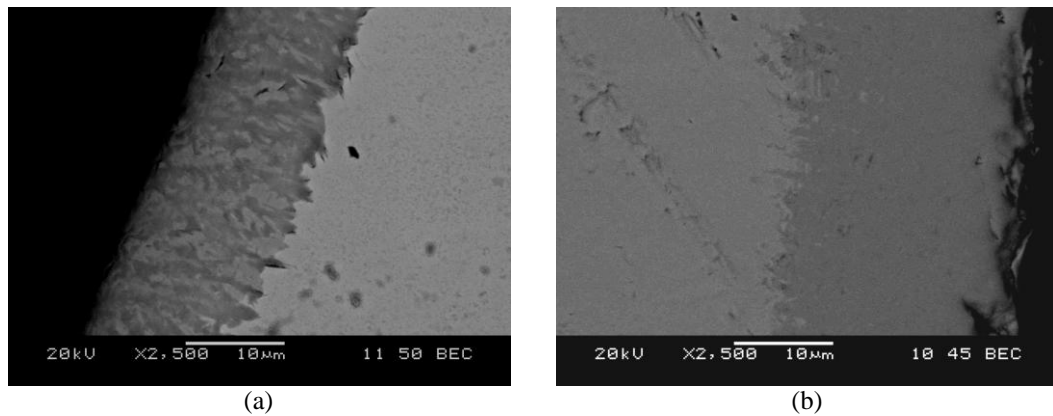

Figure 4.5 SEM/BE cross-sectional micrographs of Mo slugs boronized at 950°C for (a) 4h and (b) 6h.
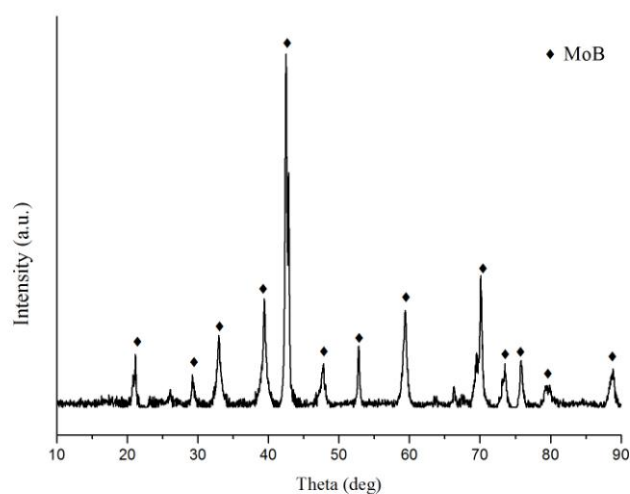

Figure 4.6 XRD diffraction pattern of the pure Mo plate boronized at 950°C for 5h.

In Figure 4.7, appearances of the boronized pure Mo samples are shown after their oxidation tests conducted at 800, 900 and 1000°C. In this test, both the Mo plate that was boronized at 950°C for 5h and the Mo slug boronized at 950°C for 6h were used. In the same test, an unborided as-received Mo slug sample was also oxidized. After the oxidation test of this as-received sample conducted at 800°C, dark gray colored voluminous oxide products were observed over the slug as seen in Figure 4.1 (a). However, after the oxidation of the boronized Mo slug sample, the color of the oxide scale formed was gray but also contained yellow-colored areas (Figure 4.7 (a)). A similar appearing region was also noted underneath this sample. As the oxidation temperature increased, the amount of the yellow region underneath the slug increased while the yellow areas on the sample decreased. It is thought that the formation of these yellow colored regions was the result of both melting of the MoO_3 phase and the boronizing treatment. Yellow-colored areas developed also over the plate samples. However, because of the sample geometry, the molten oxide dripped along the surfaces of the cylindrical slug sample but stayed over the plate sample (Figure 4.7 (d)-(f)).
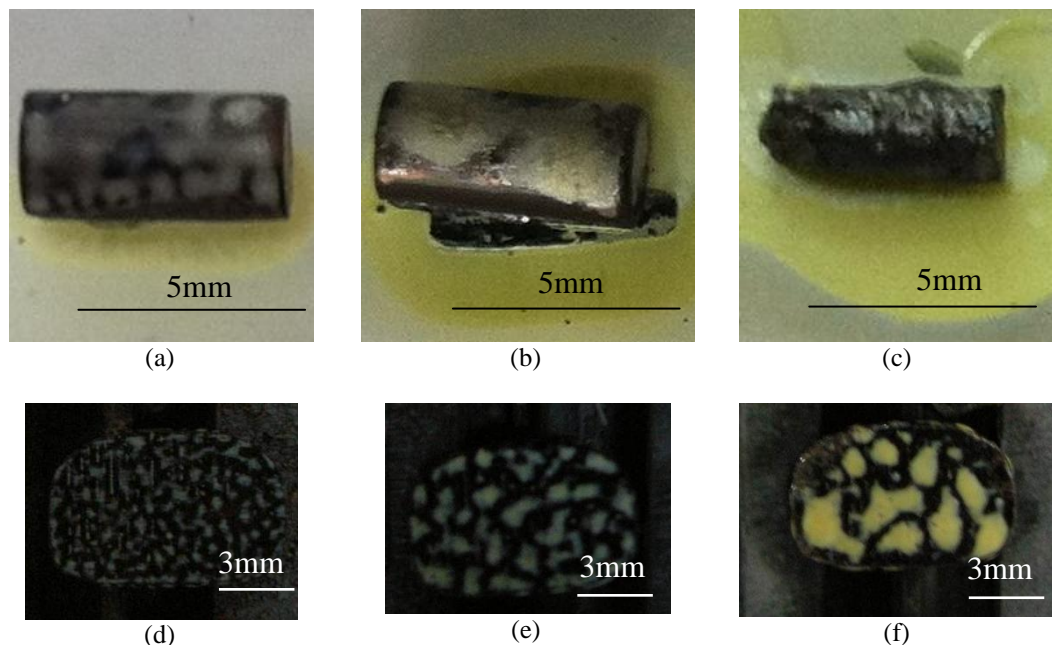

Figure 4.7 Boronized Mo slug (a, b, c) and plate samples (d, e, f) after oxidation at (a, d) 800°C, (b, e) 900°C, and (c, f) 1000°C for 30 min.

At these oxidation temperatures in air both MoO_3 and B_2O_3 phases were expected to be stable in both liquid and gas forms. The presence of boron seemed to have protected the faster degradation of the Mo substrates. As seen in Figure 4.7 (a) and (b), the borided slug sample kept its shape after oxidation unlike the "as-received sample" at the borided plate sample. Since the yellow colored areas on the plate sample increased their size by joining each other. It is concluded that those areas were molten during oxidation and were responsible for the extended life of the Mo substrate. The XRD analysis of the sample shown in Figure 4.7 (f), suggested that a $Mo_{0.1}B_{1.8}O_3$ borate phase and MoO_3 were present over the oxidized plate substrate.

Surface micrograph of the boronized Mo plate oxidized at 1000^oC for 30 min. (Figure 4.7 (f)) is given in Figure 4.8. At the time of imaging, with the electron beam bombardment, charge accumulated on some parts of the sample surface and caused heating and degradation of these areas. According to the EDS analysis, there were 28.8% B, 61.5% O and 9.3% Mo in charging (bright) area labeled by "A" while 52.6% Mo, 40.5% O and 6.8% B in dark area labeled by "B".
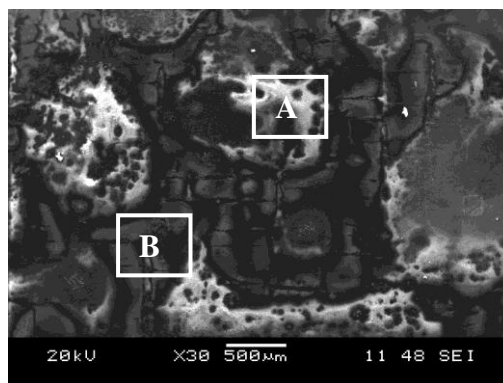
Figure 4.8 Surface SE micrograph of 950^oC/5h boronized Mo plate after oxidation at 1000^oC for 30 min.

4.1.2.2 Results and Discussion for Boronized Niobium

Backscattered electron (BE) cross-sectional micrograph of the "as-received" Nb slug boronized at 950^oC for 4h is given in Figure 4.9 (a). Although the boron-rich

layer formed was not uniform, its average thickness was measured to be about 7µm. Unlike that of Mo, this Nb boride layer had a needle-shaped structure. Some cracks parallel to the substrate were also observed. After boronizing the samples at 950°C 5h and 6h (Figure 4.9 (b)), the average thicknesses of the layers increased to 8 µm and 20µm, respectively.

(a)   (b)
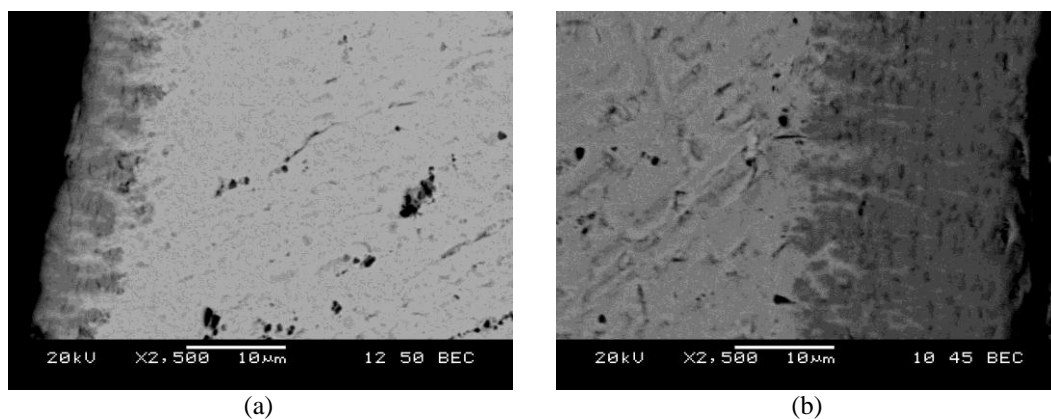
Figure 4.9 (a) BE cross-sectional micrograph of Nb slug boronized at 950°C for (a) 4h and (b) 6h.

In Figure 2.9 (b), the Nb-B binary phase diagram is given while in Figure 4.10, XRD analysis result for the Nb plate sample after boronizing for 5h at 950°C is shown. Although several boride phases are present in this binary system, only NbB$_2$ phase was found after boronizing of "as received" Nb.
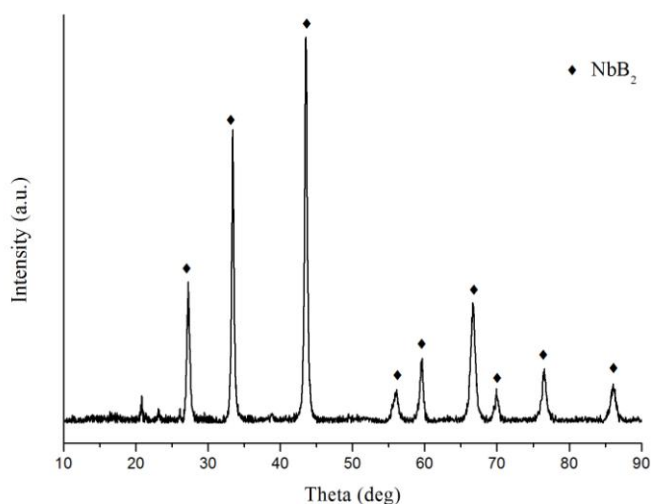
Figure 4.10 XRD diffraction pattern of the pure Nb plate
boronized at 950°C for 5h.

The appearance of the boronized Nb slug after the oxidation tests is shown in Figure 4.11. In the same oxidation test, an unborided as-received Nb slug was also used. In contrast to the cracked and thick oxide products formed over the as-received Nb sample (Figure 4.4 (a)) at 800°C, dark gray colored intact scales formed over the boronized sample after 800°C and 900°C. The oxide layer formed over the boronized sample had a yellow color after 1000°C/30 min. oxidation test. It is thought that, B_2O_3 phase caused to a yellow-colored oxide layer formation. No scale spallation was observed after all these oxidation tests. These results, suggested that the oxide layer formed on the boronized Nb is much more adherent and intact thus, protective compared to the oxide formed on the as-received Nb sample.
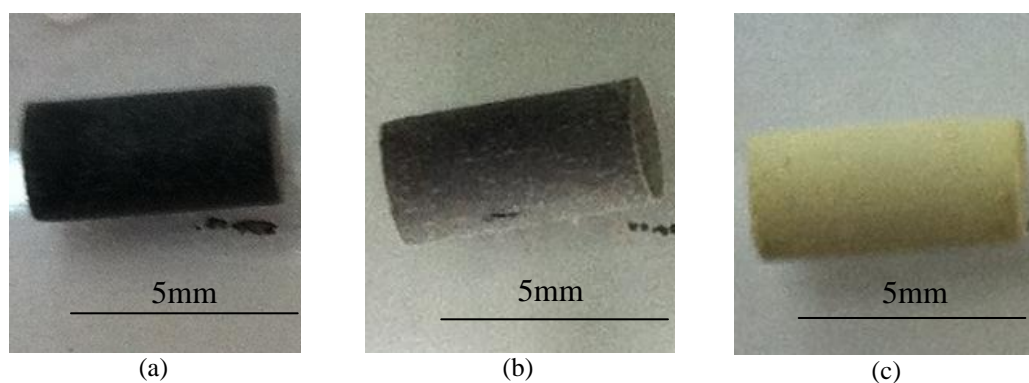
Figure 4.11 Boronized Nb slug after oxidation tests at (a) 800°C, (b) 900°C, (c) 1000°C for 30 min.

Both crystalline B_2O_3 and Nb_2O_5 phases were expected to form upon oxidation of the samples. According to the XRD results, a crystalline Nb_2O_5 phase was present over the boronized plate sample. Beside the Nb_2O_5 phase, another phase was also detected by the XRD. Based on the Nb_2O_5-B_2O_3 phase diagram (Figure 4.12), below 1160°C, the Nb_3BO_9 phase becomes stable. It is thought than the undetermined phase mentioned above could be the Nb_3BO_9 (borate) phase.

It is thought that liquid B_2O_3 formed during the oxidation tests filled the pores in the rod-like structure of the oxide layer formed over Nb. This process may have been the reason of reduced metal oxidation. The dark grey oxide scales which were stuck to the quartz boat also supported this view. The long-rod type structure of the oxide

also seemed to have been changed to a short-rod type structures (Figure 4.13) which might have increased its oxidation resistance.
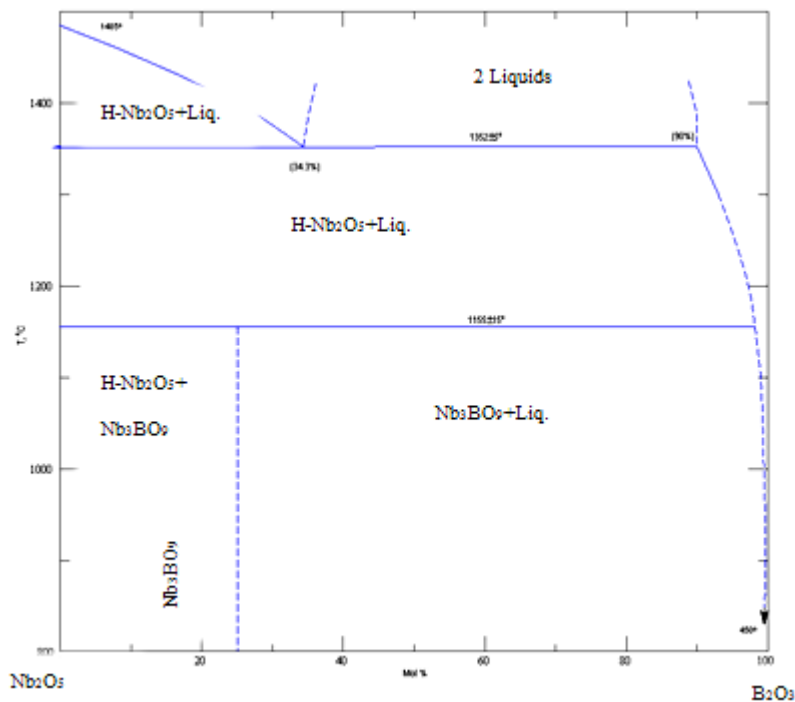

Figure 4.12 Binary Nb_2O_5-B_2O_3 oxides phase diagram (Levin, 1966)
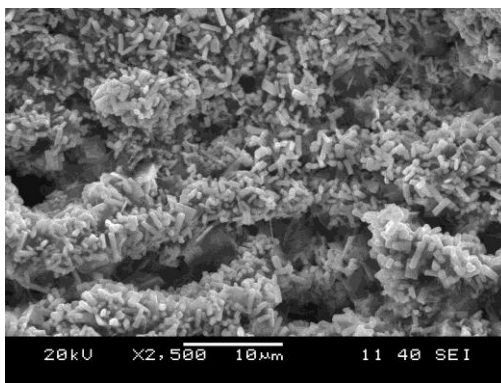
Figure 4.13 Surface SE micrograph of 950°C/5h
boronized Nb plates after oxidation at 1000°C
for 30 min.

In Figure 4.14, cross-sectional SE micrographs of the "as-received" Nb sample and the 950°C/8h boronized Nb slug after oxidation at 1000°C for 30 min. are shown. An oxide layer with a thickness of about 300 µm formed on the "as-received" Nb

slug. In this oxide layer some cracks and pores were present. Compared to the "as-received" sample, a thin (~50 µm) oxide layer formed on the boronized Nb slug. It is thought that, oxide layer was broken down during sample preparation.

(a)   (b)
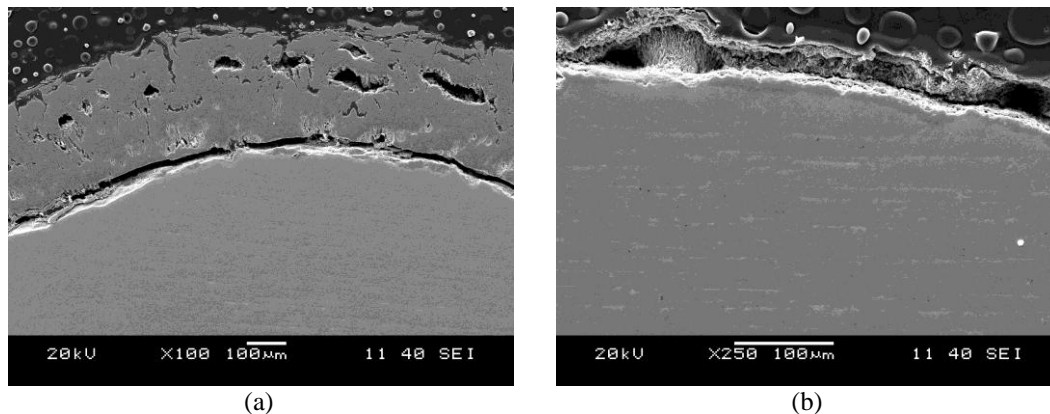
Figure 4.14 Cross-sectional SE micrograph of (a) as-received Nb and (b) 950°C/8h boronized Nb slugs after oxidation at 1000°C for 30 min.

In Figure 4.15, weight changes of both the as-received and boronized Mo as well as Nb slug samples are shown. It is clear that Mo samples lost considerable mass upon oxidation. However, the boronized Mo lost less weight than the as-received Mo sample. However, losses for the Nb sample were much smaller. Furthermore, the boronized Nb had a weight gain which indicted that boronizing had a positive effect on oxidation resistance of Nb metal.
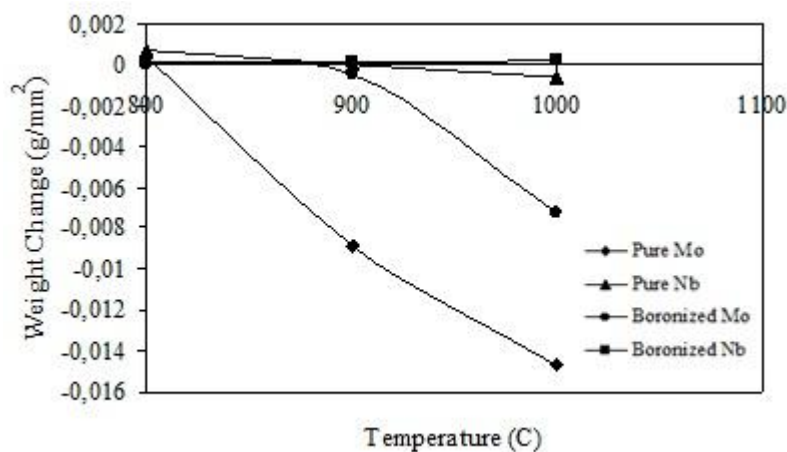
Figure 4.15 Weight changes of as-received and boronized Mo and Nb samples after oxidation at 800, 900, 1000°C for 30 min. in air.

4.2 Results and Discussion for Nb-Containing Binary Alloys

4.2.1 Production and Characterization of Nb-Containing Binary Alloys

4.2.1.1 Production and Characterization of Niobium-Chromium Binary Alloys

In the previous chapter, oxidation behavior of pure Mo and Nb metals were discussed. It is clear that, at moderately elevated temperatures (~850°C) in oxygen-containing environments like air, oxidation of these refractory metals produces non-protective oxides. Because of the high volatility of its oxide, molybdenum has a lower oxidation resistance than niobium. However, niobium has a lower density and higher low-temperature ductility compared to Mo (Buckman, 1988). Thus, these properties make niobium a more preferable base-metal for the development of   high-temperature structural alloys.

Stringer and others (1975) reviewed earlier studies conducted on Nb metal and some of its alloys. They noted that studies had been generally focused on the use of alloying additions to Nb in order to modify the products of Nb oxidation. There, it was expected that such modification would be able to reduce the oxidation rate of the Nb alloys. Oxidation studies showed that the oxide phase observed upon air oxidation of Nb was generally Nb_2O_5 which is not protective and resistant against alteration of its structure by doping with other elements. Nevertheless, to improve the high temperature oxidation resistance of Nb metal, alloying elements such as Al, Si, or Cr had been added to this metal (Geng, Tsakiropoulos, & Shao, 2006). Because oxides of Al and Si are thermodynamically more stable than those of Nb, they were used as alloying elements for Nb. Although elements like Al is also added to steels and nickel alloys such as superalloys to improve their high temperature oxidizing resistances, it was noted that adding Al to Nb decreased the melting point of the alloy thus negating the effect of the refractory nature of the Nb metal. Recently, the attention on Nb-based materials focused on the addition of Si to form intermetallic phases like silicides in the alloy microstructure. However, intermetallics can also form by the addition of Cr to Nb because the Nb-Cr binary system contains such a

phase; Cr_2Nb which is also known as a Laves phase (Brady et al., 2000; Walker; Chu et al., 1998; Keitz, Sautdoff, 2002) as shown in Figure 2.6 (c). In this thesis work, some experimental Nb-Cr binary alloys were produced and their oxidation behavior was investigated.

Chromium is a refractory metal group element like Nb and its melting point is $1857^{o}C$. According to the Nb-Cr binary phase diagram in Figure 2.6 (c), if more than 10 w/o Cr is added to Nb, the Laves phase; Cr_2Nb becomes stable in the structure. Thus, a multiphase microstructure containing Laves phase and Nb solid solution forms yielding an *in-situ* composite material. According to the studies in the literature, Laves phases can provide the alloy high-temperature strength and oxidation resistance while the ductile Nb solid solution phase (Nbss) provides ductility and fracture toughness at ambient temperatures (Takeyama, & Liu, 1991; Yoshida, & Takasugi, 1999; Zheng, Lu, & Huang, 2009).

In this study, Nb-xCr alloys (x =10, 20, 30, 33 w/o) belonging to the Nb-rich Nb-Cr_2Nb pseudo-binary system were produced and oxidized at high temperature in air. Considering their thermodynamic stabilities, it is expected that oxides of Nb metal (NbO, NbO_2 and Nb_2O_5) and of Cr (Cr_2O_3) will form upon oxidation of these binary alloys. In some cases, spinel-type chromate phases can also become stable. Although thermodynamic stability of the Cr_2O_3 phase is higher than those of Nb_2O_5 and NbO_2 at all temperatures, it was reported in the literature that scales containing only Cr_2O_3 was observed upon oxidation, at $900^{o}C$, on the Cr- 27a/o Nb alloy which is in the Cr-rich, Cr-Cr_2Nb pseudo-binary region of the phase diagram (Tortorelli, & Pint, 1996).

The binary Nb-Cr alloys produced in this study by VAM is shown in Table 4.1. Two different types of raw materials; bulk (slugs) or powders of the constituent metals were used for alloy production. The intended (theoretical) compositions, production parameters and some properties such as 'presence of unmelted material' and 'brittleness' of the as-cast ingots after casting are shown in Table 4.1. The alloy designation 'NC (b)-1' in this Table, indicates that the ingot is the first Nb-Cr alloy

ingot produced by using bulk raw materials. Ingots that are prepared from metal powders have the letter ` (p) ` in their designation.

Upon sectioning of the as-cast ingots NC (b)-1, 2 and 3, unmelted Nb areas were observed in the microstructure. After the production of the first two ingots, mass losses, by vaporization, were also observed. Because the melting temperature of Nb (2468°C) is much higher than that of Cr metal (1857°C), at temperatures where Cr was molten, the Nb slugs were still intact. This difference in melting temperatures is thought to be the cause of the unmelted zones observed in this alloy.

Table 4.1 Production parameters and some properties of the binary Nb-Cr alloy ingots produced.

Alloy Name	Theoretical composition (in w/o)	Max. Electrode Current (A)	Number of melting cycles	% Weight loss	Unmelted material in the ingot	Behavior during EDM cutting and drilling
NC (b)-1	Nb-20Cr	80	5	3.0	Observed	Satisfactory
NC (b)-2	Nb-10Cr	80	5	7.3	Observed	Satisfactory
NC (b)-3	Nb-13Cr	80	5	10.3	Observed	Satisfactory
NC (b)-4*	Nb-33Cr	120	5	2.0	Not Observed	Unsatisfactory
NC (p)-5	Nb-10Cr	140	10	9.9	Not Observed	Satisfactory
NC (p)-6	Nb-20Cr	140	10	6.9	Not Observed	Satisfactory
NC (p)-7	Nb-30Cr	120	8	3.4	Not Observed	Unsatisfactory
NC (p)-8	Nb-30Cr	120	10	3.6	Not Observed	Unsatisfactory
NC (p)-9	Nb-50Cr	120	7	4.1	Not Observed	Unsatisfactory
NC (p)-10	Nb-15Cr	120	15	-	Not Observed	Satisfactory

* produced by the "stepwise" method explained in the text.

The difference between the melting temperatures of the constituent elements is believed to be responsible also for the material loss from the ingots by Cr evaporation. This is because Cr has high vapor pressures at temperatures closer to the melting point of Nb. This suggestion that mass losses were due to Cr vaporization was found to be reasonable after conducting EDS analyses on the ingots and comparing the EDS data to the theoretical compositions of the alloys. However, the amount of mass loss calculated for the ingots did not correlate well with the amount of Cr left in the alloy. For example, mass loss observed for the NC (b)-3 sample was

more than that observed for the NC (b)-1 sample even though the latter had a higher Cr content. This observation indicated the possibility that the amount of Cr losses could be related to the placement of the starting raw materials in the VAM furnace. Besides, the electrode current used during melting may have affected the amount of Cr losses from the ingot.

Based on these observations, a new set of production conditions were chosen as shown in Table 4.1. This new ingot production method was first used for the production of the NC (b)-4 alloy. This method is called the "stepwise" production because the raw materials are placed inside the water-cooled Cu mold in such a way that Cr pieces are protected from melting before the melting of the Nb slugs. Also, higher electrode currents were used in this new method in order to melt the Nb slugs faster. As seen in Table 4.1, the NC (b)-4 sample produced by this "stepwise" method did not have unmelted Nb areas in its microstructure. Furthermore, the mass loss measured for this alloy was much lower than those measured for the alloys that had higher Cr contents than the NC (b)-4 alloy.

A typical BE image of the NC (b)-3 alloy microstructure is given in Figure 4.16 (a). It showed the presence of an area with different compositions and morphologies. The niobium rich area "A" was found to contain unmelted Nb pieces. There was an intermediate region labeled "B" between the unmelted Nb piece (area "A") and the "dendritic" area "C". On the other hand, the microstructure showed in Figure 4.16 (b) was taken from the NC (b)-4 sample produced by the stepwise method by which the formation of areas was eliminated. Thus, the alloy had a relatively uniform microstructure.

In Figure 4.17 (a), (b), typical microstructural SEM/BE images of the Nb20Cr (w/o) binary alloy NC (b)-1 is shown. The alloy had a multiphase microstructure. The blocky areas (labeled "A") contain the primary Nbss phase as suggested by its bright appearance in the BE images. The high magnification micrograph in Figure 4.17 (b) shows that these blocky areas are surrounded by smaller bright particles and a darker matrix. The matrix contains the $NbCr_2$ (Laves) phase which is one of the

products of the eutectic reaction indicated in the Nb-Cr phase diagram. The other product of the eutectic reaction was the smaller bright particles containing the Nbss phase. According to the EDS results conducted on different regions of the alloy microstructure in Figure 4.17, area "A" has 90.1% Nb and area "B" has 69.0% Nb. As expected, the primary Nbss areas (labeled "A") are rich in Nb. Since both Nbss and NbCr$_2$ phases are present in area "B", Cr concentration was higher in this region.

(a)   (b)
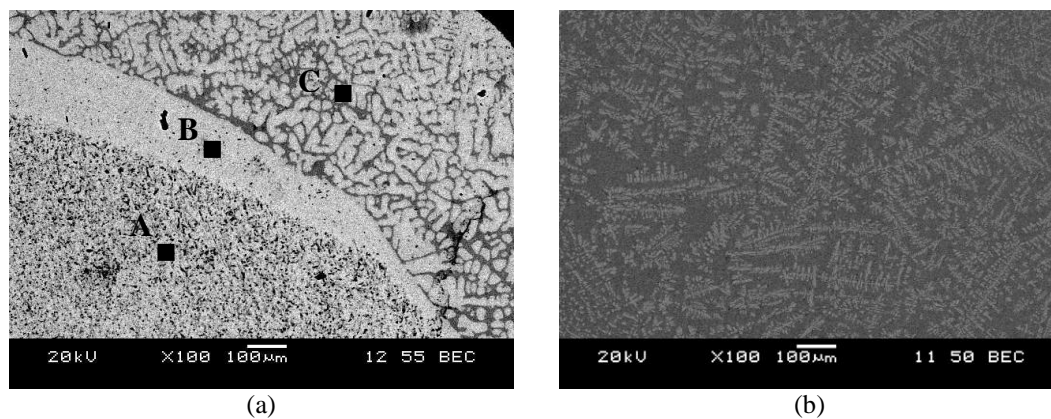
Figure 4.16 Micrographs showing (a) unmelted Nb pieces in NC (b)-3 and (b) microstructure of NC (b)-4 alloy produced by the 'stepwise' method.

(a)   (b)
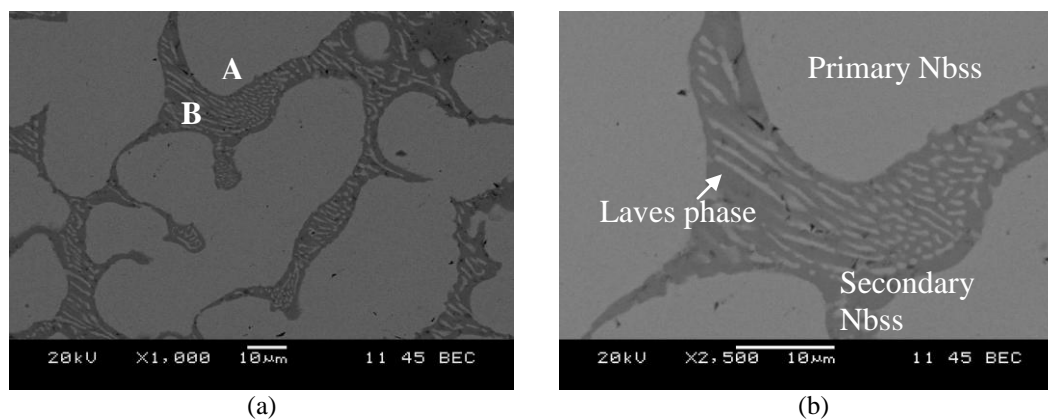
Figure 4.17 Micrographs showing the microstructure of the NC (b)-1 alloy.

Figure 4.18 shows the changes that took place in the microstructure of the NC (b)-4 alloy upon annealing. The large and interconnected primary Nbss phases broke into smaller pieces after 29 hours at 1000°C. At the same time, the amount of the primary Nbss phase decreased while the amount of the eutectic areas increased. These observations indicated that the as-cast samples prepared by using bulk raw

materials may need heat treatment in order to develop the equilibrium microstructures expected from the Nb-Cr binary phase diagram.

(a)   (b)
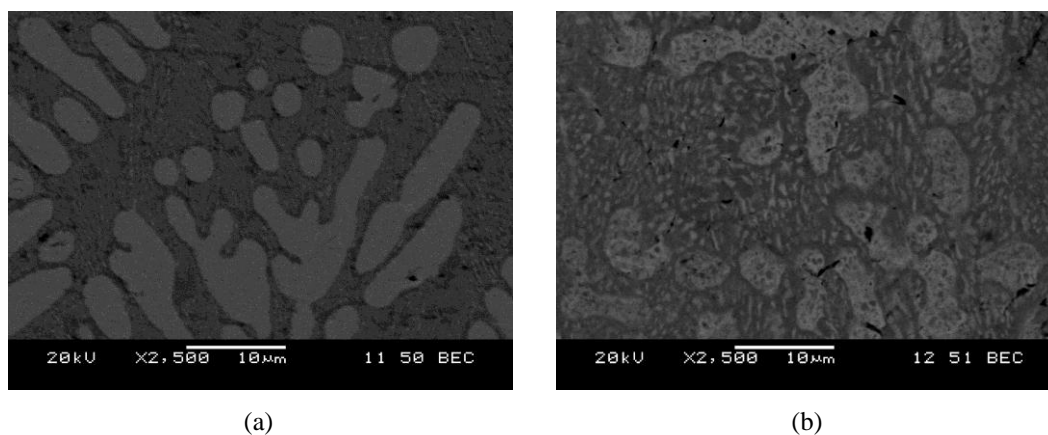
Figure 4.18 SEM/BE images of the NC (b)-4 alloy microstructure (a) before and (b) after annealing in quartz capsule.

Although the 'stepwise' method was able to prevent the presence of unmelted material in the ingots, it was later found out that using metal powders for alloy production was a better approach to produce ingots with higher homogeneity. As seen in Table 4.1, ingots based on powder raw materials did not have unmelted zones. Although mass losses were still observed for these ingots, losses were mainly due to the higher electrode currents and number of melting cycles used during their production. These parameters are later optimized so that alloy ingots without unmelted particles can be produced by melting metal powders using about 120 A electrode current during 5 consecutive melting cycles.

The NC (p)-5 alloy was the first ingot produced from metal powders. Initially, two disc-shaped powder compacts of this alloy each weighing 2.5 gr with a thickness of about 1.5 mm were prepared. Then, these discs were melted together to obtain an ingot of about 5 gr. However the amount of vaporization during the melting of two discs was high. Thus, a thicker single disc (max 3 mm) of the alloy was prepared. An electrode current of 140 A was used for melting of the NC (p)-5 alloy. It was observed that the alloy had a single phase (Nbss) structure. This result was expected because of the low Cr content of this alloy. It should be mentioned that unmelted Nb

areas were not observed in this alloy unlike the NC (b)-2 alloy which had a similar composition but produced by using bulk materials.

(a)

(b)

(c)

(d)

(e)

Figure 4.19 BE images of as-cast (a,b) NC (p)-6, (c,d) NC (p)-7 and (e) HT-NC (p)-7 alloys.

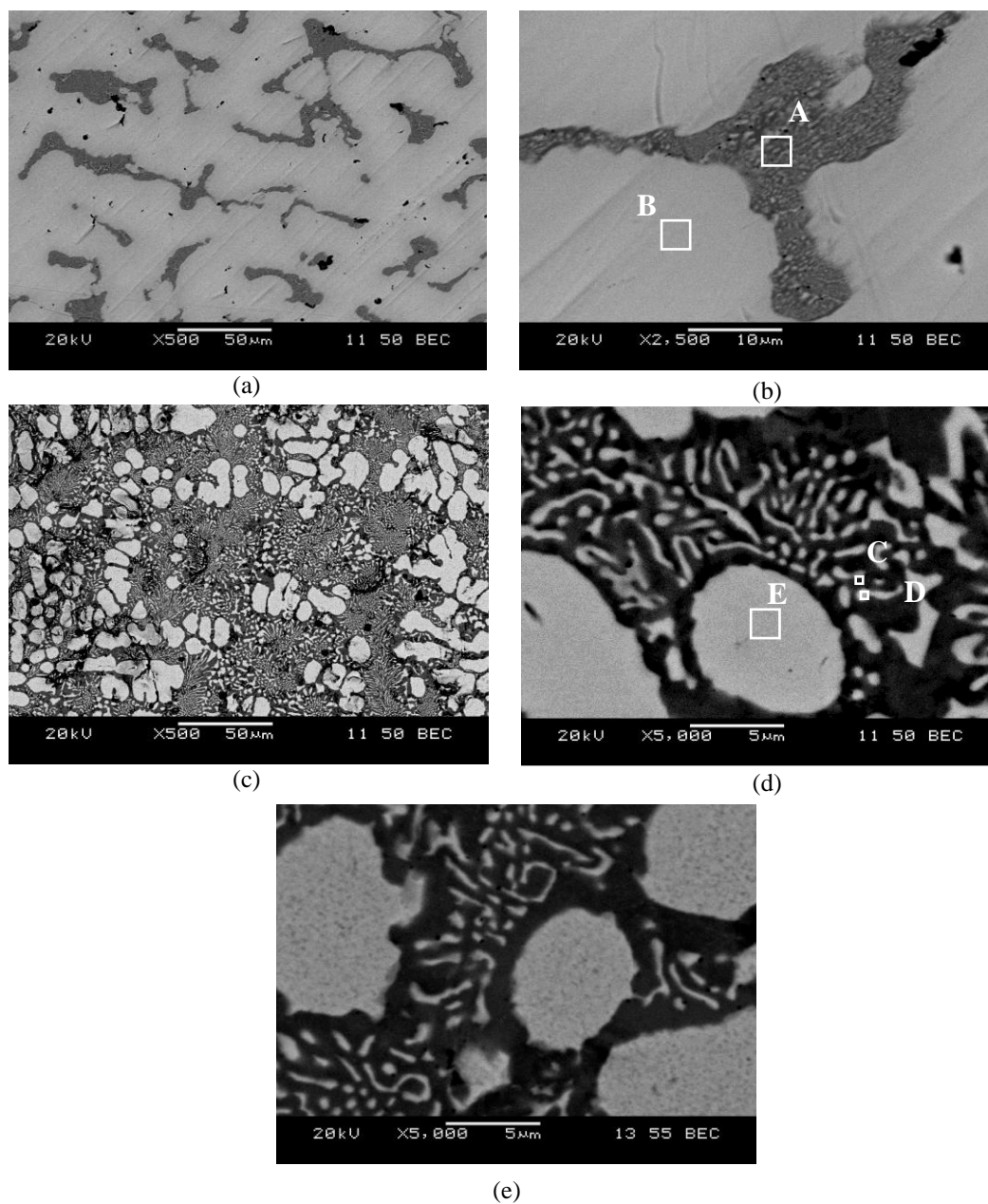The powder-based alloys; NC (p)-6 and NC (p)-7 had multiphase structures as expected from their Cr contents. Typical microstructures of these alloys are shown in the SEM/BE pictures of Figure 4.19. Both primary and secondary Nbss phases (bright areas) were present in these alloys as suggested by the Nb-Cr phase diagram.

Furthermore, the amount of the eutectic regions (darker areas) was lower and the amount of primary Nbss regions was higher in the NC (p)-6 alloy because of its lower Cr content. These results indicated that ingots prepared by the powder method had better homogeneity even in the as-cast condition.

Table 4.2 EDS analyses results (in w/o) for areas A-E in Figure 4.19.

	A	B	C	D	E
Nb	71.2	93.0	82.1	71.3	90.2
Cr	28.8	7.0	17.9	28.7	9.8

Results of the EDS analyses conducted on the areas labeled A through E in the NC (p)-6 and NC (p)-7 alloys are shown in Table 4.2. It is clear that areas B and E correspond to the primary Nbss phase whereas areas A, D and C correspond to regions where the Cr-containing $NbCr_2$ phase has formed. It should be noted that these microstructures developed in the alloys during their cooling in the VAM. Based on the fine eutectic structure (Figure 4.19 (c), (d)) of the NC (p)-7 sample and the observation of the expected phase structure, it can be said that the powder-based ingots had near-equilibrium microstructures even in the as-cast conditions. This must be related to the higher homogeneity of the alloys prepared by the powder method. BE image of NC (p)-7 after $1000^{o}C$ annealing for 44 hours is given in Figure 4.19 (e). Significant differences between the microstructure of the as-cast and the heat treated NC (p)-7 samples were not present.

In Figure 4.20, results of the XRD analyses conducted on some of the slug-based and powder-based alloys are shown. In accordance with the microstructural changes shown in Figure 4.18, during heat treatment of the NC (b)-4 alloy, the amount of the Cr_2Nb phase increased as suggested by the Nb-Cr phase diagram. Diffraction peaks belonging to this phase were clearly visible for the heat treated sample. Furthermore, XRD results of the heat treated NC (b)-4 alloy and the NC (p)-7 samples were similar even though the former alloy was produced from slugs whereas the latter alloy produced by the powder method. Therefore, these observations showed again that the powder-based ingots had near-equilibrium microstructures even in the

as-cast condition. XRD results of the similarly prepared (NC (p)-7 and NC (p)-8) alloys indicated that multiple melting of the powder-based ingots during production further increased their homogeneity.
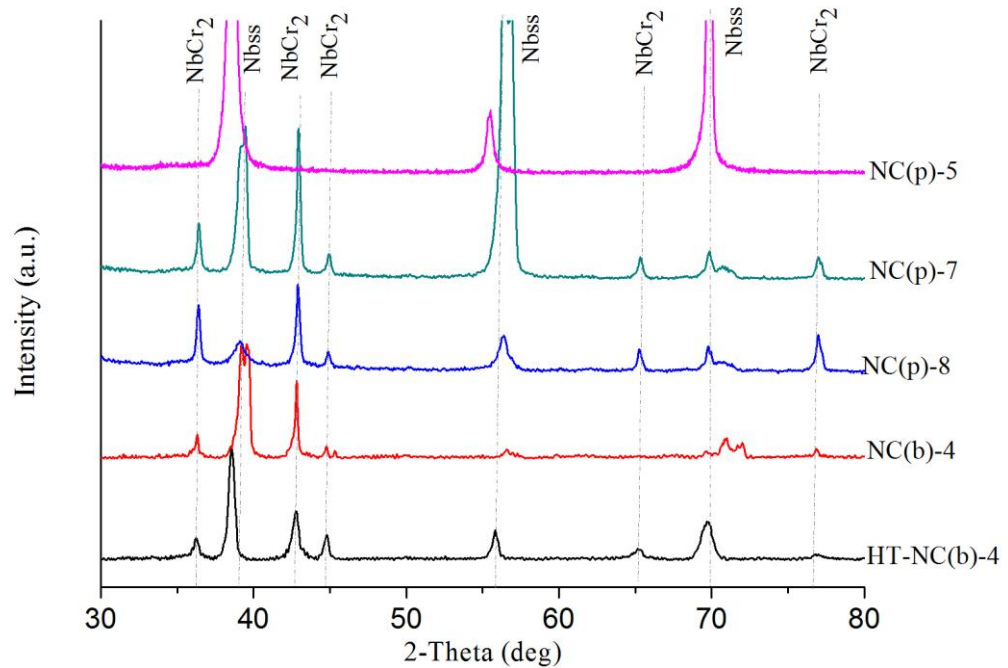
Figure 4.20 XRD results for some bulk or powder-based alloys. HT: heat-treated

4.2.1.2 Production and Characterization of Niobium-Molybdenum Binary Alloys

Another alloying element added to pure Nb was Molybdenum (Mo). This element was chosen because its melting point is close to that of Nb and that the binary alloy system is isomorphous (Figure 2.6 (a)). It is mentioned in the literature that alloying of Nb by Mo causes increases in the tensile strength, stress-rupture strength and low-temperature plasticity of Nb alloys as a result of solid solution strengthening.

Properties of the binary Mo-Nb alloys produced in this study by VAM are shown in Table 4.3. For their production, first bulk raw materials were used. The initial ingots produced were slightly Mo-rich. As seen in the SEM/BE image of Figure 4.21, the Mo-rich alloy contained areas at which only Mo was detected by EDS suggesting that Mo slugs did not completely melt during alloy production. After sectioning of

the as-cast NM (b)-1 and (b)-2 alloy ingots, presence of unmelted Mo was verified. Consequently, metal powders were used later to produce Nb-Mo alloys. As noted in Table 4.3, these new ingots had better homogeneities clearly indicating that powder-based production yielded ingots with better microstructures.

Table 4.3 Production parameters and some properties of the binary Nb-Mo ingots produced.

Alloy Name	Theoretical composition (in w/o)	Max. Electrode Current (A)	Number of melting cycles	% Weight loss	Unmelted material in the ingot	Behavior during EDM cutting and drilling
NM (b)-1	Mo-46Nb	100	2	0.1	Observed	Unsatisfactory
NM (b)-2	Mo-46Nb	120	5	1.0	Observed	Unsatisfactory
NM (p)-3	Nb-70Mo	150	15	1.4	Not Observed	Satisfactory
NM (p)-4	Nb-50Mo	150	10	2.3	Not Observed	Satisfactory
NM (p)-5	Nb-30Mo	150	15	1.1	Not Observed	Satisfactory

(a)   (b)
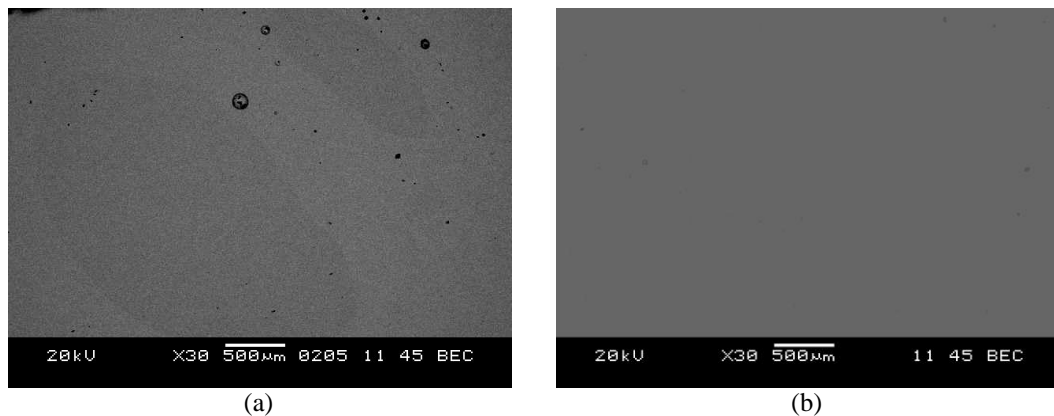
Figure 4.21 BE images of NM (b)-1 and NM (p)-5 alloy samples.

In Figure 4.22, XRD analyses results of the as-cast alloy samples are shown. According to these results, only the Nb-Mo solid solution phase was present in these alloys as expected from the isomorphous Nb-Mo phase diagram. Furthermore, XRD peaks were observed to shift toward smaller diffraction angles as the Mo content of the alloy decreased. Since lattice parameters of Mo and Nb are 3.15 and 3.30 A, respectively, as the % Mo decreases, the Nb-rich lattice would expand to increase the distances (d) between the diffracting planes. According to the Bragg's law, as the interplanar distances increase diffraction angles should decrease.
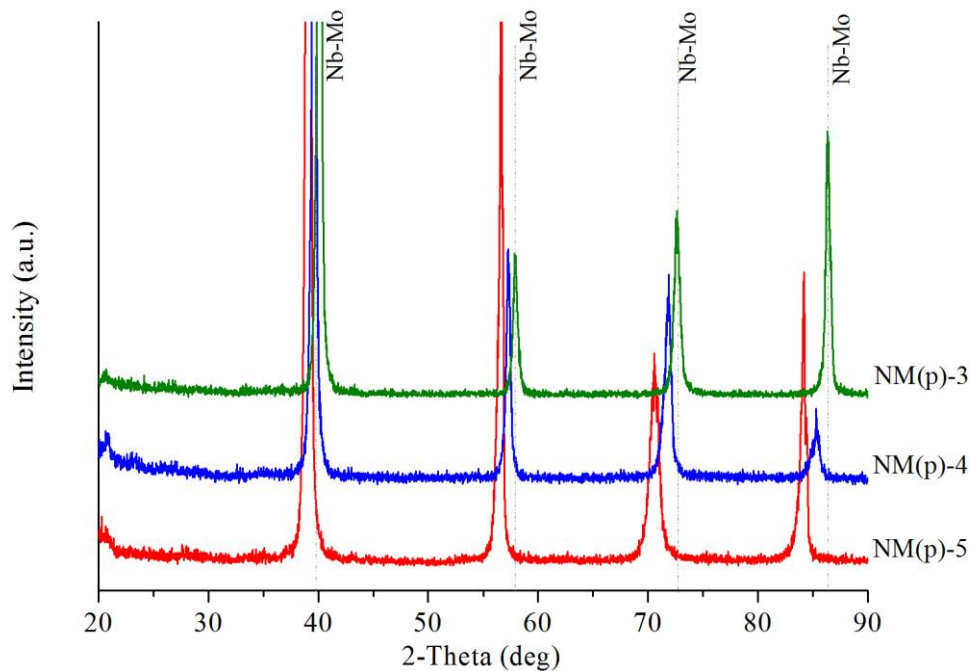
Figure 4.22 XRD diffraction patterns of the as-cast Nb-Mo binary alloys.

During this Thesis work, Electron Beam Melter (EBM) equipment available in the Process Metallurgy and Metal Recycling Laboratories (IME) at RWTH, Aachen, Germany was used to produce alloys with better microstructures and in quantities enough to make samples for high temperature corrosion studies. The EBM technique is also used for alloy production at high temperatures and low oxygen partial pressures as is the case with the VAM process. However besides some advantages, the EBM technique was found to have drawbacks.

The data in Table 4.4 show that the beam currents required for alloy production in the EBM system are closely related to the theoretical composition of the desired alloy. For example, production of Ti-Cr binary alloy ingots (EBM 3-4) required lower beam currents than that required for Nb-Mo ingots (EBM 1-2). This was due to the differences between the melting temperatures of the metals making up the alloys. A similar behavior was also observed, as mentioned above, especially during the production of Mo-containing alloys by the VAM method. It was also observed that material loss from the alloys were larger during the EB melting. This behavior is believed to be related mainly to the high vacuum environment in the EB equipment.

Table 4.4 Electron beam current of the furnace, theoretical compositions and weight changes of the alloy ingots.

Sample No	Pure Metals	Theoretical Composition (in w/o)	~Max. Current (mA) *	Weight Before Melting (g)	Weight Change (%)
EBM 1	Nb	49.92	300-350	40.10	-2.5
	Mo	50.08			
EBM 2	Nb	25.37	300-500	40.40	-2.0
	Mo	74.63			
EBM 3	Ti	78.12	130-150	23.07	-0.9
	Cr	21.88			
EBM 4	Ti	89.23	150-130	23.51	-2.8
	Cr	10.77			

*1st and 2nd numbers are the beam currents for the first and second melting cycles, respectively.

The effect of vacuum on material loss during alloy production can be explained by considering Figure 4.23 which shows the changes in vapor pressures of the elements with temperature. It is observed that, at a given temperature, elements which have lower melting temperatures have higher vapor pressures. Since elements like Nb, Cr, Ti with different melting temperatures of 2468°C, 1857°C and 1670°C, respectively are used in the tests, losses of these elements by evaporation during the preparation of the alloys depended on the processing temperature.

Material losses by evaporation were enhanced as the differences between the melting temperatures of the alloying elements increase (Ulf, Larsson, & Harrysson, 2003). Unfortunately, this condition is always present during the production of the refractory metal-based alloys. To overcome this problem, the melting process must either be kept short or an excess amount of the low melting temperature elements is added to the starting batch of raw materials.

Nevertheless, some alloy samples larger than those produced by the VAM method were manufactured at IME by the EBM method. Test samples from these larger ingots were machined in our laboratory.
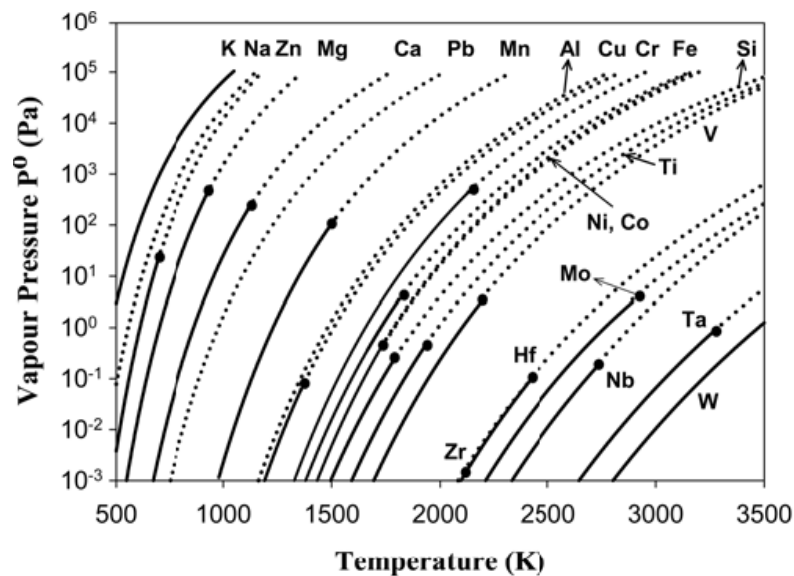
Figure 4.23 Vapor pressure vs. temperature (K) curve for some elements (Choi, Lim, Munirathnam, & Kim, 2009).

4.2.2 Boronizing of Some Selected Nb-based Binary Alloys

4.2.2.1 Boronizing of Some Niobium-Chromium (NC) Binary Alloys

A boronizing test was conducted on a sample of NC (p)-7 alloy (30% Cr) at 950°C for 5h. SEM/BE investigation of the sample cross-section after boronizing did not indicate clearly the formation of a boride layer (Figure 4.24 (a)). This observation suggested that it may not be easy to boronize alloys containing large amounts of NbCr$_2$ phase. Then, another Nb alloy; NC (p)-10 containing 15% Cr was produced and two samples of this alloy were pack-boronized at 950°C for 8 hours. Cross-section of this lower-Cr alloy after boronizing is shown in Figure 4.24 (b). Formation of a diffusion layer over this alloy is clearly observed. Also, XRD analysis of this sample's outer surface indicated the presence of the NbB$_2$ phase (Figure 4.25). Observation of diffraction peaks also from the Nbss phase in the alloy suggested that the boride layer formed over the low-Cr alloy was not thick.

In order to understand the effect of the alloy's Cr content on its boronizing behavior, an analysis of the thermodynamic stabilities of the phases that can form in the alloy is conducted as follows.

(a)   (b)
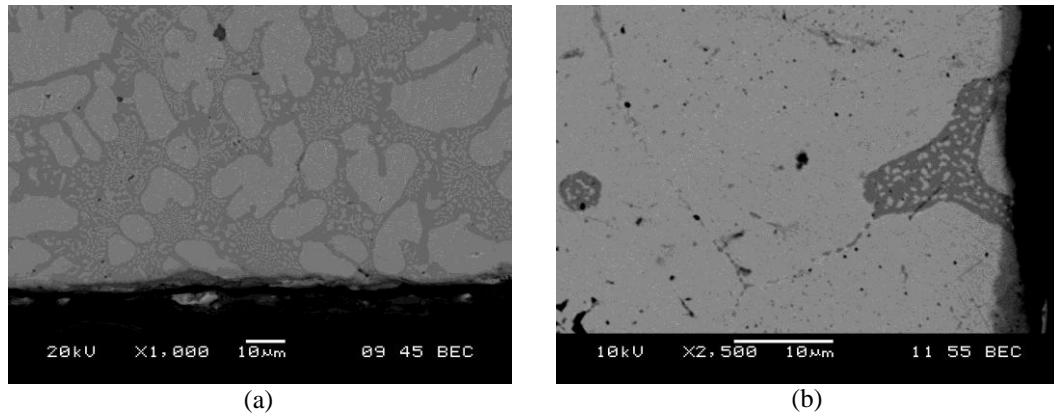
Figure 4.24 SEM/BE cross-sectional micrographs of the (a) NC (p)-7 boronized at 950°C for 5h, and (b) NC (p)-10 binary alloys boronized at 950°C for 8h.
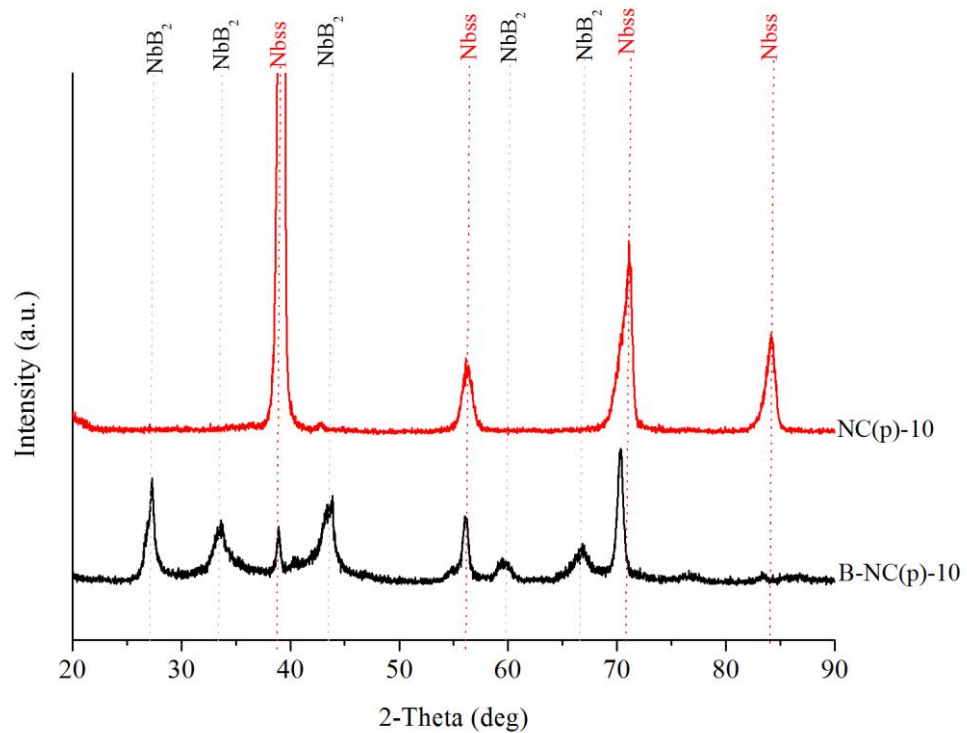
Figure 4.25 XRD diffraction pattern of the unboronized and boronized NC (p)-10 alloy.

As boron atoms diffuse into the Nb-Cr alloy, they chemically interact with the base and alloying elements in the alloy. The possible reactions which can take place in the alloy and their standard Gibbs free energy changes (ΔG^{o}_{1223}) calculated for the boronizing temperature (1223 K) are given in Table 4.5.

Table 4.5 Standard free energies of the reactions related to boronizing of Nb-base alloys (Kubaschewski, & Alcock, 1979; Türkdoğan, 1980).

|	Reactions	ΔG^o_{1223} (J/mole)
1	$\langle Nb \rangle + 2\langle B \rangle = \langle NbB_2 \rangle$	-291796
2	$\langle Cr \rangle + \langle B \rangle = \langle CrB \rangle$	-65724
3	$\langle NbCr_2 \rangle + 2\langle B \rangle = \langle NbB_2 \rangle + 2\langle Cr \rangle$	-269835
4	$\langle NbCr_2 \rangle + 2\langle B \rangle = 2\langle CrB \rangle + \langle Nb \rangle$	-43763
5	$\langle NbCr_2 \rangle + 4\langle B \rangle = \langle NbB_2 \rangle + 2\langle CrB \rangle$	-401283
6	$\langle Mo \rangle + \langle B \rangle = \langle MoB \rangle$	-2476
7	$\langle MoB \rangle + \langle Nb \rangle = \langle NbB_2 \rangle + \langle Mo \rangle$	-286645

In the case of the NC (p)-5 Nb-Cr alloy containing about 10% Cr, only Nbss phase with dissolved Cr is stable as shown in Figure 4.20. During boronizing, B atoms can react with both Nb and Cr atoms through reactions 1 and 2 in Table 4.5. However, as the XRD data in Figure 4.25 show, only the NbB_2 phase formed during boronizing of the NC (p)-10 alloy even though this alloy had a Cr content of 15%. Thus, formation of the CrB by reaction 2 did not take place. This result is consistent with the relatively higher Gibbs free energy of formation of the NbB_2 phase compared to that of the CrB phase. This CrB phase, however, was shown to be stable in the case of the boronizing of pure Cr (Usta et al., 2006).

Nb-Cr alloys with higher Cr content such as NC (p)-7 alloy (30% Cr) has $NbCr_2$ intermetallic phase besides the Nbss phase in its microstructure (Figure 4.20). According to the Gibbs free energy changes of reactions 3 and 4 in Table 4.5, if this intermetallic phase dissociates during boronizing, the NbB_2 phase could form since it has a higher stability. Cr metal which is the product of such a dissociation reaction may then react with B to form CrB phase according to reaction 5. However, XRD analysis of the boronizing high-Cr containing NC (p)-7 alloy did not indicate the formation of the CrB phase after test. This could again be due to the higher stability of the NbB_2 phase as well as the slow dissociation rate of the intermetallic $NbCr_2$ phase.

4.2.2.2 Boronizing of Some Niobium-Molybdenum (NM) Binary Alloys

Boronizing tests were conducted on the niobium-molybdenum alloys produced from powder raw materials (Table 4.3). BE images of the cross-sections of the NM (p)-3, NM (p)-4, and NM (p)-5 alloys boronized at 950°C for 8h are shown in Figure 4.26 (a)-(c). Although thicknesses of the boride layers formed were not uniform, their average values were measured to be about 2.50 μm, 1 μm and 2.00 μm for the (p)-3, 4, and 5 alloys, respectively. Compared to the thicknesses of boride layers formed over the pure Mo and Nb metals, boride layer thicknesses formed on these Nb-Mo alloys were lower. Furthermore, according to the XRD results shown in Figure 4.27, almost all the diffraction peaks detected belonged to the MoB phase regardless of the alloy composition. This observation was not expected since the Gibbs free energy of formation of MoB is less than that of NbB_2 even though they are both negative. This result may be related to the kinetics of the boronizing reaction. According to the reactions in Table 4.5, formation of MoB requires a single B atom for every Mo atom whereas two B atoms are needed for the formation of NbB_2. Since B atoms diffuse into the alloy substrate from the surface, MoB phase could have nucleated earlier than the NbB_2 phase at least in the areas closer to the sample surface. Furthermore, other studies reported that diffusion rate of B in Mo ($63.8x10^{-19}$ m/s^2), is higher than that in Nb ($27.6x10^{-22}$ m/s^2) at the boronizing temperature of 950°C (1223 K).

4.2.3 Oxidation of As-cast and Boronized Nb-Containing Binary Alloys

In this section, results of the oxidation tests conducted on the Nb-Cr and Nb-Mo alloys are discussed. Before the oxidation tests, all surfaces of the as-cast alloy samples were polished and cleaned with acetone, ultrasonically, as explained in Chapter 3. Oxidation tests were conducted at 800°C, 900°C and 1000°C for 30 min. in static air. Some oxidation tests were also conducted on some alloy samples at temperatures lower than 800°C.
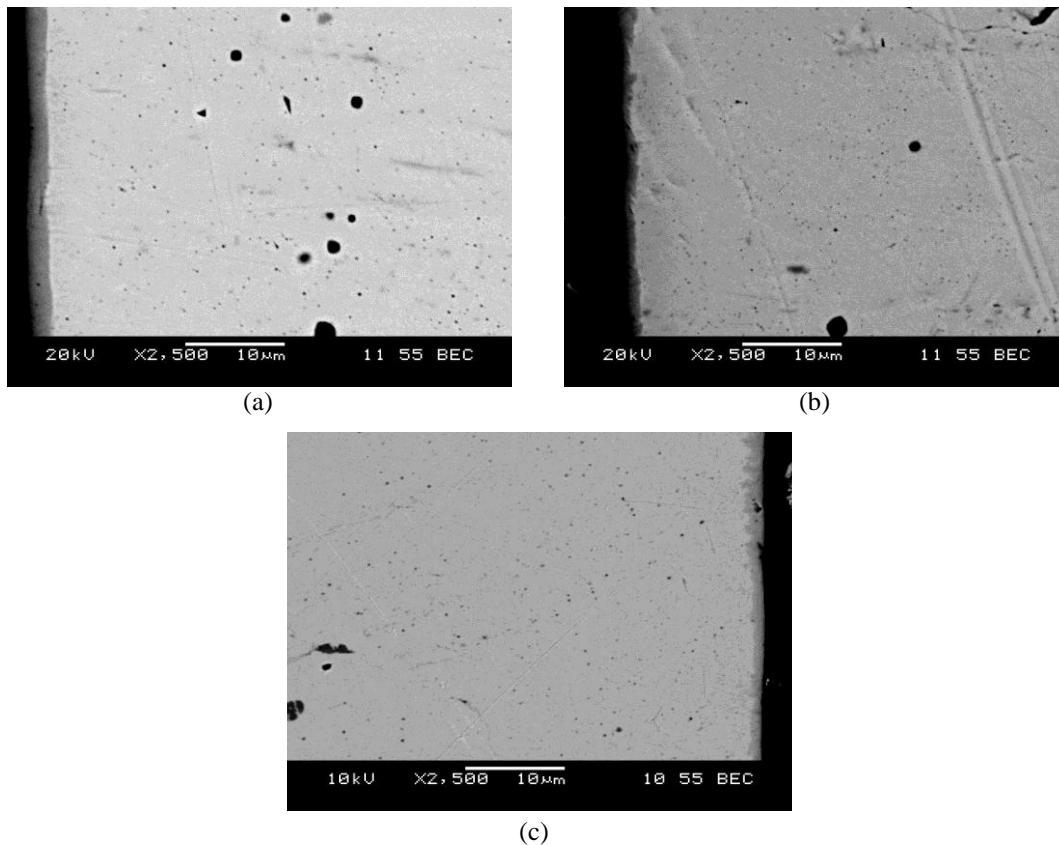
Figure 4.26 SEM/BE cross-sectional micrographs of the as-cast (a) NM (p)-3, (b) NM (p)-4, and (c) NM (p)-5 binary alloys boronized at 950°C for 8h.
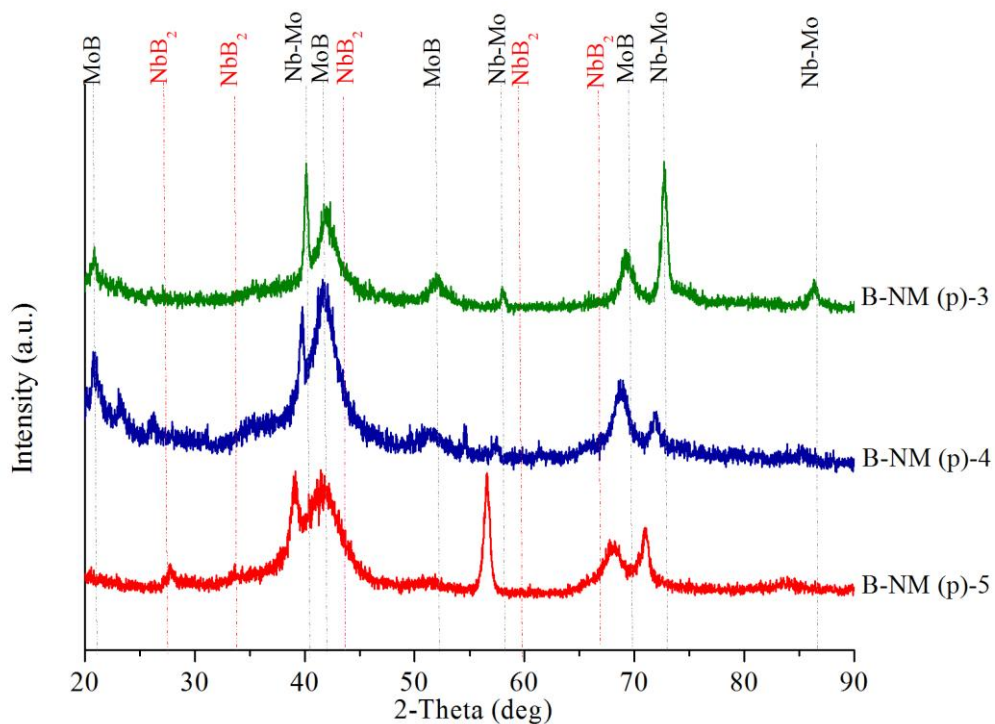

Figure 4.27 XRD diffraction pattern of the Nb-Mo binary alloys boronized at 950°C for 8h.

Boronized Nb-Cr and Nb-Mo alloys were prepared and oxidized under the same condition as the as-cast samples. In the following text, the boronized and then oxidized samples have the prefix 'B' in their names.

4.2.3.1 Oxidation of Niobium-Chromium Binary Alloys

Oxidation tests conducted on the Nb-Cr alloys started with the NC (b)-1 alloy first at 300°C to observe its low temperature oxidation behavior. After the 300°C/30 min. test, no change was observed in the surface color of this sample but its surface color changed to brown after the 500°C/30 min. test. However, the unmelted areas in this bulk-based alloy had white surface color due to the formation of only Nb oxides. Surface morphology of the sample after the 800°C/30 min. test is shown in Figure 4.28. In the BE image of the surface (Figure 4.28 (b)), bright areas indicate enrichment of the heavier alloying element; niobium. Accordingly, EDS analysis of the dark area labeled as 'A' has 27.9% Nb, 31.2% Cr and 40.9% O; whereas bright areas labeled as 'B' have 71.4% Nb, 6.7% Cr and 21.9% O. This data suggested the formation of a Cr-rich oxide scale in the area "A".

| (a) | (b) |
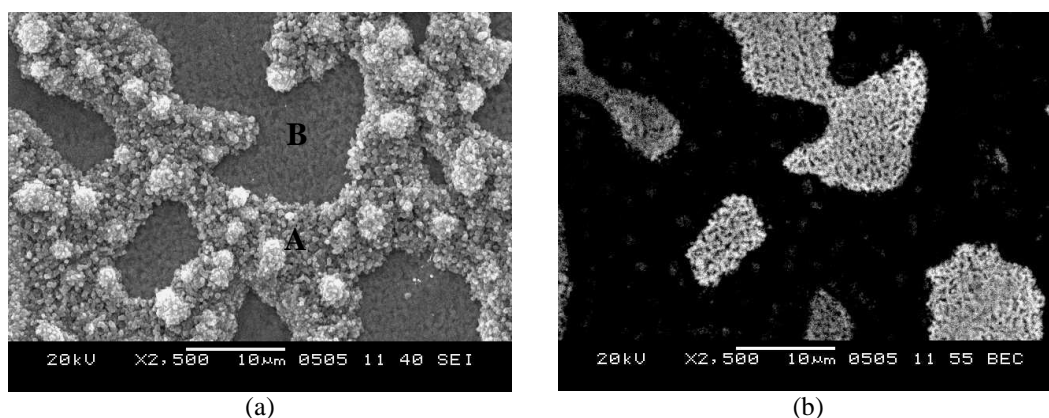
Figure 4.28 (a) SE and (b) BE micrographs of oxidized NC (b)-1 alloy sample after oxidation at 800°C for 30 min.

Cross-sectional BE images of this 20% Cr-containing alloy showed that large Nbss areas were present in the sample (bright areas in Figure 4.29 (a)). The long and dark areas on the other hand contained also the intermetallic $NbCr_2$ phase which is the other stable phase in this alloy. Over the Nbss areas, formation of a thick and layered oxidation product rich in Nb are observed. The low magnification BE image

in Figure 4.29 (b) indicated that this thick and layered oxidation products were discontinued at locations where the $NbCr_2$-containing areas intersect the outer surface. At such locations, formation of Cr-containing oxidation products was also present. EDS analyses of these areas are given in Table 4.6. Both the surface oxide structure seen in Figure 4.28 and the internal structure observed in Figure 4.29 confirmed that the oxide structure formed at the alloy surface reflected the underlying internal structure of the alloy sample. In Figure 4.30, oxidized surface of the powder-based 20% Cr-containing NC (p)-6 alloy is shown. Because of its more homogenous internal structure, the oxide scale grown on of this alloy was more homogenous than the scale in Figure 4.28 (a). EDS data in Table 4.7 shows that Cr-containing oxide regions developed on this alloy.

(a)   (b)
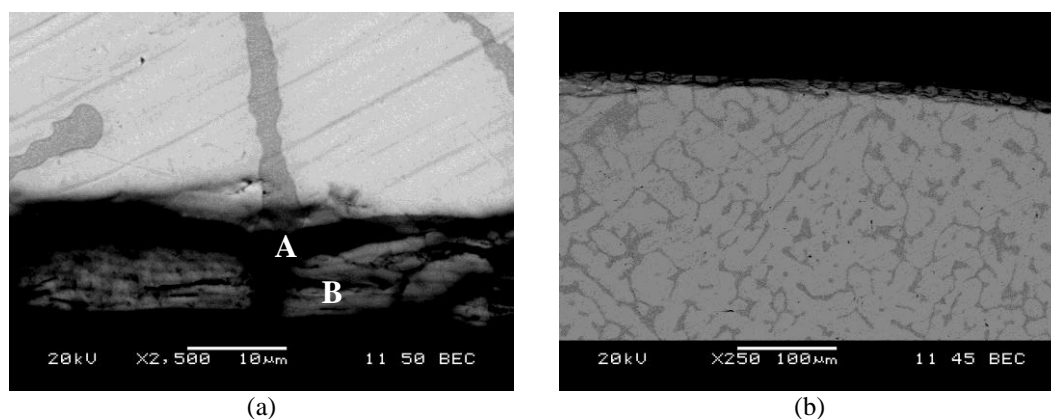
Figure 4.29 Cross-sectional BE micrographs of the 800°C for 30 min. oxidized NC (b)-1 alloy.

Table 4.6 EDS analyses results (in w/o) of dark and bright region in Figure 4.29 (a).

	A	B
Nb	76.4	87.9
Cr	14.9	6.7
O	8.7	5.4

As for the alloys in the "as-cast" and "boronized" condition, oxidation tests were conducted for the NC (p)-10 alloy (15% Cr). Surface color of this alloy was dark gray after 800°C/30 min. oxidation both in the as-cast and the boronized condition. Surface color of the as-cast alloy did not change after 900°C/30 min. and 1000°C/30 min. tests. However, the surface of the boronized alloy sample changed from dark gray to brown after the 1000°C/30 min. test. After this final test, scale spallation from both samples was observed.
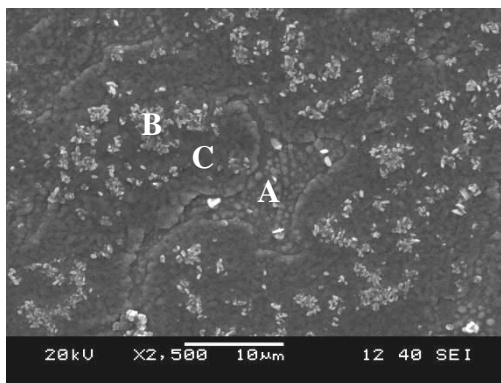
Figure 4.30 SE images of oxidized NC (p)-6
alloy after oxidation at 800°C for 30 min.

Table 4.7 EDS data (in w/o) for the oxide on the NC (p)-6 alloy after 800°C for 30 min.

	A	B	C
Nb	65.5	69.1	6.9
Cr	24.2	11.8	81.3
O	10.3	19.1	11.9
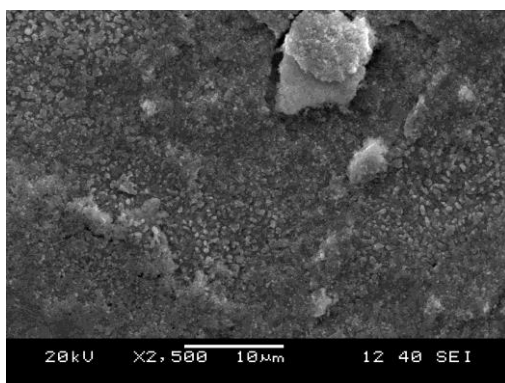
(a)
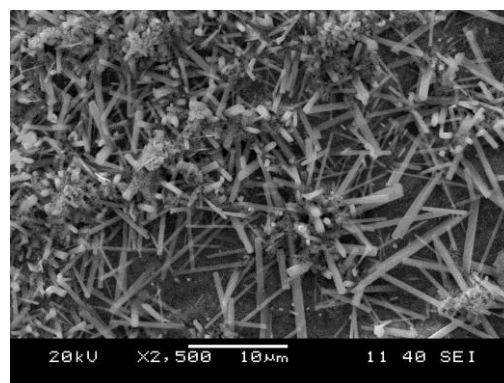
(b)
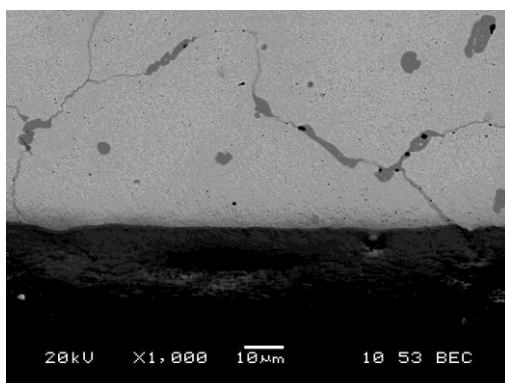
(c)
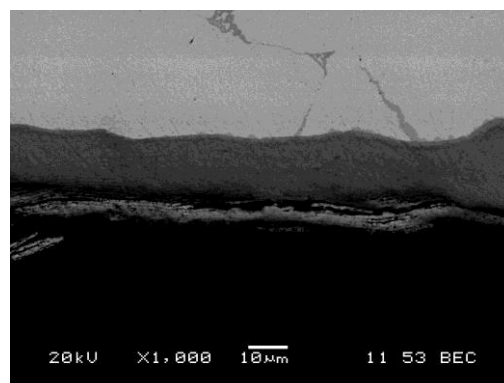
(d)

Figure 4.31 Morphologies (a, b) and cross-sectional views (c, d) of scale formed over NC (p)-10
and B-NC (p)-10 alloy samples respectively after oxidation at 1000°C for 30 min.

SEM micrographs taken from both samples after the 1000^oC/30 min. test showed that a granular type oxide structure formed over the as-cast sample (Figure 4.31 (a)) while long-rod type oxidation products cover the surface of the boronized sample (Figure 4.31 (b)). BE pictures of the sample cross-sections showed that scale formed over the boronized sample was thinner than that on the as-cast sample. Probably, because of the boride layer, less oxygen reacted with the Nb-rich alloy thus forming a thinner scale.

4.2.3.2 Oxidation of Niobium-Molybdenum Binary Alloys

Low temperature oxidation tests were conducted on the bulk-based NM (b)-1 alloy sample (46% Mo) in the as-cast condition. Up to 700^oC, the sample surface had a black color. After the 700^oC/30 min. test, the surface colors were black and green. After the 800^oC/30 min. test, the sample was completely covered with a dark gray oxide layer which also increased in volume. As a result, the scale cracked and separated from the alloy substrate. Also, the sample was observed to have adhered to the ceramic holder. In Figure 4.32 (a) and (b), the oxide scale formed after the 800^oC/30 min. test is shown. The scale contained mainly short-rod type crystals containing both Mo and Nb. At some locations, long and flat oxidation products rich in Mo (Figure 4.32 (a)) were observed. Such products were observed earlier over pure Mo samples (Figure 4.2 (b)). It was clear that Nb addition to Mo modified the morphology of the oxidation products of pure Mo. However, Nb addition did not prevent mass losses.

In another group of oxidation test, samples of the as-cast but powder-based NM (p)-3 (Mo-rich), NM (p)-4 (50% Mo) and NM (p)-5 (Nb-rich) alloys were used. After 800^oC, green oxide layers covered surfaces of (p)-3 and (p)-4 samples. However, surface of the (p)-5 sample appeared dark gray. After the 900^oC/30 min. test, surfaces of (p)-3 and (p)-4 were completely covered with green and voluminous oxide scales. At some places, these scales cracked and spalled from their substrates. The scale grown over the (p)-4 sample at 1000^oC had a few long and flat oxide crystals similar to the bulk-based alloy of the same composition. But the scale contained mostly short-rod type oxidation products (Figure 4.33 (a)). However, in

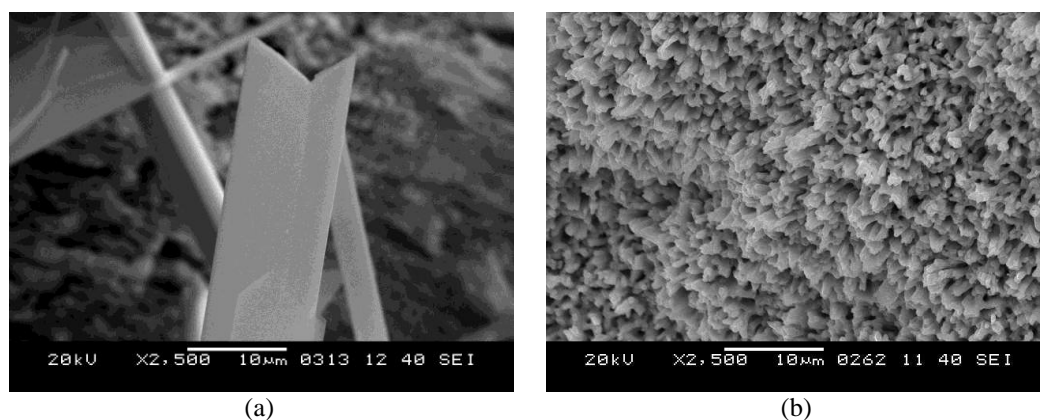the case of the Nb-rich (p)-5 alloy, long-rod type oxide crystals are observed in its scale (Figure 4.33 (b)).

(a)   (b)

Figure 4.32 SEM micrographs of the scale formed over NM (b)-1 alloy after oxidation at 800°C for 30 min.

In the case of the boronized samples, oxide products with different morphologies were observed. Dimensions of the oxide products over the boronized samples were smaller than those of the as-cast samples (Figure 4.33 (e), (f)). The dense and short-rod type oxide structure formed on the B-NM (p)-4 alloy had a good adhesion to its substrate. Also, Mo-rich thin and flat corrosion products were not present over this boronized alloy. Cross-sectional micrographs taken from the as-cast and the boronized alloys showed that thicknesses of the oxide layers grown over the boronized samples were smaller (Figure 4.33 (c), (g)).

These results suggested that more than about 30% Mo had a negative effect on the mechanical and chemical integrity of the oxide scales formed at high temperatures on the Nb-Mo binary alloys. This is possibly related to some of the Mo-oxide phases such as MoO_3 which is volatile at temperatures as low as 750°C. Thus, to prevent the degrading effect of Mo, its content in the alloy should be kept low. Boronizing of the Nb-Mo alloys was observed to have a positive effect on both the structure and the thickness of the scale grown over the alloys. As shown in Figure 4.33 (f) and (h), boronizing of the 50% Mo alloy caused a reduction in the thickness of the scale as well as the amount of Mo-rich flat-type oxidation products. Cracks observed at the scale/substrate interfaces (Figure 4.33 c, d, g, h) must be caused by the differences between the thermal expansion coefficients of the alloys and their corrosion products.
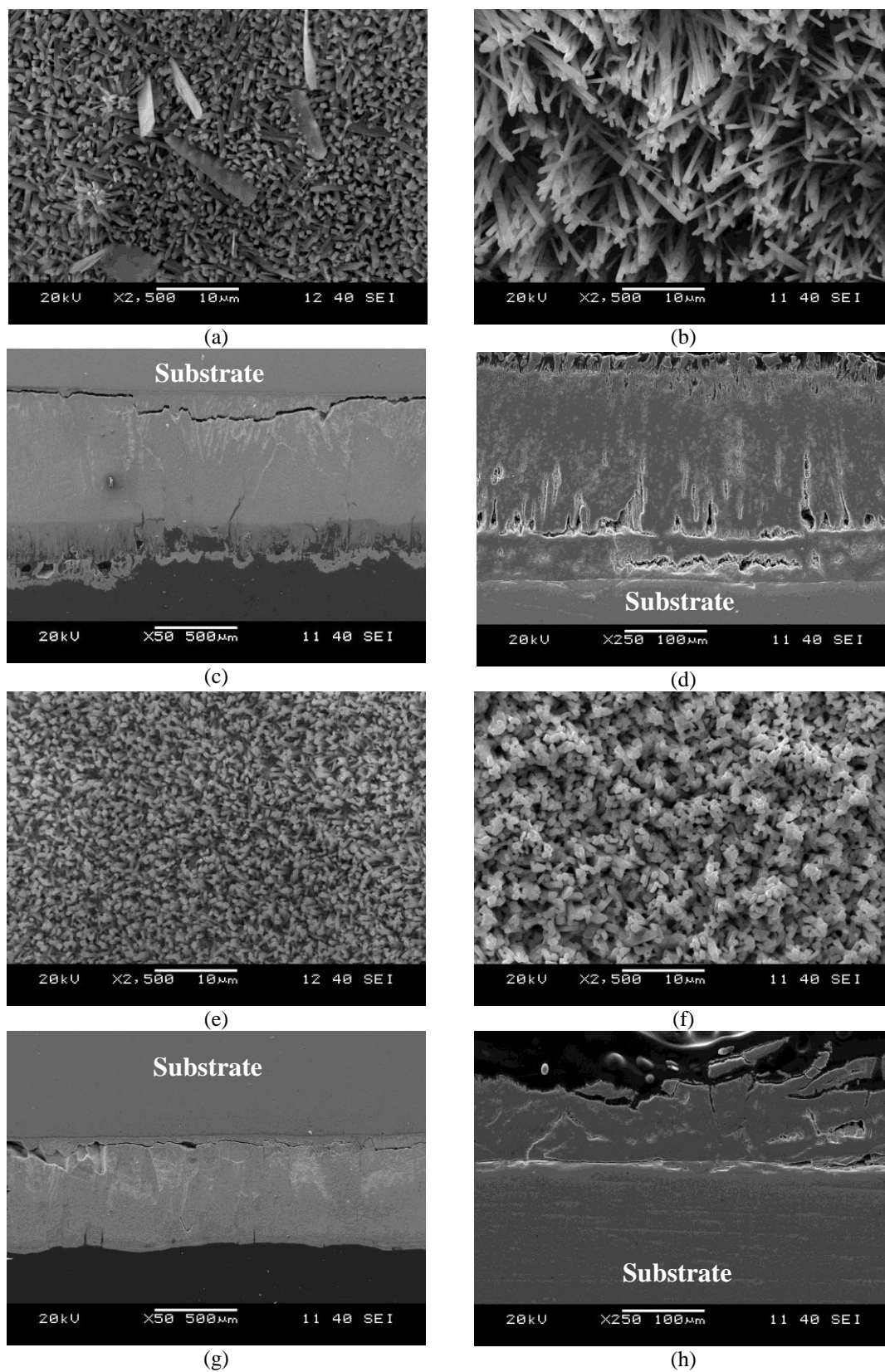
Figure 4.33 Morphologies and cross-sectional SEM micrographs of scales formed over (a, e) NM (p)-4, (b, f) B-NM (p)-4, (c, g) NM (p)-5 and (d, h) B-NM (p)-5 alloy samples after 1000°C /30 min.

Alternatively, volatile Mo oxide products that might have formed at this interface during oxidation would have caused formation and propagation of cracks at this interface.

XRD patterns of the oxidized Nb in "as-received" condition, NM (p)-4 and NM (p)-5 alloy samples in "as-cast" and" boronized" conditions after 1000°C are shown in Figure 4.34. The microstructure of the NM (p)-4, B-NM (p)-4 and B-NM (p)-5 samples were similar (Figure 4.33 (a), (e) and (f)). Although NM (p)-5 showed different microstructure, XRD patterns of all the "as-cast" and "boronized" Nb-Mo alloys were similar to each other.
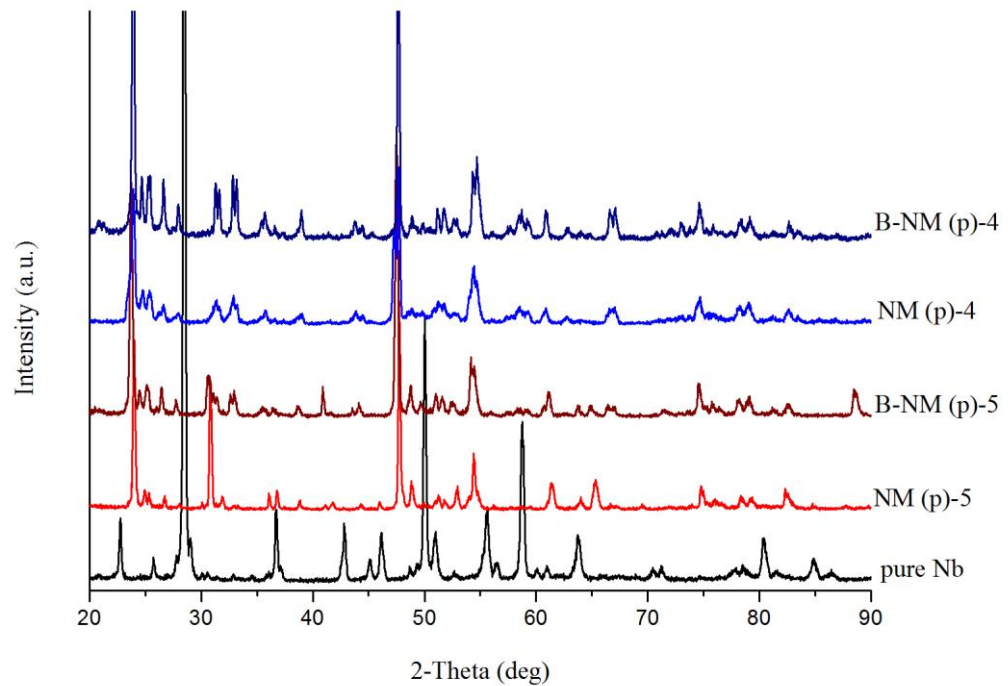
Figure 4.34 XRD analysis of "as-cast" and "boronized" Nb-Mo samples and as-received Nb plate after oxidation at 1000°C for 30 min.

4.3 Results and Discussion for Nb-based Ternary Alloys

4.3.1 Production and Characterization of Niobium-Chromium-Titanium Ternary Alloys

In the previous chapters, binary alloys were investigated. Here, the effect of the third alloying elements added to Nb-based alloy is discussed. Aluminum (Al), and/or Chromium (Cr) are generally used as alloying elements in high temperature oxidation resistant alloys since, under the proper conditions, they promote the formation of an oxidation resistant, protective oxide scales over the alloy surfaces.

As discussed earlier, when Cr is added to Nb, $NbCr_2$ type Laves phase-containing alloys with high melting points (about 1730^oC), relatively low densities (7.7 g/cm^3) and good oxidation resistances can be produced. However, as the amount of Cr addition increases, the amount of $CrNb_2$ phase increases causing brittleness at low temperatures (Thoma et al., 2002; Yoshida, & Takasugi, 1999).

Here, Titanium (Ti) is chosen as the third alloying element for the Nb-Cr binary system to improve mainly its oxidation resistance because Ti can prevent the formation of some of the sub-oxides of Nb which can be detrimental to alloys' oxidation resistance. According to the Ellingham diagram of oxides, TiO_2 (Ti oxide) is more stable than NbO at both high and low temperatures.

In this part of the study, Nb-Cr-Ti ternary alloys were produced by VAM (Table 4.8). Melting temperatures of Ti (T_m=1660^oC) and Cr (T_m= 1857^oC) are closer to each other but the melting temperature of Nb (T_m= 2468^oC) is much higher than those of Ti and Cr. Thus, to prevent material loss by evaporation from the alloy, the "stepwise" production method was used initially for the NCT (b)-1 alloy. In this method, first Ti-Cr binary alloy ingots were cast then Nb slugs were added to the binary alloy ingot.

Table 4.8 Production parameters and some properties of Nb-Cr-Ti ternary alloys.

Alloy No	Theoretical composition (in w/o)	Max. Electrode Current (A)	Number of melting cycles	% Weight loss observed	Unmelted material in the alloy	Behavior during cutting/ drilling
NCT (b)-1*	Nb-12Cr-18Ti	120	5	4.5	Not Observed	Satisfactory
NCT (p)-2	Nb-12Cr-18Ti	120	10	2.9	Not Observed	Satisfactory
NCT (p)-3	Nb-12Cr-18Ti	140	15	-	Not Observed	Satisfactory

*This alloy produced using "stepwise" method.

BE micrographs taken from the NCT (b)-1 alloy sample are given in Figure 4.35. EDS analyses showed that 5.3% Cr, 12.7% Ti and 82.0% Nb are present in the bright area; "A" whereas 13.1% Cr, 22.6% Ti and 64.3% Nb are present in the dark area; "B" in Figure 4.35 (b). It is clear that the area "A" is in the Nbss solid solution phase (β) whereas area B indicate segregation zones richer in Cr and Ti. Figure 4.35 (c) shows the changes that took place in the microstructure of the NCT (b)-1 alloy upon annealing. Long dendritic structures in the as-cast alloy disappeared after annealing at $1000^{o}C$ for 29 hours. However, some segregation was still present at the grain boundaries.

In Figure 4.36, the $1000^{o}C$ section of the Nb-Cr-Ti phase diagram is shown. The intended composition of the NCT (b)-1 alloy is labeled as "X". Note that the phase diagram is based on atomic % of the components whereas EDS data are reported as weight %. The alloy composition is not inside but very close to the single phase Nbss region. Although, formation of only the β phase was expected for this ternary alloy after the heat treatment, formation of some intermetallics along the grain boundaries was possible.

In Figure 4.37 (a) and (b), microstructures of the powder-based NCT (p)-2 alloy are given. As seen in these BE images, dendrites as the β-phase developed in the as-cast alloy. According to the EDS analyses result in Table 4.9, some Ti-rich participates were also present in the alloy.

(a)

(b)

(c)
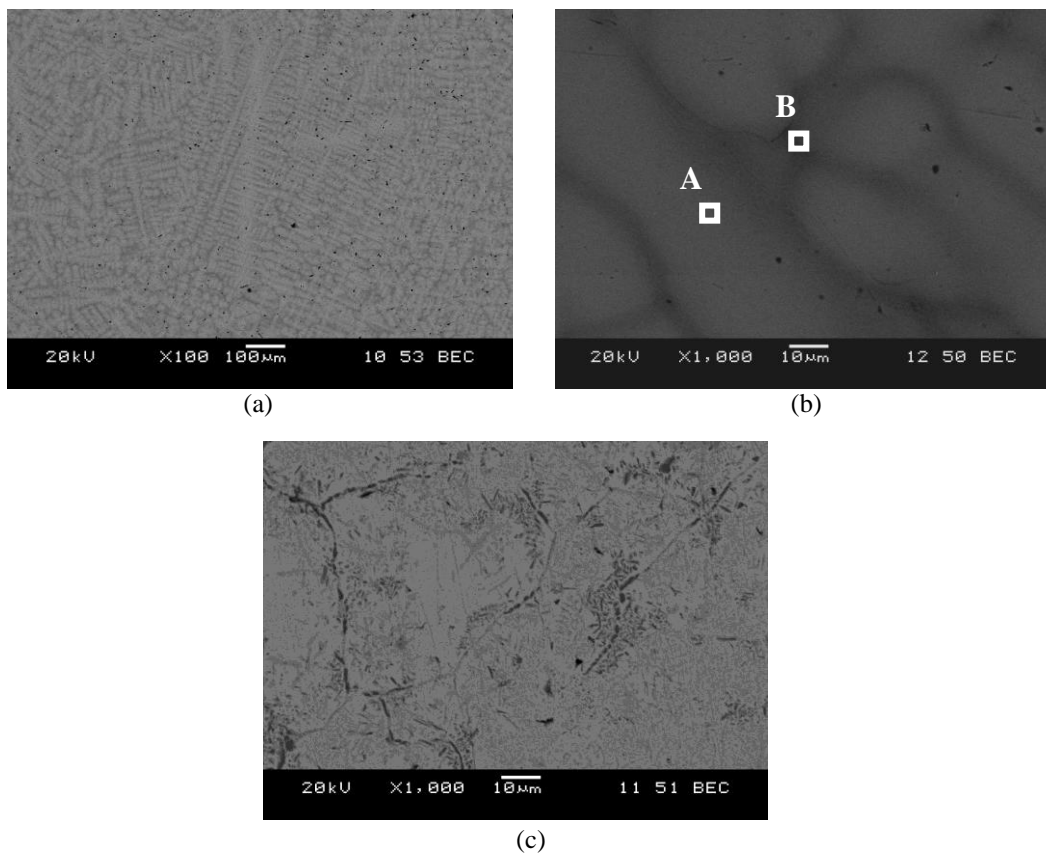
Figure 4.35 (a) Low magnification and (b) high magnification BE images of NCT (b)-1 (c) HT-NCT (b)-1 alloy.
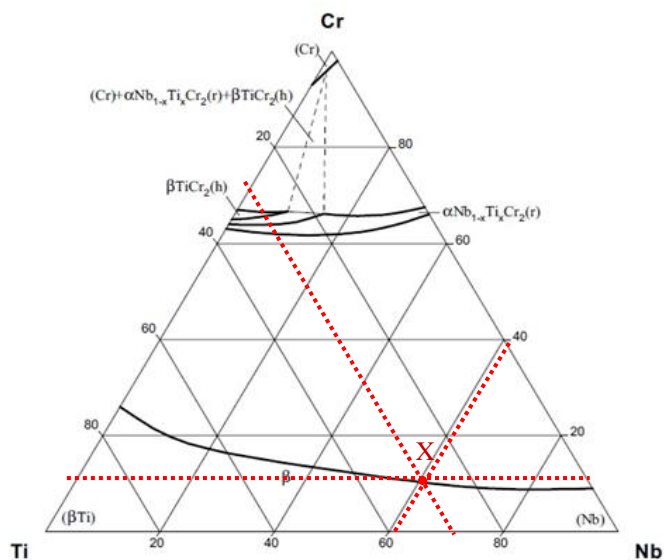
Figure 4.36 Section of Nb-Cr-Ti system at 1000°C and the theoretical composition of the ternary alloy based on atomic % of elements (Ghosh, n.d.).

BE micrographs of NCT (p)-2 alloy after 1000°C annealing for 44 hours is given in Figure 4.37 (c). Compared to the sample prepared by the bulk method, segregation along grain boundaries was much lower in this powder-based sample.

(a)　(b)

(c)
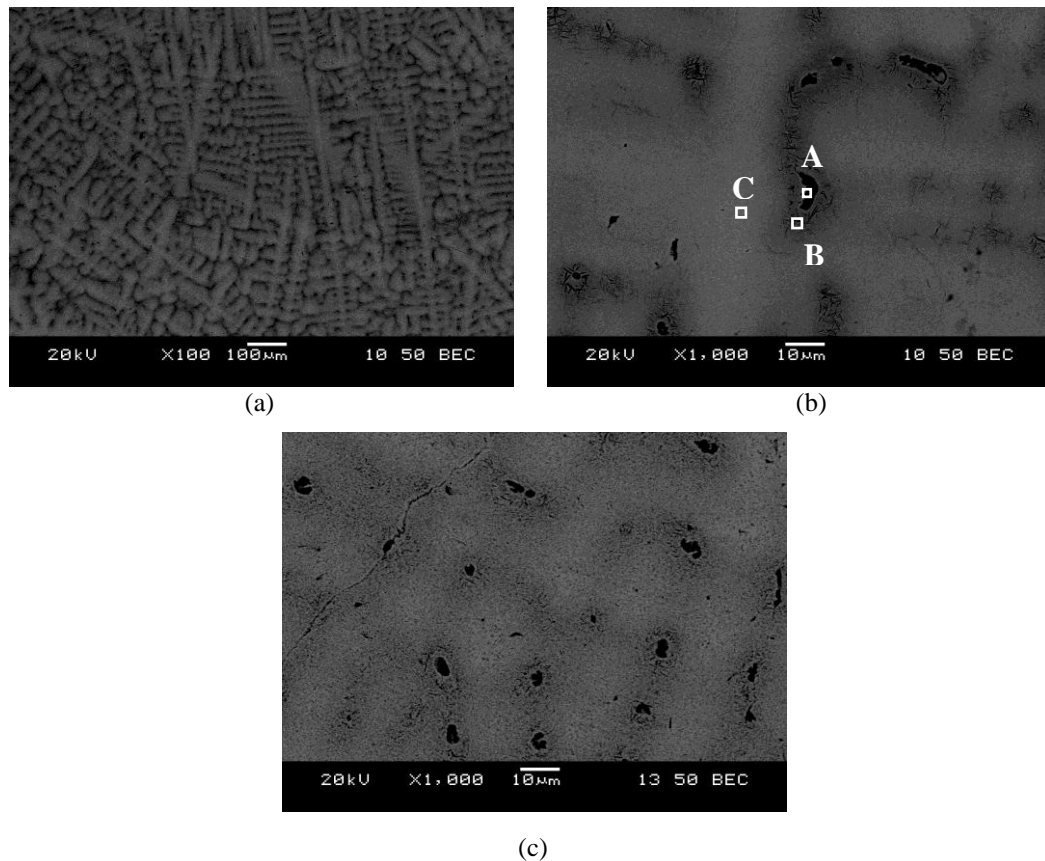
Figure 4.37 (a) Low magnification and (b) high magnification BE images of NCT (p)-2 (c) HT-NCT (p)-2 alloy.

Table 4.9 The compositions (in w/o) of individual phases in ternary Nb alloy.

Region	A	B	C
Nb	29.2	73.4	82.5
Cr	3.4	9.3	5.6
Ti	67.4	17.3	11.9

XRD analyses of the as-cast and heat treated NCT ternary alloys are given in Figure 4.38. While only the Nbss phase was detected in the NCT alloys, Cr_2Nb phase was also present in the structure after heat treatment as seen in the SEM pictures. This result suggested that the intended alloy composition slightly moved toward the 2-phase region, Nbss and [β-(Nb, Ti) Cr_2], in Fig 4.36.
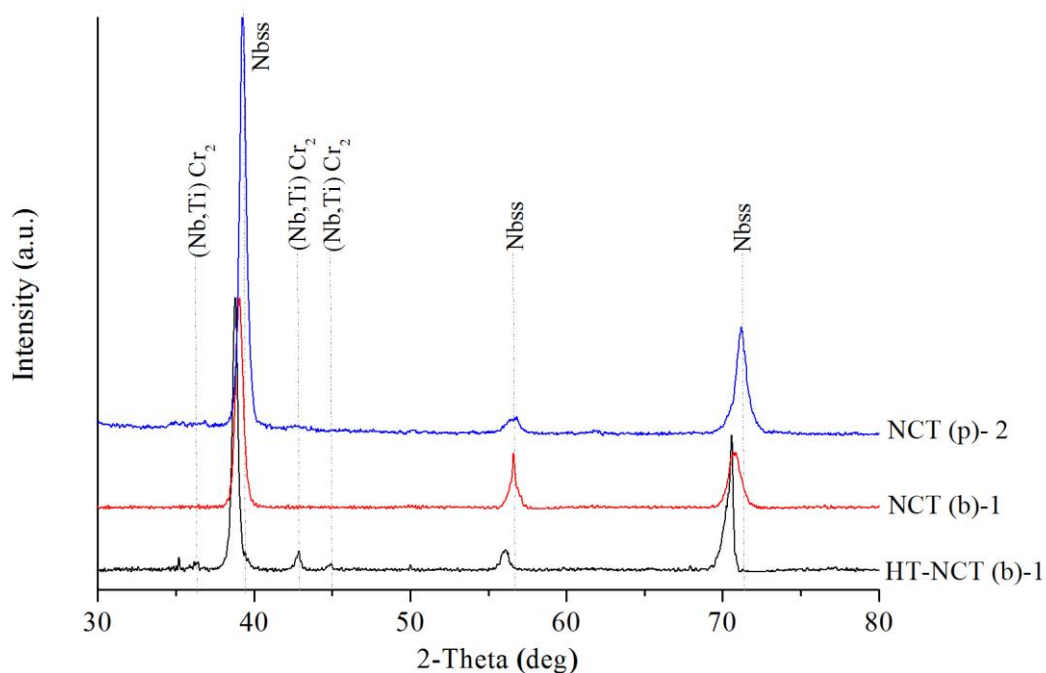
Figure. 4.38 XRD results of as-cast and heat treated ternary Nb alloys.

Production of ternary alloys was also conducted using the EB melting. However, as the data in Table 4.10 show, weight changes of the alloys produced by the EB method were very high. Because of significant material losses during alloy production electron beam melting studied were not continued.

Table 4.10 Electron beam current of the furnace, theoretical compositions and weight changes of the alloy ingots.

Sample No	Pure Metals	Theoretical Composition (in w/o)	~Max. Current (mA)*	Weight Before Melting (g)	Weight Change (%)
EBM 6	Nb	56.15	350–430	25.24	-25.7
	Ti	39.03			
	Cr	4.82			
EBM 7	Nb	47.52	350–210–350	29.89	-24.5
	Ti	35.42			
	Cr	17.06			

*1st, 2nd and 3rd numbers are the beam currents for the first and second melting cycles, respectively.

4.3.2 Boronizing of Niobium-Chromium-Titanium Ternary Alloy

A boronizing study was conducted on the niobium-titanium-chromium ternary alloy. Boronizing test conditions were the same as those mentioned in Chapter 3.2.2. A cross-sectional BE image of the ternary NCT (p)-3 alloy boronized at 950°C for 8h is given in Figure 4.40. A boron-rich layer with an average thickness of 2.50 μm was uniformly formed on the whole surface of this alloy.
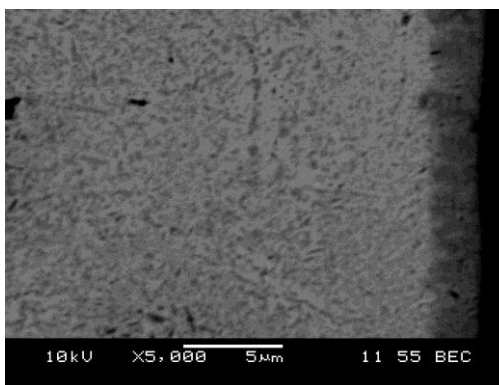
Figure 4.40 SEM/BE cross-sectional micrograph of the NCT (p)-3 sample boronized at 950°C for 8h.
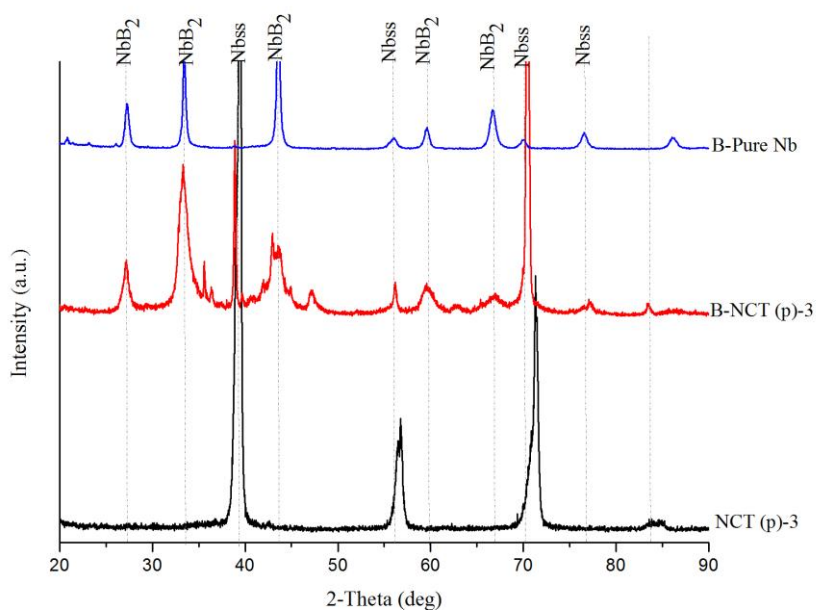
Figure 4.41 XRD diffraction pattern of B-Nb, NCT (p)-3, B-NCT (p)-3 samples.

In Figure 4.41, XRD analyses results of the NCT (p)-3 alloy before and after boronizing are shown. According to these results, NbB_2 layer formed over the alloy sample. Formation of the NbB_2 phase is consistent with the earlier boronizing tests conducted on pure Nb and Nb-based binary alloys.

4.3.3 Oxidation of As-cast and Boronized Niobium-Chromium-Titanium Ternary Alloys

"As-cast" and "boronized" NCT (p)-3 alloy sample was exposed to oxidation tests conducted in air at 800^oC, 900^oC and 1000^oC for 30 min. Long-rod type B-containing oxides covered the B-NCT (p)-3 sample surface (Figure 4.42 (b)) different from the surface of the oxidized as-cast NCT (p)-3 alloy (Figure 4.42 (a)). Similar to the boronized and oxidized Nb-Cr binary alloys, the boronized ternary alloy had a thinner oxide as shown in the cross-sectional SEM pictures (Figure 4.42 (c), (d)).

(a)   (b)

(c)   (d)
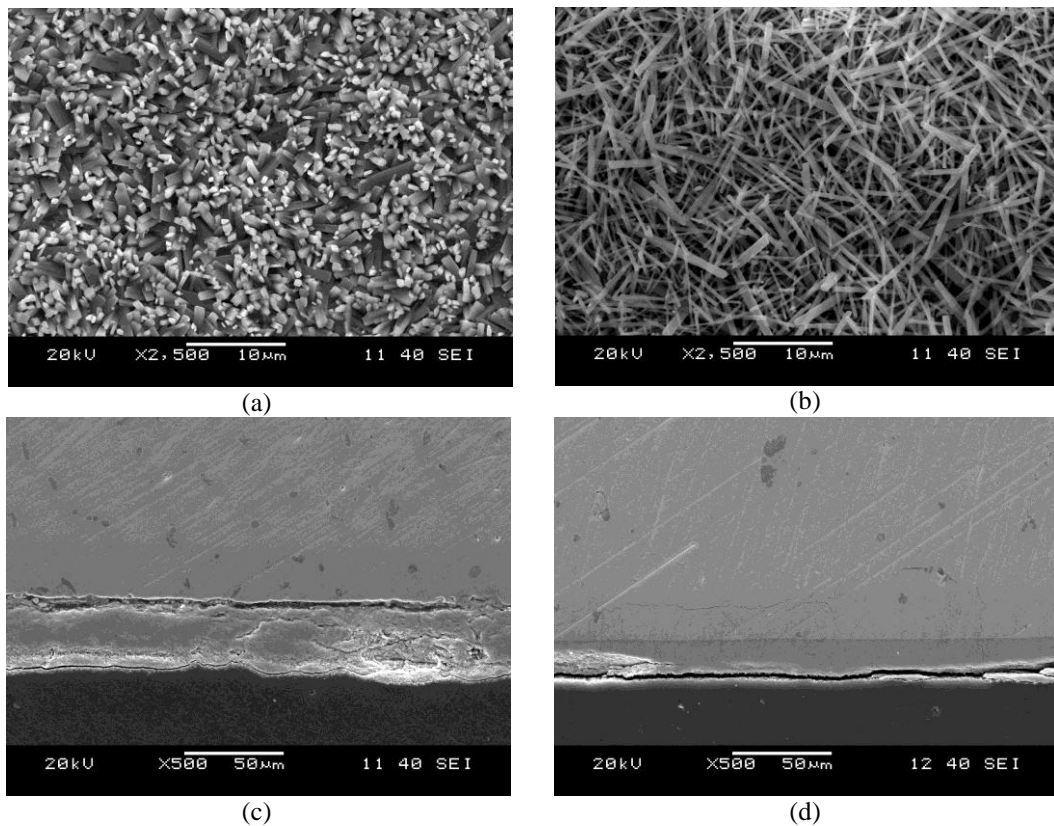
Figure 4.42 Morphologies and cross-sectional SEM micrographs of scales formed over (a, c) NCT (p)-3 and (b, d) B-NCT (p)-3 alloy samples after 1000^oC /30 min.

CHAPTER FIVE
CONCLUSIONS

In this Thesis, production and characterization of high temperature corrosion resistant materials was investigated. The base component of the produced materials (alloys) was the refractory metal Niobium (Nb) which has a melting temperature higher than 2000°C. However, oxidation resistance of most of the refractory metals in air is very low even at temperatures lower than 1000°C. Thus, to impart oxidation resistance, Nb was alloyed with elements such as Cr, Mo and Ti to make binary Nb-Cr, Nb-Mo and ternary Nb-Cr-Ti alloys. All the alloys studied in this investigation were produced by Vacuum Arc Melting (VAM). Both bulk (slug) and powder starting materials (metals) were used in the production of the alloys. High temperature oxidation tests on the alloys were conducted between 500 and 1000°C in air at atmospheric pressure. Characterization of the alloy microstructures and the oxidation products were made by using scanning electron microscopy (SEM) and X-ray diffraction (XRD). Because oxidation resistances of the produced alloys were found to be of moderate value, the process of boronizing (or boriding) was investigated as a surface modification method to improve oxidation resistance of Nb and Mo metals as well as some of the produced alloys. Overall conclusions of this study, based on the experiments results obtained, are as follows:

1. The Vacuum Arc Melting technique was suitable for the laboratory-scale production of refractory metal-base alloys. However, during the production of alloys containing metals with significantly different melting temperatures, loss of the metal with the lower melting temperature was observed. This was due to the high arc currents used to melt the metal with the higher melting temperature. In the case of the Electron Beam Melting (EBM) technique, the material loss was much higher because of the very high temperatures reached by the electron beam. Thus alloy production was mostly made by VAM.

2. During the earlier work on alloy production by using bulk (slugs) starting materials, unmelted metallic areas were found inside the ingots, mostly because of the differences between the melting temperatures of the alloy components. Thus, metal powders were used later in alloy production. Ingots made from metal powders were more homogeneous. In "as-cast" conditions, these ingots had microstructures that were very similar to those observed for the heat-treated ingots.

3. The Nb-Cr binary alloys produced had multi-phase microstructures containing the Nb-rich solid solution phase and the $NbCr_2$ phase also known as the Laves phase. Alloys containing large amounts of the Laves phase were brittle thus machining of oxidation test samples were difficult. On the other hand, Nb-Mo binary alloys and Nb-Cr-Ti ternary alloys had single-phase microstructures. These alloys were observed to be ductile.

4. Air oxidation behavior of pure Mo and Nb metals were different mainly because of the properties of their respective oxides; MoO_3 and Nb_2O_5. Because of its low melting point ($795^{o}C$), MoO_3 oxide vaporized as soon as it formed, thus did not form as a cover over the metal. Nb_2O_5 oxide was solid but also not protective for the Nb metal because the oxide was voluminous and poorly adhered to the metal causing spallation. These observations were consistent with the other studies reported in the literature.

5. Addition of Cr increased the oxidation resistance of Nb. Formation of Cr-rich oxide products were observed over the oxidized Nb-Cr alloys. However, because of the multiphase structure of these alloys, oxide layer was found to be discontinuous at locations underneath which Nb-rich solid solution phase was present. It was clear that the microstructure of the alloy was reflected in the nature of the oxide layer. Addition of Mo to Nb, on the other hand, decreased the volatilization of Mo. However, the alloy did not develop an oxide layer protective enough for long term service. Compared to Cr-rich Nb-Cr alloys, continuous oxide layer formed over the Nb-Cr-Ti ternary alloy.

6. Boronizing, caused the formation of MoB and NbB_2 layers over the surfaces of pure Mo and Nb metals, respectively. As expected, thicknesses of the boride layers increased with the processing time since the layer thickness was controlled by the diffusion of B atoms. When the pure Nb was oxidized at 1000^oC after boronizing, the oxide layer formed on the metal was found to be adherent and intact unlike the oxide on the "as-received" metal. In the case of Nb-Cr and Nb-Mo alloys, it was observed that the oxide scales formed over the boronized samples were thinner than the oxide scales formed over the samples which were not boronized. The boride layer is thought to have slowed down the access of oxygen to the alloy samples by forming protective oxidation products which possibly contained glassy phases.

REFERENCES

Alam, M., Rao, A. S., & Das, D. (2010). Microstructure and high temperature oxidation performance of silicide coating on Nb-based alloy C-103. *Oxidation of Metals, 73*, 513-530.

Argent, B. B., & Phelps, B. (1960). The oxidation of niobium-titanium and niobium-molybdenum alloys. *Journal of Less Common Metals, 2* (2-4), 181-190.

Baker, S. D. (1992). Binary alloy phase diagrams, In S. D. Baker (and others) (Eds.). *ASM Handbook: Alloy phase diagrams, 3* (48, 161, 292, 293, 306). Materials Park, OH: ASM International.

Barrett, C.A., & Clauss, F. J. (1958). In Gonser, B. M. & Sherwood, E. M. (Eds.) *Technology of Columbium (Niobium).* (98) Wiley, New York.

Begley, R. T., & Bechtold, J. H. (1961). Effect of alloying on the mechanical properties of niobium. *Journal of Less Common Metals, 3*, 1-12.

Behrani, V., Thom, A. J., Kramer, M. J., & Akinc, M. (2006). Microstructure and oxidation behavior of Nb-Mo-Si-B alloys. *Intermetallics, 14*, 24-32.

Benedict I. P., & Varma, S. K. (2010). Oxidation behavior of Nb-20Mo-15Si-5B-20Ti alloy in air from700 to 1300ºC. *Journal of Alloys and Compounds, 497*, 63-73.

Bewlay, B.P., Lewandowksi, J.J., & Jackson, M.R. (1997). Refractory metal intermetallic in-situ composites for aircraft engines. *JOM*, 44–67.

Bewlay, B. P., Jackson, M. R., & Subramanian P. R. (1999). Processing high-temperature refractory-metal silicide in-situ composites. *JOM*, 32–36.

Bewlay, B. P., Jackson, M. R., & Gigliotti, M. F. X. (2002). Niobium silicide high temperature in situ composites. In J. H. Westbrook, & R. L. Fleischer (Eds.). *Intermetallic compounds, Principles and Practice, 3* (541-560), John Wiley & Sons Ltd.

Bewlay, B.P., Jackson, M.R., Zhao, J. C., & Subramanian, P. R. (2003). A review of very-high-temperature Nb-silicide–based composites. *Metallurgical and Materials Transactions A*, *34 A*, 2043.

Brady, M. P. , Zhu, J. H., Liu, C. T., Tortorelli, P. F., Walker, L. R. (2000). Oxidation resistance and mechanical properties of Laves phase reinforced Cr in-situ composites. *Intermetallics, 8*, 1111-1118.

Buckman, R.W. Jr. (1988). Alloying of refractory metals. In J .R.Walter, M.R. Jackson, & C. T. Sims (Eds.). *Alloying.* (419–421). Metals Park, OH: ASM International.

Campos, I., Palomar, M., Amador, A., Ganem, R., Martinez, J. (2006). Evaluation of the corrosion resistance of iron boride coatings obtained by paste boriding process. *Surface & Coatings Technology,* 201, 2438–2442.

Chan, K. S. (2005). Alloying effect on the fracture thoughness of Nb-based silicides and Laves phases. *Materials Science and Engineering A, 409*, 257-269.

Chattopadhyay, K., Balachandran, G., Mitra, R., & Ray, K. K. (2006). Effect of Mo on microstructure and mechanical behavior of as-cast Nbss-Nb_5Si_3 in situ composites. *Intermetallics, 14*, 1452-1460.

Chattopadhyay, K., Mitra, R., & Ray, K. K. (2008). Nonisothermal and isothermal oxidation behavior of Nb-Si-Mo alloys. *Metallurgical and Materials Transactions A, 39A*, 577-592.

Choi, G., Lim, J., Muniratham, N. R., Kim, H. (2009). Purification of niobium by multiple electron beam melting for superconducting RF cavities. *Metals and Materials International, 15*, 3, 385-390.

Chou, T. C., & Nieh, T. G. (1993). Pesting of the high-temperature intermetallic MoSi$_2$. *JOM*, 15-21.

Chu, F., Thoma, D. J., Kotula, Gerstl, S., Mitchell, T. E., Anderson, I. M, & Bentley, J. (1998). Phase stability and defect structure of the C15 Laves Phase Nb (Cr, V)$_2$. *Acta Material, 46*, 5, 1759-1769.

Cox, A. R., & Brown, R. (1964). Protection of molybdenum from oxidation by molybdenum disilicide based coatings. *Journal of Less Common Metals, 6*, 36-50.

Davis, J. R. (Ed.). (1997). *ASM Speciality Handbook, Heat Resistant Materials* (361- 365). Metals Park, OH: ASM International.

Dimiduk, D. M., & Perepezko, J. H. (2003). Mo-Si-B alloys developing a revolutionary turbine-engine materials. *MRS Bulletin, 28*, 639.

DiStefano, J. R., Pint, B. A., & DeVan, J. H. (2000). Oxidation of refractory metals in air and low pressure oxygen gas. *International Journal of Refractory Metals & Hard Materials, 18,* 237-243.

Gaskell, D. R. (2003). Reactions involving pure condensed phases and a gaseous phase. In R. H. Bedford (Ed.) *Introduction to the thermodynamics of materials.* (4th ed.) (429), Taylor and Francis Books, Inc.

G. Ghosh. (n.d.). Cr-Nb-Ti (Chromium - Niobium - Titanium). In G. Effenberg, S. Ilyenko, (Eds.). *Light Metal Ternary Systems: Phase Diagrams.* Crystallographic and Thermodynamic Data. Landolt-Börnstein New Series IV/11A4.

Geng, J., Tsakiropoulos, P., & Shao, G. (2006). Oxidation of Nb–Si–Cr–Al in situ composites with Mo, Ti and Hf additions. *Materials Science and Engineering, A 441*, 26–38.

Geng, J., Tsakiropoulos P., & Shao G. (2007). A study of the effects of Hf and Sn additions on the microstructure of Nbss /Nb$_5$Si$_3$ based in situ composites, *Intermetallics, 15*, 69-76.

Goldschmidt, H. J., & Brand, J. A. (1960). The constitution of the chromium-niobium-molybdenum system. *Journal of Less Common Metal, 3*, 44-61.

Gritsch, M., Piplits, K. H., Hutter, P., Wilhartitz, H., Wildner., H.P., & Martinz (2000). Investigations on the oxidation behavior of technical molybdenum foils by means of secondary-ion mass spectrometry. *Surface Science, 454–456*, 284–288.

Grobstein, T., Doychak, J. (1988). *Oxidation of high-temperature intermetallic.* United States of America: TMS.

Habazaki, H., Hon-Yashiki, K., Ito, K., Mitsui, H., Kawasashima, A., Asami, K., Hashimoto, K., & Mrowec, S. (1999). Sulfidation and oxidation-resistant alloys prepared by sputter deposition. *Materials Science and Engineering, A267*, 267-276.

Hausner, H. H. (Ed.). (1966). *Coatings of High-Temperature Materials.* United States of America: Plenum Press.

Hebsur, M.G., Stephens J.R., Smialek, J.L., Barrett, C.A., & Fox, D.S. (1989). Influence of alloying elements on the oxidation behavior of NbAl$_3$. Grobstein T.& Doychak (Ed.) (171-183). *Oxidation of High-Temperature Intermetallics*, TMS.

Heilmaier, M., Krüger, M., Saage, H., Rösler, J., Mukherji, D., Glatzel, U, & et al. (2009). Metallic materials for structural applications beyond nickel-based superalloys. *JOM, 61*, 7, 61-67.

Helmick, D. A. (2003). *High temperature oxidation behavior of Mo-Si-B base alloys (6-20).* University of Pittsburg, PhD thesis.

Jackson, M. R. (1991). Chromium containing high temperature Nb-Ti-Al alloys.

Johnson, W. A. (1990). Molybdenum, Properties and selection: nonferrous alloys and special purpose-material. In Davis, J.R. (Ed.) *ASM Handbook, Properties and Selection: Nonferrous Alloys and Special Purpose-Materials,* Volume 2 (574-577), Materials Park, OH: ASM International.

Jun, W., Xiping, G., & Jinming, G. (2009). Effects of B on the microstructure and oxidation resistance of Nb-Ti-Si-based ultrahigh-temperature alloy. *Chinese Journal of Aeronautics, 22*, 544-550.

Keitz, A. V., & Sauthoff, G. (2002). Laves phases for high temperatures- Part II: stability and mechanical properties. *Intermetallics, 10*, 497-510.

Khanna, A. S. (2002). *Introduction to high temperature oxidation and corrosion.* United States of America: ASM International.

Kim, W., Tanaka, H., Kim, M., & Hanada, S. (2003). High temperature strength and room temperature fracture toughness of Nb-Mo-W refractory alloys with and without carbide dispersions. *Materials Science and Engineering, A346*, 65-74.

Kling, H. P. (1958). In Gonser, B. M. & Sherwood, E. M. (Eds.) *Technology of Columbium (Niobium).* (87) Wiley, New York.

Klopp, W. D. (1960). Oxidation Behavior and Protective Coating for Columbium and Columbium-Base Alloys, Defense Metals Information Center Report 123.

Kubaschewski, O., & Hopkins, B. E. (1960). Oxidation mechanism of niobium, tantalum, molybdenum and tungsten. *Journal of Less Common Metals, 2*, 2-4, 172-180.

Kubaschewski, O., & Hopkins, B. E. (1962). Niobium and tantalum. In *Oxidation of metals and alloys* (2nd Ed.) (219-220). London: Academic Press Inc., Publishers.

Kubaschewski, O., & Alcock, C.B. (1979). Thermodnamic Data, The Tabulation of Data. In *Metallurgical Thermo-Chemistry* (5th Ed.) (268-413). Pergamon Press.

Kumar, K. S., & Liu, C. T. (1993). Ordered intermetallic alloys, part II: silicides, trialuminides, others. *JOM*, 28-33.

Kuznetsov, S.A, Kuznetsova, S.V., Rebov, E.V, Mies, Croon, M.H.J.M, & Schouten, J.C. (2004). Synthesis of molybdenum borides and molybdenum silicides in molten salts and their oxidation behavior in an air-water mixture. *Surface and Coating Technology*.

Lai, G. Y. (1990). *High-temperature corrosion of engineering alloys.* United States of America: ASM International.

Lambert, J. B., & Rausch, J. J. (1990). Refractory metals and alloys. In J. R. Davis (Ed.). *ASM Handbook, Properties and selection: Nonferrous alloys and special purpose-materials*, 2 (557-565). Materials Park, OH: ASM International.

Lei, M.K., Zhu, X.P., Han, S.Q., Wang, D.Y., Wang, F.G., & Wang, F. (2000). Effect of borate coating on oxidation resistance of γ-TiAl intermetallic compound. *Materials Chemistry and Physics, 65*, 249-252.

Levin, E.M. (1966). *Journal of research of the National Bureau of Standarts A, 70*, 1, 11-16.

Lipetzky, P. (2002). Refractory metals: a primer. *JOM, 54 (*3) , 47-49.

Mandal, P., Thom, A. J., Kramer, J. M., Behrani, V., & Akinc, M. (2004). Oxidation behavior of Mo–Si–B alloys in wet air. *Materials Science and Engineering, A 371*, 335–342.

Mayo, G. T. J., Shepherd, W. H., & Thomas, A.G. (1960). Oxidation behaviour of niobium-chromium alloys. *Journal of Less Common Metals, 2*, 223-232.

Meetham, G. W., & Van de Voorde, M. H. (2000). *Materials for high temperature engineering applications.* Springer.

Michalkiewicz, B., Nazzal, J.S., Tabero, P., Grzmil, B., & Narkiewicz, U. (2008). Selective methane oxidation to formaldehyde using polymorphic T-, M-, and H-forms of niobium (V) oxide as catalysts. *Chemical Papers, 62*, 1, 106-113.

Miller, G. L., & Cox, F.G. (1960). Development of oxidation resistance of some refractory metals. *Journal of Less Common Metals, 2*, 207-222.

Monicca, M. P. (2009). *High temperature oxidation characteristics of Nb-10W-xCr alloys* (49-51). The University of Texas et al Paso, PhD thesis.

Mu, D., & Shen, B. (2010). Oxidation resistance of boronized CoCrMo alloy. *Int. Journal of Refractory Metals & Hard Materials, 28*, 424-428.

Mu, D., Yang, C., Shen, B. & Jiang, H. (2009). Oxidation resistance of borided pure cobalt. *Int. Journal of Refractory Metals & Hard Materials, 479*, 629-633.

Northcott, L. (1961). Some features of the refractory metals. *Journal of Less Common Metals, 3,* 125-148.

Perepezko, J. H. (2009). The hotter the engine, the better. *Science, 326*, 1068-1069.

Perkins, R. A., Chiang, K. T., Meier, G. H., & Miller, R. (1989). Formation of alumina on niobium and titanium alloys. In T. Grobstein, & J. Doychak (Eds.). *Proceedings of the workshop on the oxidation of high-temperature intermetallics.* (159). United States of America: TMS.

Perkins, R. A., & Meier, G. H. (1990). The oxidation behavior and protection of niobium. *JOM*, 17-21.

Sahin, S., & Meric, C. (2002). Investigation of the effect of boronizing on cast irons. *Materials Research Bulletin, 37*, 971-979.

Sha, J., Liu, J., & Zhou, C. (2010). Effect of Cr additions on thoughness, strength, and oxidation resistance of an Nb-4Si-20Ti-6Hf alloy at room and/or high temperatures. *Metallurgical and Materials Transactions A*.

Sheasby, J. S., & Smeltzer W. W. (1981). Oxygen tracer studies of the oxidation of niobium. *Oxidation of Metals, 15* (3/4), 215-229.

Sheftel, E. N., & Bannykh, O. A. (1994). Niobium-base alloys. *Int. J. of Refractory~ Metals & Hard Materials 12*, 3, 303-314.

Smith, R. (1960). The development of oxidation-resistant niobium alloys. *Journal of Less Common Metals, 2* (2-4), 191-206.

Smolik, G. R., Petti, D. A., & Schuetz, S. T. (2000). Oxidation and volatilization of TZM alloy in air, *Journal of Nuclear Materials, 283-287*, 1458-1462.

Speiser, R. & Pierre, G. R. St. (1964). Fundamentals of Refractory Metal-Gaseous Environment Interactions. In Promisel, N. E. (Ed.) *The Science and Technology of Selected Refractory Metals* (289), Pergamon, Oxford.

Stringer, J. (1973). Are there new approaches to alloying which may produce oxidation- resistant refractory metal alloys? Liverpool University, England: Defense Technical Information Center.

J. F. Stringer, R. I. Jaffee, & T. F. Kearns (Eds.). (1975). *High temperature of aerospace alloys*, Advisory group for aerospace research and development, North Atlantic Treaty Organizations, AGARD-CP-120. London: Technical editing and reproduction Ltd.

Stott, F.H. (1989). Influence of alloy additions on oxidation. *Materials Science and Technology, 5*, 734–740.

Subramanian, P.R., Mendiratta, M.G., & Dimiduk, D.M. (1996). The development of Nb-based advanced intermetallic alloys for structural applications. *JOM, 48,* 1, 33-38.

Takasugi, T., Hanada, S., & Yoshida, M. (1995). High temperature mechanical properties of C15 Laves phase Cr_2Nb intermetallics. *Materials Science and Engineering A 192/193*, 805-810.

Takeyama, M., & Liu, C. T. (1991). Microstructure and mechanical properties of Laves-phase alloys based on Cr_2Nb. *Materials Science and Engineering, A 132*, 61-66.

Thoma D. J. , Nibur, K. A., Chen , K. C., Cooley, J. C., Dauelsberg, L. B., Hults, W. L., Kotula, P. G. (2002). The effect of alloying on the properties of $(Nb,Ti)Cr_2$ *C*15 Laves phases. *Materials Science and Engineering, A329–331*, 408–415.

Titran, R. H. (1992). Niobium and its alloys, *Advanced Materials & Processes, 11*, 34-41.

Tortorelli, P. F., & Pint, B. A. (1996). *Oxidation behavior of Cr-Cr₂Nb alloys.* In D. A. Shores, & P. Y. Hou (Eds.). Fundamental aspects of high temperature corrosion VI. 1-5.

Türkdoğan, E. T. (1980). *Physical Chemistry of High Temperature Technology*, Academic Press, 1-26.

Ulf, L., Larsson, M. & Harrysson, L. A. (2003). Rapid manufacturing with electron beam melting (EBM)-A manufacturing Revolution. Direct Metal Fabrication, SME, Dearborn, Michigan, USA.

Uslu, I., Comert, H., Ipek, M., Ozdemir, O., Bindal, C. (2007). Evaluation of borides formed on AISI P20 steel. *Materials and Design, 28*, 55–61.

Usta, M., Ozbek, I., Bindal, C., Ucisik, A. H., Ingole, S., Liang, H. (2006). A comparative study of borided pure niobium, tungsten and chromium. *Vacuum, 80*, 1321-1325.

Varma, S. K., Parga, C., Amato, K., & Hernandez. (2010). Microstructures and high temperature oxidation resistance of alloys from Nb–Cr–Si system. *J. Material Science, 45*, 3931-3937.

Vellios, N., & Tsakiropoulos, P. (2007). The role of Sn and Ti additions in the microstructure of Nb-18Si base alloys. *Intermetallics, 15*, 1518-1528.

Ventura, J. & Varma, S. K. (2009). The oxidation resistance of Nb-20Mo-15Si-5B-20Cr up to 1,300ºC. Journal of the minerals, metals and materials society *JOM, 61* (7), 72-75.

Vilasi, M., Francois, M., Brequel, H., Podor R., Venturini G., & Steinmetz J. (1998). Phase equilibria in the Nb–Fe–Cr–Si System, *Journal of Alloys and Compounds, 269*, 187–192.

Weber, R., Bouvier, J. & Slama, G. (1973). Failure mechanism of aluminide and silicide coating on a niobium alloy subjected to thermal cyclic in air. *Journal of Less Common Metals, 32*, 1-20.

Wilkinson, W. D. (1969). *Properties of refractory metals.* New York: Gordon & Breach Science Publishers.

Wlodek, S. T. (1960). The Properties of Cb-Ti-W Alloys. Part I Oxidation. In Douglass, D. L., & Kunz, F. W. (Eds.). *Columbium Metallurgy*, AIME Metallurgical Society Conferences, 10 (175). Interscience, New York.

Wright, I. G. (1987). High Temperature Corrosion. In L. J. Korb, (Ed). *ASM Handbook, Volume 13. Corrosion* (97–103). Metals Park, OH:ASM International.

Yao, D., Cai, R., Zhou, C., Sha, J., Jiang, H. (2009). Experimental study and modeling of high temperature oxidation of Nb-base in situ composites. *Corrosion Science, 51*, 364–370.

Yoshida, M., & Takasugi, T. (1999). Phase relation and microstructure of the Nb-Cr-W alloy system. *Materials Science and Engineering A262*, 107-114.

Zhang, F., Zhang, L. T., Shan, A. D., Wu, J. S. (2005). In situ observations of the pest oxidation process of $NbSi_2$ at 1023 K. *Scripta Materialia, 53*, 653-656.

Zheng, H. Z., Lu, S. Q., & Huang, Y. (2009). Influence of grain size on the oxidation behavior of $NbCr_2$ alloys at 950-1200°C. *Corrosion Science, 51*, 434-438.

Zmii, V. I. , Ruden'kii, S. G,Bredikhin, M. Y., & Kunchenko, V. V. (2008). High-temperature oxidatiın-resistant coatings on niobium and its alloys. *Powder Metallurgy and Metal Ceramic, 47*, 3-4, 255-259.